



Organic Light-Emitting Diodes based on New Promising Materials

Charlotte Fléchon

University College London
Department of Physics and Astronomy
2013

A dissertation submitted for the degree of Doctor of Philosophy

I, Charlotte Fléchon, confirm that the work presented in this thesis is my own. Where information has been derived from other sources, I confirm that this has been indicated in the thesis.

Abstract

The present work focuses on the investigation of two types of new materials, phosphorescent and near-infrared, for the fabrication of solution-processible Organic Light-Emitting Diodes (OLEDs).

After the introduction of the theoretical background in the first part, the second part concentrates on phosphorescent OLEDs based on copper transition metal complexes. The photophysical properties of the copper complexes, the phosphorescent host and the interlayers were studied before the fabrication of phosphorescent OLEDs. Despite the various colours exhibited by the metal complexes all devices emit white light. The possible formation of an exciplex at the guest/host interface was thus investigated. Finally the influence of the solvent on the morphologies of the films and the performances of the devices were studied.

The third part focuses on near-infrared OLEDs obtained by using two different strategies. First by using a near-infrared copolymer emitting at 880 nm and incorporating it in green and red hosts and second by the creation of what is believed to be an exciplex at the interface between a hole injection layer and twisted organic molecules that emit at 515 and 540 nm. In both cases pure infra-red light above 800 nm was achieved.

A tout ceux qui ont toujours cru en moi

Acknowledgements

To begin with, I would like to thank Prof. Franco Cacialli for welcoming me in his international group, for his enthusiasm and for letting me work my own way.

I would also like to thank Marten who started his PhD on the same day as me. I have enjoyed our long scientific discussions, thanks for all your explanations and your patience. You have been such a great “PhD companion”.

Then I would like to thank all the chemists who have provided me with materials. My work would not have been the same without their help so thanks to Dietrich Breusov and his supervisor Ulrich Scherf, thanks to Claudia Bizzarri and her supervisor Luisa De Cola and finally thanks to Koke and Sunil Choudhary. Thanks to you all for your hard work and your availability.

Special thanks to those who took time to proofread my thesis: Olly, my mum and Marten.

I would also like to thank the rest of the group Mattia, Olly, Gustaf, Francesco, Pengei, Yong, Nico, Ania, Francesco number II, Giulia, Sadi, Giuseppe. Thanks to all of you for your jokes, discussions and availability. The master students Aurelio, Giuseppe, Alessandro, Supriya, Tanzim, the ones I have forgotten and all the guests who have visited our group throughout these three years. Thanks to the staff of UCL and all the people we never see but make all this possible.

Thanks as well to the training network and to all who provide us with money: the European Commission Marie Curie Research Training Net-work THREADMILL (grant number: MRTN-CT-2006-036040), the EC Seventh Framework Programme (FP7/2007-2013) under grant number 212311 (ONE-P) and the physics department of UCL.

Thanks to Guillaume Wantz and the ELORGA research group in Bordeaux to make me discover the wonderful field of organic electronics.

And finally thanks to my parents who have always believed in me, my sister Cécile and all my family who have supported me throughout my thesis. Thanks to all my friends especially Omrane, Florent, Myriam, Maïlys, Aurélie L., Aurélie M., Maréva, Aurélien, Justine, Anne-Elise, Céline, Nicolas Y., Fuit, Stéphanie, Anne, Alexis and Catherine and to the Hiking and Walking Club for their support. And last but not least a huge thank to my Yummy who has taught me so much about life.

Table of Contents

Abstract	4
Acknowledgements	6
List of figures	12
List of tables	18
Part I. Introduction & Scientific Background	20
1 Introduction	21
2 From π-conjugated materials to devices	23
2.1 <i>π-conjugated materials</i>	23
2.2 <i>What is an Organic Light-Emitting Diode?</i>	25
2.3 <i>Experimental steps of the fabrication of an OLED</i>	27
2.3.1 ITO substrates and oxygen plasma treatment.....	27
2.3.2 PEDOT:PSS	28
2.3.3 Active layer and interlayer.....	29
2.3.4 Cathode	30
2.4 <i>Charge injection</i>	31
2.5 <i>Importance of the interfaces</i>	31
2.6 <i>Charge transport and trapping in amorphous organic materials</i>	32
2.7 <i>Energy transfer: the exciton diffusion</i>	34
2.8 <i>Interchain interactions</i>	36
2.8.1 Interactions in the excited states: exciplexes, excimer and polaron pairs	36
2.8.2 Interactions in both ground states and excited states: aggregation (dimer) ...	38
2.9 <i>Efficiencies and CIE coordinates</i>	39
3 Experimental techniques	44
3.1 <i>UV-Vis spectroscopy</i>	44
3.2 <i>Photoluminescence measurements</i>	46

3.3	<i>Time-correlated single photon counting (TCSPC)</i>	46
3.4	<i>IVL measurements</i>	47
3.5	<i>Thickness measurements</i>	48
3.6	<i>Atomic Force Microscopy (AFM)</i>	48
3.7	<i>HOMO, LUMO determination via cyclic voltammetry</i>	49
3.7.1	Background on voltammetric techniques.....	50
3.7.1.1	Cyclic Voltammetry.....	50
3.7.1.2	Ferrocene, an internal standard	52
3.7.2	Experimental procedure	53
3.7.3	HOMO-LUMO calculations	54
3.7.4	HOMO-LUMO measurements of some classic polymers and small molecules used in organic electronics devices.	55
PART II. Phosphorescent OLEDs		57
4	Triplet excitons, phosphorescence and Cu-complexes	58
4.1	<i>Theory behind the triplet exciton</i>	58
4.2	<i>Cu-complexes and their applications in OLEDs</i>	61
4.2.1	Theoretical background on transition metal complexes	61
4.2.1.1	Transition metal complexes.....	62
4.2.1.2	d^{10} transition metal complexes and the tetrahedral coordination.....	63
4.2.1.3	The particular case of Cu-complexes.....	64
4.2.2	Literature review on Copper complexes based OLED	65
4.3	<i>How to choose a good host?</i>	66
5	Study of the TFB/PVK/TPBi structure spin-coated from chlorobenzene	67
5.1	<i>Materials properties</i>	67
5.1.1	PVK.....	67
5.1.2	Incorporation of a hole-injecting layer: TFB	71
5.1.3	Incorporation of an electron-injecting layer: TPBi.....	73
5.2	<i>Single and multilayer device properties</i>	74
5.2.1	PVK.....	75
5.2.2	TFB/PVK	76
5.2.3	PVK/TPBi	80
5.2.4	TFB/PVK/TPBi.....	84

5.3	<i>Conclusion</i>	87
6	OLED devices doped with Cu-complexes and spin-coated from chlorobenzene	88
6.1	<i>The Copper compounds</i>	89
6.1.1	Absorption	91
6.1.2	Emission properties in solution at room temperature	92
6.1.3	Emission in solid state at low temperature	92
6.1.4	Emission in solid state at room temperature	93
6.2	<i>Experiments</i>	95
6.2.1	Fabrication of the devices	95
6.2.2	PVK/TPBi devices	95
6.2.3	Discussion on the energy levels	95
6.2.4	Effect of the triplet concentration	97
6.2.4.1	Results	97
	Compound A	102
	Compound B	102
	Compound C	102
	Compound D	102
	Compound E	103
	Compound G	103
	General observations	103
6.2.5	Insertion of a hole-injecting layer: TFB	104
6.2.5.1	Preliminary test	104
6.2.5.2	Effect of the guest concentration	107
6.3	<i>Photophysical results</i>	108
6.3.1	Compound A	109
6.3.1.1	Pure A	109
6.3.1.2	Blend of PVK and A	110
6.3.2	Summary on the photophysics of PVK, A and PVK:A	113
6.4	<i>Conclusion</i>	114
7	On the importance of the solvent for phosphorescent OLEDs based on Cu-complexes	116
7.1	<i>Preliminary experiments</i>	117
7.1.1	Influence of the solvent on the absorption spectra of PVK	117
7.1.2	Influence of the solvent on pure PVK devices	118

7.1.3	Influence of the solvent on PVK/TPBi devices	121
7.2	<i>Influence of the solvent on the phosphorescent OLEDs</i>	123
7.3	<i>Conclusion</i>	126
PART III Near Infrared OLED		127
8	OLEDs based on a benzoselenadiazole compound.....	130
8.1	<i>Experimental details</i>	131
8.1.1	Materials.....	131
8.1.2	Energy levels of the materials	132
8.1.3	Devices.....	132
8.2	<i>Results</i>	132
8.2.1	Pure material OLEDs	132
8.2.2	Blended active layer OLEDs	136
8.2.3	Effect of a TFB interlayer on F8BT devices.....	140
8.2.4	F8BT:P3HT blend	146
8.3	<i>Conclusion</i>	150
9	Near-infrared emission from compounds emitting in the visible	151
9.1	<i>The compounds</i>	151
9.2	<i>Absorption and photoluminescence</i>	154
9.3	<i>OLEDs</i>	155
9.3.1	Basic devices	155
9.3.2	Insertion of an hole-injecting layer.....	157
9.3.3	Investigation of the origin of the near-infrared emission	159
9.4	<i>Conclusion and outlook</i>	161
10	General Conclusion	163
10.1	<i>Outlook</i>	164
Bibliography		166
List of abbreviations, mathematical symbols and compounds		187

List of figures

Figure 2-1 a) Representation of the three sp^2 orbitals b) Representation of the overlap of the p orbitals forming a π and π^* orbital. The σ orbitals are shown in the upper figure, but have been removed from the bottom picture for clarity. Reprinted with permission from [5]. Copyright © 2007, John Wiley and Sons.....	23
Figure 2-2 On the left, chemical structure of benzene and on the right, the six p orbitals of benzene overlap to form three bonding orbitals (a), (b) and (c). The three orbitals superimposed are shown in (d). Reprinted with permission from [5]. Copyright © 2007, John Wiley and Sons.....	24
Figure 2-3 Energy level scheme of an OLED with applied bias.....	26
Figure 2-4 Schematic of the sandwich structure OLED.	27
Figure 2-5 Structure of PEDOT (left) and PSS (right).	28
Figure 2-6 Metal/organic interface energy diagram a) without and b) with an interface dipole Δ . Φ_{Be} and Φ_{Bh} are the electron and hole barriers, Φ_M the metal work function, E_{vac} the vacuum levels, EA the electronic affinity and IE the ionisation energy of the organic material.	32
Figure 2-7 Schematics of hopping via high ionization potential compound in the presence of a low ionization potential compound: (a) hopping via high-Ip material (no dopant); (b) hopping via high-Ip material in the presence of a small amount of a low-Ip compound (trapping at the sites of low Ip); (c) hopping via both low-Ip and high-Ip material; (d) hopping via low-Ip compound exclusively. Reprinted with permission from Pai et al. [39]. Copyright © 1984 American Chemical Society.....	34
Figure 2-8 Förster and Dexter energy transfer.....	35
Figure 2-9 Orbital interactions of a) DA ground state pairs and b) D ^{-*} -A exciplexes. Reproduced with permission from Turro et al. [46]. Copyright 2009, Mill Valley, California. All rights reserved.	37
Figure 2-10 Illustration of the two mechanisms for electron-hole capture. Electrons and holes are transported through their respective transport materials and accumulate at the heterojunction. a) Injection of one of the charges into the opposite polymer enables charge capture within the polymer bulk and formation of intramolecular excitons. b) Barrier-free electron-hole capture directly produces a neutral excited-state, the exciplex, without prior injection of a charge carrier into the opposite polymer. The exciplex can either be thermally activated and transferred to the bulk exciton, leading to exciton electroluminescence or, with small oscillator strength, it can also decay radiatively and emit red-shifted exciplex electroluminescence. Reprinted with permission from [48]. Copyright 2006 Wiley-VCH Verlag GmbH & Co. KGaA.....	38
Figure 2-11 CIE 1931 colour space chromaticity diagram. Reprinted from [64].	41
Figure 2-12 Elementary processes for charge recombination, production of excitons, internal and external light emission in an OLED.....	42
Figure 3-1 Possible electronic transitions in UV-Vis spectroscopy.....	45
Figure 3-2 Scheme of a UV-Vis spectrometer	45

Figure 3-3. a) typical excitation function for cyclic voltammetry. Reprinted with permission from [72]. Copyright 1999 Wiley-VCH Verlag GmbH & Co. KGaA. and b) cyclic voltammogram. Reprinted with permission from [74]. Copyright 2000, Springer.	51
Figure 3-4 The ferrocene/ferricenium redox couple. Reprinted with permission from [78]. Copyright 2008 American Chemical Society.	53
Figure 4-1 Simplified scheme of the electronic processes of organic molecules and oligomers. Plain arrows represent radiative decays and dashed arrows represent non-radiative decays. Reproduced with permission from [84].	59
Figure 4-2 State diagram of singlet and triplet states. Solid lines represent radiative decay channels whereas dotted lines represent the non-radiative decay channels. Reproduced with permission from [90]. Copyright 2009, Elsevier.	60
Figure 4-3 Schematic diagram of the fluorescent and phosphorescent transitions for host-guest systems. Adapted with permission from [94]. © 2002 IEEE.	61
Figure 4-4 Scheme of the five d orbitals, reprinted with permission from [101]. Copyright 2004 Wiley and Sons.	63
Figure 4-5 Scheme of the tetrahedral complex geometry (on the right) and scheme of the tetrahedral configuration (on the left).	64
Figure 5-1 Chemical structure of PVK.	68
Figure 5-2 Representation of a) face-to-face conformation and b) side-by-side conformation of PVK. Reproduced with permission from [113]. Copyright 2006 American Chemical Society.	69
Figure 5-3 Absorption, electroluminescence and photoluminescence spectra of PVK. PL and absorption spectra are from a thin film of 1 wt. % PVK in chlorobenzene. The EL spectra is from a ITO/PEDOT:PSS/PVK/Ca/Al device.	69
Figure 5-4 Chemical structure of TFB.	71
Figure 5-5 Absorption, electroluminescence (for not annealed and annealed devices) and photoluminescence spectra of pure TFB from a thin film of 2 wt. % in p-xylene.	72
Figure 5-6 Chemical structure of TPBi.	73
Figure 5-7 Absorption and PL spectra of pure TPBi from 30 nm thin-film (sublimed)	74
Figure 5-8 Current density (filled squares) and luminance (empty squares) function of the voltage for a ITO/PEDOT:PSS/PVK/Ca/Al device, thin film spun from PVK 1 wt.% in CB.	75
Figure 5-9 Absorption comparison between NANR (Not Annealed Not Rinsed), ANR (Annealed Not Rinsed) and AR (Annealed and Rinsed) samples of TFB (thin film of 2 wt.% in p-xylene) a) as measured and b) normalised.	76
Figure 5-10 Absorption, PL and EL spectra of TFB/PVK samples. EL spectra of a ITO/PEDOT:PSS/TFB/PVK/Ca/Al device. All films were spun from a 2 wt. % TFB solution in p-xylene and a 1 wt. % PVK solution in chlorobenzene.	77
Figure 5-11 Comparison of a) the absorption b) the PL and c) the EL spectra of TFB, PVK and TFB/PVK in thin films and d) energy level of TFB and PVK compared to the work function of ITO, PEDOT:PSS, calcium and aluminum. The HOMO and LUMO levels of TFB and PVK were determined by cyclic voltammetry at UCL as described in the text and in part 3.7.4. Other values are from literature [148].	78
Figure 5-12 Current-voltage-light characteristics of a ITO/PEDOT:PSS/TFB/PVK/Ca/Al device (circles) compared to a ITO/ PEDOT:PSS/PVK/Ca/Al device (squares). The current densities are represented by filled symbols and luminances by empty symbols.	79

Figure 5-13 Absorption, photoluminescence and electroluminescence spectra of PVK/TPBi. All spectra are from a thin film of 1 wt. % PVK in chlorobenzene and 30 nm thick evaporated layer of TPBi. The EL spectrum is from a ITO/PEDOT:PSS/PVK/TPBi/Ca/Al device.	81
Figure 5-14 Comparison of a) the absorption b) the PL and c) the EL spectra of PVK, TPBi and PVK/TPBi in thin films and d) energy level of PVK and TPBi compared to the work function of ITO, PEDOT:PSS, calcium and aluminum. The EL of TPBi is not shown since no data are available The HOMO and LUMO levels of PVK were determined by cyclic voltammetry at UCL as described in the text and in part 3.7.4. Other values are from literature [145, 148].	82
Figure 5-15 Current-voltage-light characteristics of a ITO/PEDOT:PSS/PVK/TPBi/Ca/Al device (circles) compared with pure PVK devices (squares). The current densities are represented by filled symbols and luminances by empty symbols.	83
Figure 5-16 Absorption, photoluminescence and electroluminescence spectra of TFB/PVK/TPBi. All spectra are from a thin film of 2 wt. % TFB in p-xylene, 1 wt. % PVK in chlorobenzene and 30 nm thick evaporated layer of TPBi. The EL spectrum is from a ITO/PEDOT:PSS/TFB/PVK/TPBi/Ca/Al device.	84
Figure 5-17 Comparison of a) the absorption b) the PL and c) the EL spectra of TFB, PVK, TPBi and TFB/PVK/TPBi in thin films and d) energy level of TFB, PVK and TPBi compared to the work function of ITO, PEDOT:PSS, calcium and aluminum. The HOMO and LUMO levels of TFB and PVK were determined by cyclic voltammetry at UCL as described in the text and in part 3.7.4. Other values are from literature [145, 148].	85
Figure 5-18 Current-voltage-light characteristics of a ITO/PEDOT:PSS/TFB/PVK/TPBi/Ca/Al device (circles) compared with pure PVK device (squares). The current densities are represented by filled symbols and luminances by empty symbols.	87
Figure 6-1 Flattening process of a Cu(I)-complex upon excitation. Reproduced with permission from [151].	89
Figure 6-2 Absorption spectra of the compound in dichloromethane solution [data from WWUM].	91
Figure 6-3 Photoluminescence spectra of the compounds in deoxygenated dichloromethane solution at room temperature [Data from WWUM].	92
Figure 6-4 Energy diagram of the materials used in this chapter compared with the work functions of the electrodes. The HOMO and LUMO levels of A, B, C, D, E and G were determined by cyclic voltammetry at WWUM and TFB and PVK at UCL, the errors on the values are represented. No LUMO data are available for B and C. Other values were taken from literature [145, 148].	96
Figure 6-5 Triplet energy E_T of each compound. The values of the triplet energy and the dimer emission energy (2.5 eV) of PVK has been taken from [120], TFB from [142], TPBi from [107].	96
Figure 6-6 EL spectra comparison between PVK/TPBi and TFB/PVK/TPBi devices.	105
Figure 6-7 a) Electroluminescence spectra and b) EQE versus current density of pure PVK (dashed line), PVK with 25 wt. % of A, C, E and G with the structure ITO/PEDOT:PSS/TFB/PVK:triplet/TPBi (30 nm)/ Ca (30 nm)/Al (150 nm).	106
Figure 6-8 a) Electroluminescence spectra, b) current-voltage-light characteristics, c) EQE versus current density and d) CIE coordinates of the devices made with the structure ITO/PEDOT:PSS/TFB/PVK:A/ TPBi (30 nm)/Ca (30 nm)/Al (150 nm) with concentration of A of 0 (dashed line), 25, 30, 35 and 40 wt. %.	108
Figure 6-9 Absorption (black line) and PL spectra of pure A 1wt.% in chlorobenzene (black dashed line).	109

Figure 6-10 Time resolved photoluminescence spectra with a pulsed laser beam at 371 nm entering from the polymer side. Emission at 520 nm.....	110
Figure 6-11 a) Absorption and PL (dashed line) spectra of A:PVK. 25 wt. % of A in PVK and overall concentration of 1 wt.% in CB. b) Comparison between the PL of PVK (grey line), A (grey dashed line) and PVK:A (black line).....	111
Figure 6-12 Time resolved photoluminescence spectra with a pulsed laser beam at 371 nm entering from the polymer side.	112
Figure 6-13 Absorption spectra of PVK and A. The excitation wavelength of 371 nm used for the lifetime measurements is indicated in grey.....	113
Figure 7-1 Absorption spectra of 1 wt. % PVK in CB and in THF measured from thin film.	118
Figure 7-2 Comparison between the electroluminescence spectra of PVK in CB (plain line) and in THF (dashed line) normalised a) on the integral b) on the maximum of the first emission peak.....	118
Figure 7-3 Current density (filled symbols) and luminance (empty symbols) of the devices ITO/PEDOT:PSS/PVK/Ca/Al spin-coated from chlorobenzene (circles) and from THF (squares).....	120
Figure 7-4 Atomic force microscopy of PVK spin-coated from CB (left) and from THF (right) on ITO substrates covered with an 80 nm thick PEDOT:PSS layer and snapshots of the electrodes (bottom row).	121
Figure 7-5 Comparison between the electroluminescence spectra of PVK/TPBi with PVK spin-coated from CB (plain line) and THF (dashed line).	122
Figure 7-6 Current density (filled symbols) and luminance (empty symbols) of the ITO/PEDOT:PSS/PVK/TPBi/Ca/Al devices spin-coated from CB (circles) and from THF (squares).....	123
Figure 7-7 Comparison of the current density of PVK:G 25 wt. % spin-coated from CB (circles) and from THF (squares).	124
Figure 7-8 Atomic force microscopy of PVK:G spin-coated from CB (left) and from THF (right) on ITO substrate covered with a 80 nm thick PEDOT:PSS layer. The images with the 4 μm scale bar show the amplitude of the vibrating AFM probe (not the topography).....	124
Figure 7-9 Snapshots of the electrodes on films of PVK:G spin-coated from CB (left) and THF (right).....	125
Figure 8-1 Chemical structure of TBST.	130
Figure 8-2 Chemical structure of F8BT, MDMO-PPV and P3HT.	131
Figure 8-3 Absorption, Electroluminescence and Photoluminescence spectra (excitation at 325 nm for F8BT and 412 nm for MDMO-PPV) of thin films of a) F8BT, b) MDMO-PPV and c) TBST spin-coated from toluene.....	133
Figure 8-4 Energy diagram of the materials used in these experiments compared with the work functions of the electrodes. The HOMO and LUMO levels of TBST, F8BT and MDMO-PPV were determined by cyclic voltammetry at UCL as described in the text and in part 3.7.4. Other values are from literature [148]. The error on F8BT and MDMO-PPV values are represented.....	134
Figure 8-5 Current-voltage-light characteristics of pure material devices a) F8BT, b) MDMO-PPV and c) TBST.....	135
Figure 8-6 Absorption spectrum of TBST compared with the photoluminescence spectra of F8BT (dashed line) and MDMO-PPV (dotted line) in thin films spin-coated from toluene solutions.....	136

Figure 8-7 Current-voltage-light characteristics of blend devices: F8BT:TBST 5 wt. % (squares), MDMO-PPV:TBST 5 wt. % (circles). The current densities are represented by filled symbols and light outputs by empty symbols.	137
Figure 8-8 Current-voltage-light characteristics of blend devices a) F8BT:TBST and b) MDMO-PPV:TBST for the different concentrations of TBST (1, 2, 3 and 5 wt. %) compared to the pure material devices. The current densities are represented by filled symbols and light outputs by empty symbols.	137
Figure 8-9 Effect of TBST concentration on the electroluminescence spectra of a) F8BT:TBST and b) MDMO-PPV:TBST with TBST concentration from 1 to 5 wt. %.	139
Figure 8-10 EQE plotted as a function of TBST for 1 wt. % to 5 wt. % TBST in a) F8BT and b) MDMO-PPV.	140
Figure 8-11 Energy diagram of the materials used in these experiments compared with the work functions of the electrodes. The HOMO and LUMO levels of TFB, TBST and F8BT were determined by cyclic voltammetry at UCL as described in the text or in part 3.7.4. Other values are from literature [148]. The error on TFB and F8BT values are represented.	141
Figure 8-12 Comparison of the electroluminescence spectra of a F8BT device and a TFB/F8BT device.	141
Figure 8-13 Time resolved photoluminescence spectra of F8BT and TFB/F8BT devices at 550 nm excited with a pulsed laser beam picked at 371 nm, of 270 ps duration entering from the polymer side.	142
Figure 8-14 Current-voltage-light characteristics of TFB/F8BT devices (circles) compared to F8BT devices (squares). The current densities are represented by filled symbols and light outputs by empty symbols.	144
Figure 8-15 Current-voltage-light characteristics of TFB/F8BT:TBST 5 wt. % blend devices (circles) compared with F8BT:TBST 5 wt. % devices (squares) The current densities are represented by filled symbols and light outputs by empty symbols.	145
Figure 8-16 Effect of TBST concentration on the electroluminescence spectra of F8BT:TBST with a TFB interlayer.	145
Figure 8-17 EQE plotted as a function of TBST concentration for 1 to 5 wt. % TBST.	146
Figure 8-18 Energy diagram of the materials used in these experiments compared with the work functions of the electrodes. The HOMO and LUMO levels of TBST, F8BT and P3HT were determined by cyclic voltammetry at UCL as described in the text and in part 3.7. Other values are from literature [148]. The errors on F8BT and P3HT values are represented.	147
Figure 8-19 EL spectra of a F8BT:P3HT 5 wt. % blend compared with pure F8BT.	147
Figure 8-20 Current-voltage-light characteristics of F8BT:P3HT 5 wt. % :TBST 0, 1, 2,5 and 10 wt. % blend devices. The current densities are represented by filled symbols and light outputs by empty symbols.	148
Figure 8-21 Effect of TBST concentration on the electroluminescence spectra of F8BT:P3HT 5 wt. %.	149
Figure 8-22 EQE plotted as a function of TBST concentration for 1 to 10 wt. % TBST.	150
Figure 9-1 Chemical structure of the compounds HAT-TIPS and HAT-TIBS – data from University of Freiburg.	152
Figure 9-2 Packing of the molecule HAT-TIPS, one can see the twist of the aromatic core as well – data from University of Freiburg.	152
Figure 9-3 Packing of the molecule HAT-TIBS, one can see the twist of the aromatic core as well – data from University of Freiburg.	153

Figure 9-4 Absorption spectra of HAT-TIPS and HAT-TIBS spin-coated from a 2.5 wt. % toluene solution	154
Figure 9-5 Photoluminescence spectra of HAT-TIPS and HAT-TIBS spin-coated from a 2.5 wt. % solution in toluene measured with a 325 nm laser and the ANDOR.....	155
Figure 9-6 Energy diagram of the materials used in the experiments compared with the work functions of the electrodes. The HOMO and LUMO levels of HAT-TIPS and HAT-TIBS were determined at Freiburg University. Other values are from literature [148].	156
Figure 9-7 Current-voltage-light characteristics of pure HAT-TIPS (squares) and HAT-TIBS (circles) devices. The current densities are represented by filled symbols and light outputs by empty symbols.	156
Figure 9-8 Energy diagram of the materials used in these experiments compared with the work functions of the electrodes. The HOMO and LUMO levels of HAT-TIPS and HAT-TIBS were determined at Freiburg University and TFB at UCL, the errors on the values of TFB are represented. Other values are from literature [148].	157
Figure 9-9 a) EL spectra and b) Current-Voltage-Light characteristics of HAT-TIPS (squares) and HAT-TIBS (circles) devices containing TFB as an interlayer. The current densities are represented by filled symbols and light outputs by empty symbols.	158
Figure 9-10 Comparison of the absorption spectra of a) TFB, HAT-TIPS and TFB:HAT-TIPS and b) TFB, HAT-TIBS and TFB:HAT-TIBS	160
Figure 9-11 Photoluminescence spectra (excitation at 325 nm) of a) HAT-TIPS and b) HAT-TIBS blended with TFB. The PL of the pure materials are also represented for comparison purpose.	161

List of tables

Table 3-1 HOMO-LUMO energy levels of commercial polymers and small molecules measured at UCL.	55
Table 5-1 Summary of the photophysical data of PVK.	70
Table 5-2 Summary of the photophysical data of TFB.	72
Table 5-3 Summary of the photophysical data of TPBi.	74
Table 5-4 Summary of the properties of the ITO/PEDOT:PSS/PVK/Ca/Al devices in average.	75
Table 5-5 Summary of the photophysical data of TFB/PVK.	79
Table 5-6 Summary of the properties of the ITO/PEDOT:PSS/TFB/PVK/Ca/Al devices in average compared to pure TFB (annealed devices) and pure PVK devices.	80
Table 5-7 Summary of the photophysical data of PVK/TPBi.	83
Table 5-8 Summary of the properties of the ITO/PEDOT:PSS/PVK/TPBi/Ca/Al devices in average compared to pure PVK devices.	84
Table 5-9 Summary of the photophysical data of TFB/PVK/TPBi.	86
Table 5-10 Summary of the properties of the ITO/PEDOT:PSS/TFB/PVK/TPBi/Ca/Al devices in average compared to pure TFB, pure PVK, TFB/PVK and PVK TPBi devices.	86
Table 6-1 Cu(I)-complexes, synthesized at WWUM.	90
Table 6-2 Photophysical and electrochemical data of the new Cu(I)-complexes. Data from WWUM.	94
Table 6-3 Properties of the ITO/PEDOT:PSS/PVK:copper complex/TPBi/Ca/Al devices over a range of triplet compositions.	98
Table 6-4 Electroluminescence spectra, current-voltage-light characteristics, EQE versus current density of the devices made with the structure ITO/PEDOT:PSS/PVK:triplet/TPBi (30 nm)/Ca (30 nm)/Al (150 nm).	99
Table 6-5 CIE coordinates of the devices for the different concentrations.	101
Table 6-6 Properties of the ITO/PEDOT:PSS/TFB/PVK:copper complex/TPBi/Ca/Al devices in average.	105
Table 6-7 Properties of the ITO/PEDOT:PSS/TFB/PVK:A/Ca/Al devices over a range of triplet concentrations.	107
Table 6-8 Summary of the photophysical data of A.	110
Table 6-9 Summary of the photophysical data of A:PVK.	112
Table 7-1 Summary of the properties of the ITO/PEDOT:PSS/PVK/Ca/Al devices in average for PVK spin-coated from CB and THF solutions.	119
Table 7-2 Summary of the properties of the ITO/PEDOT:PSS/PVK/TPBi/Ca/Al devices in average for PVK spin-coated from CB and THF solutions.	123
Table 8-1 Optical properties (from solution in CHCl ₃) and polymer parameters for TBST (data from University of Wuppertal).	131

Table 8-2 A summary of the principle properties of the ITO/PEDOT:PSS/F8BT or MDMO-PPV or TBST/Ca/Al devices in average.....	135
Table 8-3 Properties of the devices over a range of TBST compositions. The last column shows the percentage of emission of the materials in the different blends [F8BT (<650 nm), MDMO-PPV (<740 nm)].	138
Table 8-4 A summary of the principle properties of the ITO/PEDOT:PSS/TFB/F8BT/Ca/Al devices in average and compared to pure F8BT devices.	143
Table 8-5 Properties of the ITO/PEDOT:PSS/TFB/F8BT:TBST/Ca/Al devices over a range of TBST compositions. The last column shows the percentage of emission of the materials in the different blends [TFB F8BT (<670 nm)].	144
Table 8-6 A summary of the main properties of the ITO/PEDOT:PSS/F8BT:P3HT 5 wt. %/Ca/Al devices in average.....	147
Table 8-7 Properties of the ITO/PEDOT:PSS/F8BT:P3HT:TBST/Ca/Al devices over a range of TBST compositions. The last column shows the percentage of emission of the materials in the different blends [F8BT:P3HT 5 wt. % (<710 nm) (<720 nm for 1 wt. % TBST)].	148
Table 9-1 Properties of the ITO/PEDOT:PSS/TFB/HAT-TIPS or HAT-TIBS/Ca/Al devices in average.....	159

***Part I. Introduction &
Scientific Background***

1 Introduction

Organic light-emitting diode (OLED) is a fast growing technology based on the principle of electroluminescence. Electroluminescence was first reported in organic semiconductors by Pope et al. in 1963 [1], but the commercial potential was not realised until 1987 when Tang and VanSlyke of Kodak reported efficient low voltage electroluminescence in an organic thin-film device [2]. Later Friend and co-workers reached a new milestone by incorporating polymers instead of small molecules as the emitting layer [3]. Since these discoveries tremendous progress has been made in materials and manufacturing techniques and today several companies are sharing the lucrative market of producing OLED displays. They are mostly used in mobile phones, MP3 players and even televisions. The total annual sales are over \$ 1 billion [4] and billions of dollars are, still, invested in the development of this technology.

OLED technology offers many advantages over traditional liquid crystal displays (LCDs) and plasma screens. First of all their design is much simpler thanks to the fact that OLED displays are self-luminescent. No backlighting and colour filters are thus required allowing thinner and lighter devices. Since no backlighting is needed and no power is drawn by black OLED pixels, OLED displays required lower power consumption than LCDs. Besides the colour of an OLED can be tuned easily and thus filters are no longer needed. Furthermore, OLEDs are exhibiting better response time (0.01 ms against 2 ms), better contrast and better viewing angles and offer the possibility of transparent, thin and flexible screens opening the way to new applications. However, the biggest challenges OLEDs manufacturers must face are their degradation in air making high quality encapsulation compulsory and the upscaling needed to enter mass production.

However, despite the successful commercialization of OLED displays and lighting products, many aspects are not well-understood and researchers are, still, working on new materials, processes and explanations.

After introducing in part I the theoretical background needed to understand the present work (chapter 2) and the experimental techniques (chapter 3), the optoelectronic properties of some new materials are presented in parts II and III.

Part II focuses on phosphorescent OLEDs based on transition metal complexes synthesised by Claudia Bizzarri from the University of Münster (Germany), group of Luisa De Cola. These complexes have the particularity of incorporating copper, allowing cheap and non-toxic electroluminescent materials with relatively short excited-state lifetimes, high emission quantum yields and appropriate HOMO/LUMO energies. The polymeric matrix, the hole and electron injection layer were extensively investigated (chapter 5) in an attempt to explain the photophysical properties of the devices (chapter 6). Eventually chapter 7 focuses on the importance of the choice of the solvent.

Finally part III concentrates on near-infrared devices. In chapter 8, a near-infrared emitting copolymer, synthesized by Dietrich Breusov from the University of Wuppertal (Germany), group of Ulrich Scherf is studied in several polymeric hosts. And in chapter 9 near infrared emission was obtained using twisted molecules synthesized by Sunil Choudhary, University of Freiburg (Germany); group of Aurelio Mateo Alonso, molecules which originally emit in the visible.

2 From π -conjugated materials to devices

2.1 π -conjugated materials

Organic electronics is based on π -conjugated materials that are organic materials based on carbon and hydrogen atoms, in other words, hydrocarbons. The electronic structure of a carbon atom is $1s^2 2s^2 2p^2$. According to the valence bond theory, in π -conjugated materials carbon atoms present a sp^2 hybridization resulting from the merging of the 2s orbital with two 2p orbitals ($2p_x$ and $2p_y$). The last 2p orbital ($2p_z$) is not hybridized and forms a π bond. The three axes of the sp^2 orbitals are all in the same plane and thus form a planar molecule with angles of 120° (see Figure 2-1).

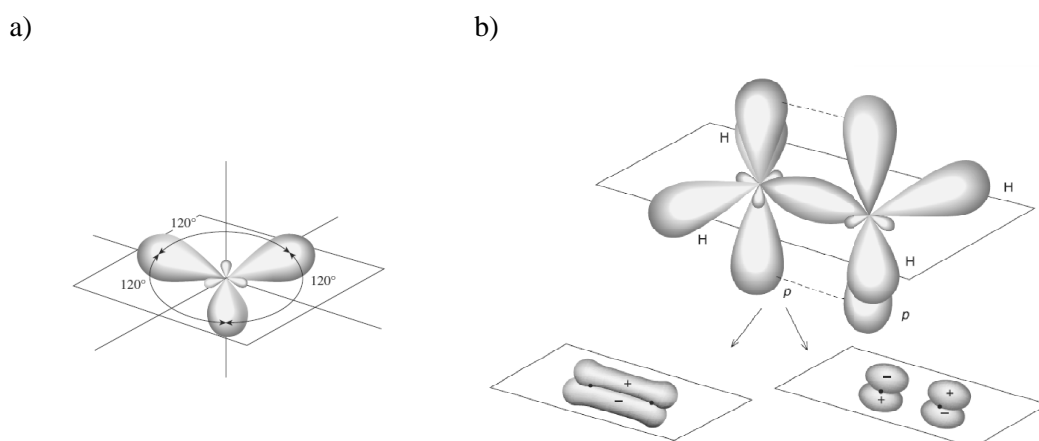


Figure 2-1 a) Representation of the three sp^2 orbitals b) Representation of the overlap of the p orbitals forming a π and π^* orbital. The σ orbitals are shown in the upper figure, but have been removed from the bottom picture for clarity. Reprinted with permission from [5]. Copyright © 2007, John Wiley and Sons.

If we now consider the ethylene molecule ($\text{CH}_2=\text{CH}_2$) formed by two carbon atoms presenting sp^2 orbitals, we find that the carbon-hydrogen bonds arise from the sp^2 orbitals and the two carbon atoms form two different bonds: one from the sp^2 orbital and the other from the $2p_z$ orbital.

The overlapping of two sp^2 atomic orbitals generates two new molecular orbitals, a bonding orbital σ and an antibonding orbital σ^* . The bonding orbital has a lower energy

than the original atomic orbital and the antibonding orbital has a higher energy and remains empty in the ground state. Due to the large overlap of the atomic orbitals sp^2 , the molecular orbitals σ are very stable and give rigidity to the molecule. As a consequence it is very difficult to excite an electron to the σ^* orbital.

The p_z orbital is perpendicular to the plane of the sp^2 orbitals (see Figure 2-1). The two parallel $2p_z$ orbitals of the molecule overlap to generate two new orbitals, a bonding (π) orbital and an antibonding (π^*) orbital. Due to the small overlapping of the atomic orbitals $2p_z$, the molecular orbitals π and π^* are close in energy.

Thus the distance between the Highest Occupied Molecular Orbital (HOMO) and the Lowest Unoccupied Molecular Orbital (LUMO) is reduced in the presence of π bonds. The resulting energy gap is of such magnitude that the materials are then considered semiconductors.

When a molecule is conjugated, that is when there is a sequence of alternating double and single bonds, the π electrons are no longer localised in specific double bonds between two particular carbon atoms but are spread out, or delocalised. Benzene is a common example of this phenomenon (see Figure 2-2).

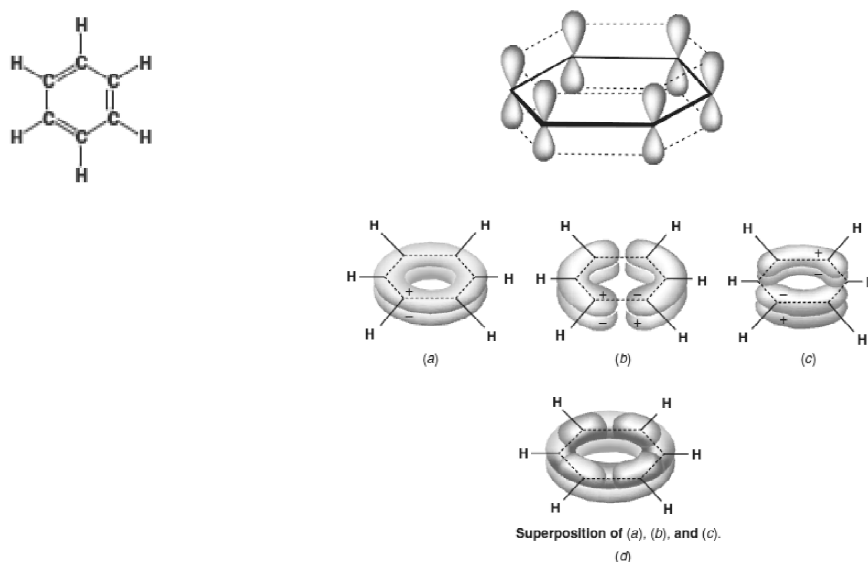


Figure 2-2 On the left, chemical structure of benzene and on the right, the six p orbitals of benzene overlap to form three bonding orbitals (a), (b) and (c). The three orbitals superimposed are shown in (d). Reprinted with permission from [5]. Copyright © 2007, John Wiley and Sons.

Due to this delocalization, the energy levels of π and π^* associated with the double bonds are modified and the molecule is stabilized. When the number of carbon atoms is increased, the delocalization of the π and π^* orbitals become longer and thus the energy difference between π and π^* decreases. The band model in which the two bands are called HOMO (π) and LUMO (π^*) can be approximated. The energy difference between the HOMO and the LUMO is called bandgap. The approximation is particularly accurate for defect-free and highly-ordered crystals of conjugated 'small' molecules. Conjugated polymers on the other hand are often considered rather unordered so that hopping transport often provides a more precise description of charge transport phenomena.

In the present thesis, the large majority of materials used are conjugated materials. Conjugated materials are generally divided into two categories: small molecules and polymers. Small molecules are mostly defined as low molecular mass materials and can be thermally-evaporated or solution-processed (for the soluble ones) whereas polymers are long chains of molecules which are solution-processed. Solution processing offers the possibility of large area low cost production but at the moment thermally-evaporated devices exhibit better characteristics than solution-processed ones.

In organic electronics not only are intramolecular interactions of tremendous importance but intermolecular interactions have to be taken into account as well. These interactions are of a different nature and are introduced in part 2.8.

2.2 What is an Organic Light-Emitting Diode?

An Organic Light-Emitting Diode (OLED) is basically a thin film of 100 to 150 nm of organic material sandwiched between two electrodes. Organic electroluminescent materials are all based on π -conjugated molecules (see part 2.1) and are not highly conductive [6]. Charge carrier density is obtained when an electron is added or removed (reduction or oxidation), indeed, this extra electron or missing electron (hole) installed on a π or π^* orbital can easily relocate along the molecule thus creating a very efficient

transport limited to the molecule dimension or several molecular units for the case of conjugated polymers. But to cross thick barriers, electron and hole have to jump [7] limiting the mobility. Light is produced by the recombination of holes and electrons which are injected at the electrodes. When a voltage is applied between the electrodes, charges are injected into the organic material: holes from the anode and electrons from the cathode. Then, the charges move inside the material, generally by hopping processes and then recombine to form excitons (see Figure 2-3). The location of the recombination zone in the diode differs according to the charge mobilities and the injection barriers. After diffusion, either the exciton recombines radiatively emitting a photon or decays non-radiatively.

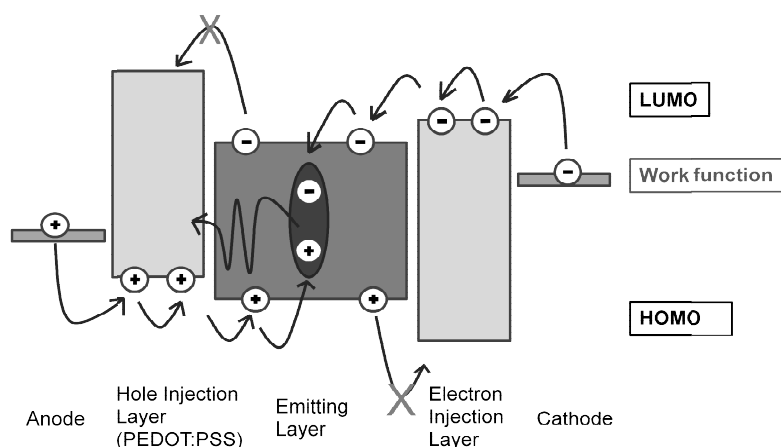


Figure 2-3 Energy level scheme of an OLED with applied bias.

The colour of the photon depends on the energy difference between the highest occupied molecular orbital (HOMO) and the lowest unoccupied molecular orbital (LUMO) levels of the electroluminescent molecule. The wavelength of the light emission can thus be controlled by the extent of the conjugation in the molecule/polymer. For efficient hole injection from the anode, a low barrier is required in respect of the HOMO level of the organic material (typically 5-6 eV). ITO is usually used as an anode because of its high work function as well as its good transparency in the visible region. On the cathode side, a low barrier for electrons is needed in respect of the LUMO level of the organic material (typically 2-3 eV). This criterion is fulfilled by low work function metals such as calcium, silver and aluminium.

With only one layer between the cathode and the anode, yields are very low. Indeed, the mobility of charge carriers within the same material is usually very different, holes typically have a higher mobility than electrons [8]. Indeed electrons are easily trapped in presence of oxygen [9]. Therefore, the recombination zone is located near the cathode leading to a diminution of the device efficiencies because of non-radiative deexcitation at the interface. One of the solutions applied in this work is the use of interlayers. All devices have been made with the following type of structure (Figure 2-4) with or without interlayers:

Al
Ca (30 nm)
Interlayer
Active layer (100 nm)
Interlayer
PEDOT:PSS (80 nm)
ITO
Glass

Figure 2-4 Schematic of the sandwich structure OLED.

2.3 Experimental steps of the fabrication of an OLED

2.3.1 ITO substrates and oxygen plasma treatment

The substrates were made of glass covered with an indium tin oxide (ITO) layer (~150 nm thick) already conveniently etched by Visiontek Systems LTD. ITO is widely used in organic electronic because of its good transparency (transmission of 90 % in the visible [10]), high conductivity and high efficiency as a hole injector into organic materials [11]. It is usually deposited by sputtering, evaporation or pulsed laser deposition [12-14].

The first steps in the fabrication process were the cleaning of the ITO substrate and the oxygen plasma treatment in order to further clean the surface from impurities, increase the work function, lower the sheet resistance of the electrode and increase the

surface polarity enabling a good adhesion with polar polymers [11]. Oxygen plasma techniques are used since the late 1950s to remove organics in vacuum deposition techniques [15]. Plasmas are generated at subatmospheric pressures of oxygen and create highly reactive ions that bombard the surface and react with organics forming volatile species such as CO. The effect of oxygen plasma was investigated by several groups [10, 11, 14] and they always concluded on the tremendous importance of this step in the fabrication of stable and efficient OLEDs.

2.3.2 PEDOT:PSS

PEDOT:PSS (Poly(3,4-ethylenedioxythiophene):poly(styrenesulfonic acid)) (Figure 2-5) was subsequently spin-coated on the top of the treated ITO.

PEDOT is a polymer that is insoluble in water and that exhibits: high conductivity (ca. $550 \text{ S}\cdot\text{cm}^{-1}$ [16]), good thin-film transparency, and high stability in its oxidised state. To overcome the low solubility of pure PEDOT, a colloidal suspension in water containing poly(styrene sulfonic acid) (PSS) is added. PEDOT:PSS presents good film-forming properties, a conductivity of ca. $10 \text{ S}\cdot\text{cm}^{-1}$, high visible-light transmission, and relatively good stability [16].

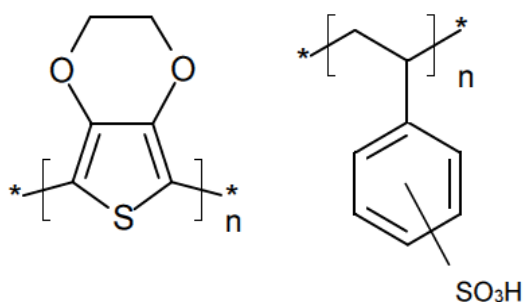


Figure 2-5 Structure of PEDOT (left) and PSS (right).

PEDOT:PSS serves as an ameliorating coating for indium tin oxide (ITO) as it allows to overcome a lot of the drawbacks of ITO by raising its work function (from 4.8 eV to 5.2 eV [17]), improving the adhesion of the organic layers and reducing its surface roughness by forming a smooth layer and thus preventing electrical shorts. It is also

reported that its use reduces the batch to batch variability and enhances the operating lifetimes and efficiencies [18-21].

However, PEDOT:PSS presents some drawbacks such as its chemical interactions with some organic materials and ITO due to its acidic nature [22] as well as its degradation when it is forced to pass an electron (as opposed to hole) current. Furthermore, exciton quenching is occurring at the interface between PEDOT:PSS and the active layer which leads to a decrease in the efficiency of the devices [23]. One solution to counter this problem is to use electron-blocking/hole-transporting interlayer between PEDOT:PSS and the active layer [18].

PEDOT:PSS is available commercially with different ratio of PEDOT and PSS and in different concentration. In this thesis, a 2.8 wt. % dispersion of PEDOT:PSS purchased from Sigma-Aldrich was used with a PEDOT content of ~0.14 % and PSS content of ~2.6 %.

After the deposition of the PEDOT:PSS films via spin-coating the samples were annealed in nitrogen atmosphere at 180°C for 10 minutes leading to 80 nm films. If the film of PEDOT:PSS would have been dried in air it would have uptaken water again. The release of water in functional devices would be a severe source of degradation as water might corrode the metallic contacts or oxidize the adjacent organic layer [19].

2.3.3 Active layer and interlayer

The active layer was subsequently spin-coated. The polymer/small molecule needs to dissolve in the chosen solvent and the film formed by spin-coating needs to be pinhole-free. The concentration and the solvent need to be chosen carefully in order to obtain the desired thickness of 100 nm. The layer thicknesses were measured with a mechanical profilometer (Dektak).

Hole-transporting interlayers physically separate PEDOT:PSS from the active layer and thus prevent electrons from passing through PEDOT:PSS as well as chemical interactions between PEDOT:PSS and the active layer.

Ideally hole-transporting layers (HTL) present high hole mobilities, a HOMO level close to the work function of PEDOT:PSS for an easy hole injection and a high LUMO to block electrons [18].

Electron-transporting layers (ETL) can be used on top of the active layer to help the injection and the transport of electrons and in most cases to act as a hole-blocking layer as well.

2.3.4 Cathode

The top electrode consisted of calcium capped with aluminium and was deposited via thermal evaporation at a pressure of $\sim 10^{-6}$ mbar and with an evaporation rate between 0.4 and 2 Å/s.

Deposition rates are monitored by a quartz crystal monitor that oscillates at a resonance frequency which is dependent on the mass and, therefore, on the thickness of the film deposited onto it. For OLEDs the most common cathode is calcium capped with aluminium to prevent its oxidation.

During the evaporation of calcium, the high vacuum allows vapour particles to travel directly to the cooled substrate where they condense back to a solid state. The calcium atoms reach the polymer film with enough thermal energy to migrate and diffuse into the polymer surface. During this process the metal forms Ca^{2+} ions and donates electrons to the π -system of the polymer. In case of a large amount of oxygen on the surface or in the atmosphere, a layer of calcium oxide is formed [24]. The interfacial region between the polymer and the metal layer is estimated to be between 2 and 4 nm thick [25, 26].

The same evaporation technique was used for the deposition of aluminium and the organic layers.

2.4 Charge injection

The first step to obtain emission of light from an OLED is the injection of charge carriers into the device. These charges (electron and holes) need to overcome the energetic barrier formed at the interface metal/organic material. This is the reason why high work function anodes and low work function cathodes are desirable.

The two main attempts to model the injection of charges in organic materials are the Richardson-Schottky thermionic emission and the Fowler-Nordheim tunnelling [27, 28] that were initially developed for inorganic materials. The different models are more detailed by Braun in [29].

The Richardson-Schottky model is based on the assumption that an electron from the metal can be injected once it has acquired a thermal energy sufficient to cross the barrier. It is dependent on the temperature and the electric field applied.

The Fowler-Nordheim model ignores image charge effects and assumes tunnelling of electrons independent of the temperature. This model is used for high metal/organic barriers whereas the Richardson-Schottky model is used for low metal/organic barriers.

However, it is difficult to extend these models from bandtype materials to disordered organic materials where mobilities are low and charge carriers are localised. Researchers are thus, still, working on improving or developing models for charge injection [30-34].

2.5 Importance of the interfaces

As seen in the previous part, the injection of charge carriers depends on the metals used for the electrodes and the HOMO/LUMO of the materials. However, interface mechanisms with organic materials are complicated to predict due to the morphology of the films and the fact that the molecules can be polarised.

Ultraviolet Photoemission Spectroscopy (UPS) measurements have shown that dipoles are created when the materials are brought into contact (see Figure 2-6) and thus invalidate the vacuum level alignment rule (the vacuum level of the materials

aligned on contact) [35, 36]. The formation of this dipole is due to different mechanisms such as chemical reaction, polarization at the metal interface, formation of gap states in the organic material, orientation of molecular dipoles, etc. [37, 38]. These dipoles could modify the energetic barrier from 0.5 to 1 eV.

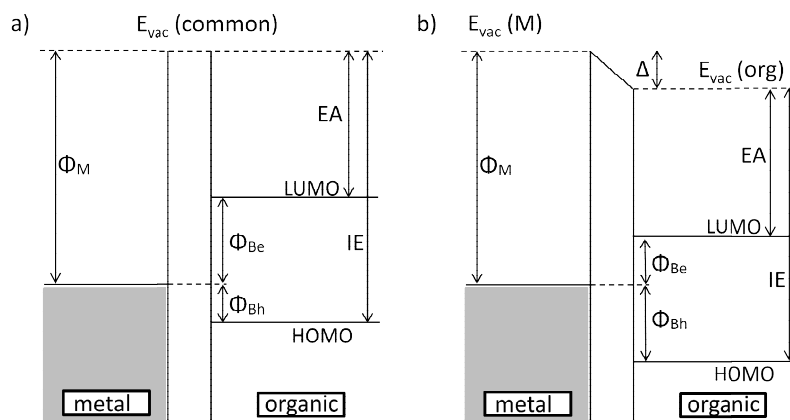


Figure 2-6 Metal/organic interface energy diagram a) without and b) with an interface dipole Δ . Φ_{Be} and Φ_{Bh} are the electron and hole barriers, Φ_M the metal work function, E_{vac} the vacuum levels, EA the electronic affinity and IE the ionisation energy of the organic material.

When comparing the HOMO/LUMO of materials together or with the work function of metals one must thus be aware that a dipole might be formed changing the prediction that could have been made.

2.6 Charge transport and trapping in amorphous organic materials

Charge transport in amorphous organic materials, in which charge transfer are localised on different molecular sites, is a hopping process. Charge transfer occurs between neighbouring hopping sites which can be situated on the same polymer chain (or molecule) or on a different one leading to intramolecular or intermolecular charge transport. It is assumed that in trap-free systems the distribution of energy of hopping sites is narrow and, therefore, approximately the same amount of thermal activation is needed to free charges from all the hopping sites. It should be noted that injection of charge depends on the ionization potential (I_p)/electron affinity ($\mathcal{A}e$) of the material and

the work function of the metal whereas the charge transfer is dominated by the activation energy.

The charge carrier mobility depends on the average distance and the charge transfer rate between the neighbouring hopping sites. Hole transport can be described as *“an electric field driven chain of reversible redox reactions where neutral molecules or groups will repetitively transfer an electron to their positively charged cation radical neighbours in the direction of an electric field”* [39]. This transport is not considered ionic because matter is not displaced during the process.

Trapping occurs in the presence of hopping sites that require larger energy input to release the charge carrier than the majority of hopping sites or in other words when a molecule presents a lower ionization potential (I_p)/ higher electron affinity (A_e) than the other molecules in the close surrounding.

The mechanism of trapping can then be explained by adding a very small amount of an organic material to another as Pai did in 1984 [39]. He took two organic materials with known hole mobility: TPD and PVK (see Figure 2-7). He knew that TPD presented a higher hole mobility than PVK and observed that the addition of a small amount of TPD in a PVK matrix reduced the hole mobility. The addition of more TPD further reduces the hole mobility to a minimum value and from this point onwards the addition of more TPD causes an increase in the hole mobility until it reaches the hole mobility of pure TPD. It shows that once this critical concentration is reached, charge transport occurs via TPD sites exclusively and that PVK acts as an inert matrix only. However, at low TPD/PVK ratios charge transport proceeds primarily via PVK and TPD acts as traps releasing the charge carriers slowly. The charge carrier migration will stop at the site of molecules with lower ionization potentials and will need to gain enough thermal energy to be released.

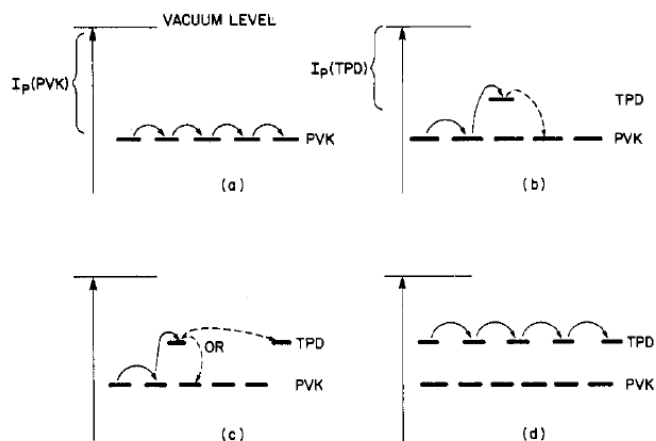


Figure 2-7 Schematics of hopping via high ionization potential compound in the presence of a low ionization potential compound: (a) hopping via high-Ip material (no dopant); (b) hopping via high-Ip material in the presence of a small amount of a low-Ip compound (trapping at the sites of low Ip); (c) hopping via both low-Ip and high-Ip material; (d) hopping via low-Ip compound exclusively. Reprinted with permission from Pai et al. [39]. Copyright © 1984 American Chemical Society.

2.7 Energy transfer: the exciton diffusion

When an electron and a hole recombine an exciton (electrically neutral quasiparticle where the bound electrons and holes are attracted to each other by the electrostatic Coulomb force) is formed. In case of organic materials, because the dielectric constant is low, the exciton is called Frenkel exciton. After its formation and before its deexcitation, an exciton can transfer its energy to a neighbour molecule. This is called the exciton diffusion.

Exciton diffusion is an energy transport process between molecules. Three different mechanisms of energy transfer were reported:

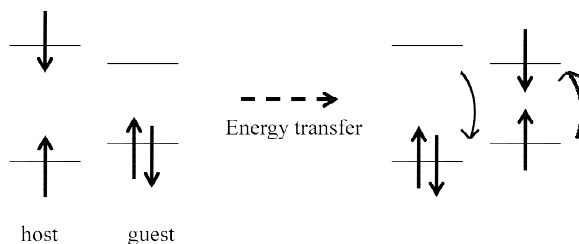
The simplest one is the trivial transfer and occurs when a donor emits a photon that is then absorbed by an acceptor. Obviously a good transfer implies that the acceptor absorbs where the donor emits.

The second one is called Förster Resonance Energy Transfer (FRET) [40] (see Figure 2-8 (a)) and assumes the exchange of a virtual photon between two point dipoles. This model is for spin-allowed optical transitions only (singlet to singlet or triplet to singlet)

and the rate mostly depends on the spectral overlap between the emission of the donor (D) and the absorption of the acceptor (A). Typical Förster radii for conjugated polymers are of the order of 4 to 10 nm. However, since excited states in conjugated polymers are not point dipoles but, in fact, extended over a nanometer or more, the dipole-dipole approximation tends to break down.

The last one is the Dexter transfer [41] (see Figure 2-8 (b)) which is an electron tunnelling exchange process. The excited electron from the donor molecule is exchanged for a ground state electron from the acceptor molecule. It requires the orbital overlap between the acceptor and the donor and is, therefore, a short range energy transfer (~1 nm) where the rate is exponentially dependent on the distance between the donor and the acceptor molecules. Similar to FRET, the rate also depends on the overlap of the donor-emission and acceptor-absorption spectra. Since it is a tunnelling transfer, electron spin is not important and the transfer can occur between both triplet or singlet states as long as the spin is conserved. In the case of a phosphorescent guest in an electroluminescent host, it is possible for the triplet exciton of the host to be transferred to the radiative triplet excitons of the guest on a very short range, resulting in highly efficient devices.

a) Förster energy transfer



b) Dexter energy transfer

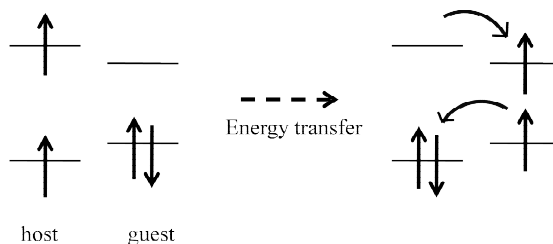


Figure 2-8 Förster and Dexter energy transfer.

2.8 Interchain interactions

When the chains of a conjugated polymer are isolated in solution, it is well accepted that photoexcitation creates only singlet intrachain excitons. However, when the polymer chains are in contact in a film, interchain interactions also take place making the interpretation of the emission spectra much more complex [42].

2.8.1 Interactions in the excited states: exciplexes, excimer and polaron pairs

In type II heterojunction [43], exciplexes are often formed and are of a particular interest as they can allow the fabrication of very efficient devices. Exciplexes result from a transfer of electronic charges between the LUMO of a donor or an acceptor and the HOMO of an acceptor or a donor respectively [44]. When the molecular components of the exciplex are the same, the excited complex is called excimer. There are molecular associates that exist only in excited electronic states and are, therefore, detectable only in emission spectra [45].

The formation of an exciplex results from the fact that a D^{*}-A complex exhibits an enhanced stabilization compared to a D-A ground state complex, which can be explained by the molecular orbital interactions (see Figure 2-9). We can see that in the case of a ground state DA pair two electrons are destabilized and two electrons are stabilized. Consequently there is no gain in energy resulting from the formation of a DA pair. Whereas in the case of a D^{*}-A exciplex one electron is destabilized and three electrons are stabilized, thus, the formation of exciplex involves a gain in energy. This comparison shows that the formation of a supramolecular complex is energetically favourable; the only problems occurring are the strength of the excimer or exciplex bonding [46].

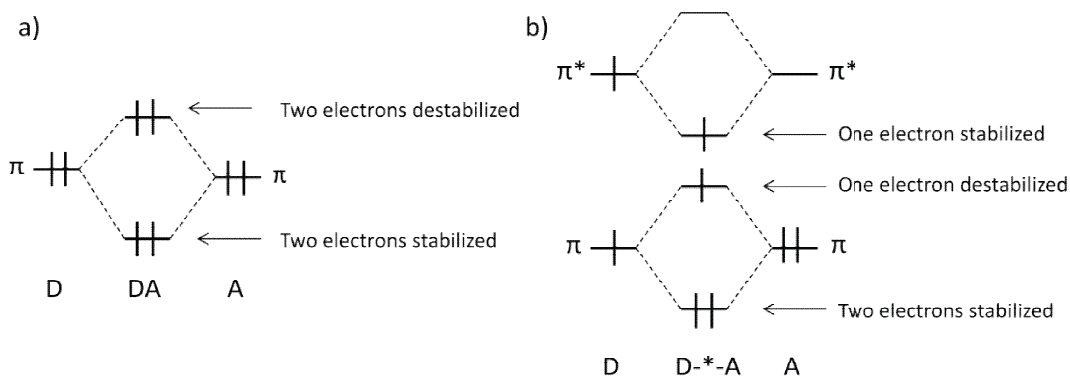


Figure 2-9 Orbital interactions of a) DA ground state pairs and b) D^{*}-A exciplexes. Reproduced with permission from Turro et al. [46]. Copyright 2009, Mill Valley, California. All rights reserved.

Since exciplexes and excimers are distinct species they possess distinct photophysical and photochemical properties. If exciplexes are present they should in principle exhibit fluorescence (singlet exciplexes) or phosphorescence (triplet exciplexes) and the emission from the exciplexes should be different from the excited species alone. The lifetime of an excimer is very short whereas exciplexes exhibit longer lifetimes than the excited species alone due to their low oscillation strength. Excimer and exciplex fluorescence both exhibit broad structureless bands at longer wavelength than the monomer fluorescence emission [47].

In devices, exciplexes are formed at the heterojunction. Morteani et al. [48] developed a model to explain the electronic processes at the heterojunction and suggested two mechanisms for electron-hole capture at a type II heterojunction (see Figure 2-10). The first possibility is the injection of one of the charges into the opposite polymer and the formation of an intramolecular exciton, the second possibility is the formation of an interfacial exciplex state via a barrier-free electron capture. Then the exciplex can diffuse on one of the polymer and recombine or either recombines at the interface and emits a photon. This fast barrier free capture could explain the high-efficiency observed in some devices [48].

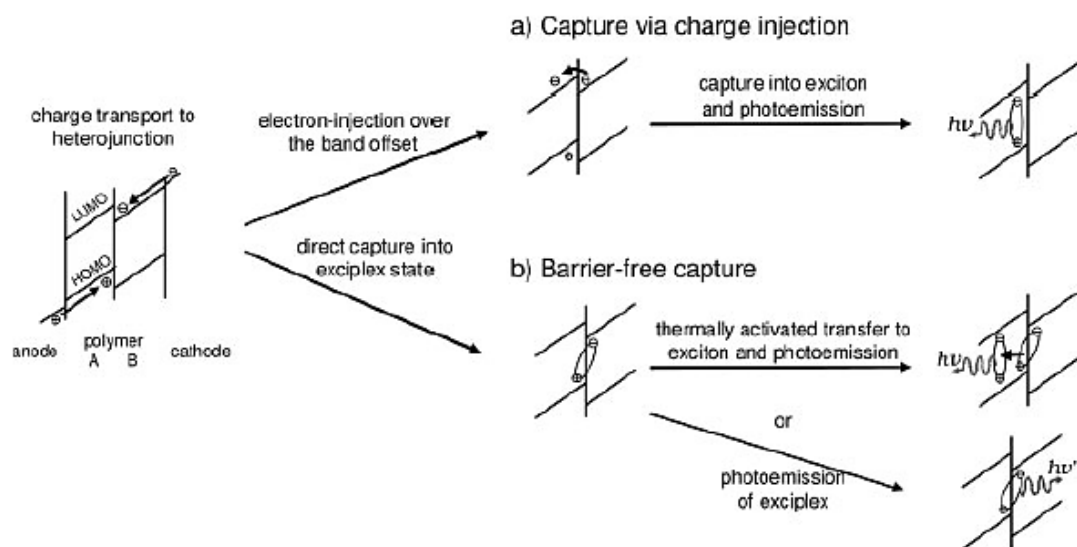


Figure 2-10 Illustration of the two mechanisms for electron-hole capture. Electrons and holes are transported through their respective transport materials and accumulate at the heterojunction. a) Injection of one of the charges into the opposite polymer enables charge capture within the polymer bulk and formation of intramolecular excitons. b) Barrier-free electron-hole capture directly produces a neutral excited-state, the exciplex, without prior injection of a charge carrier into the opposite polymer. The exciplex can either be thermally activated and transferred to the bulk exciton, leading to exciton electroluminescence or, with small oscillator strength, it can also decay radiatively and emit red-shifted exciplex electroluminescence. Reprinted with permission from [48]. Copyright 2006 Wiley-VCH Verlag GmbH & Co. KGaA.

A polaron pair or “spatially indirect exciton” [49-52] is a Coulomb pair of two oppositely charged polarons located on adjacent chains (charge separation). They are similar to π -dimers except that the binding is mainly coulombic whereas for dimers the binding is due to lattice relaxation [53]. It is often described as a step between separated polarons and exciton [54, 55]. Polaron pairs are distinguished from excimers and exciplexes by the fact that they represent single quasi particles with coherent wavefunctions [47, 56].

2.8.2 Interactions in both ground states and excited states: aggregation (dimer)

While exciplexes, excimers and polaron pairs exist only in the excited state, interchain interactions such as aggregates may lead to ground-state interactions [42, 47,

57]. Aggregates are usually formed from a forced proximity of two (in this case it is called a dimer) or more molecules and the wavefunctions of both the ground and excited states are delocalized over multiple chains. The aggregate is, therefore, directly accessible spectroscopically and is characterized by a broad, featureless and red-shifted emission. The origin of the red shift is due to the fact that the delocalization of the excited-state wave function upon aggregate formation lowers the energy relative to the single-chain exciton. Furthermore, the small overlap between the delocalized excited state with the single-chain ground-state wave function leads to a small Franck Condon factor and hence a long radiative lifetime and low luminescence quantum efficiency [42, 51, 58-62].

2.9 Efficiencies and CIE coordinates

To convert the light output from photons to photometric units, such as candela and lumen, the spectral profile needs to be measured. Once the spectral shape is known, the overlap integral with the luminosity function can be calculated.

Indeed, most applications of organic light-emitting diodes are related to visible light emission (e.g. illumination, signs and displays). That is the reason why the optical characteristics of OLEDs are usually given and compared in photometric units (not radiometric). Photometry is essentially radiometry normalised to the spectral response of the eye. The spectral response of the human eye under daylight conditions (photoptic response) was standardized by the Commission Internationale de l'Éclairage (CIE) in 1924.

The sensitivity of the human eye depends on the wavelength of the light. Indeed, the retina contains two sorts of sensors: the rods, responsible for the luminance, and the cones, measuring the colour. Three types of cones form what is called a tristimulus measuring system which is based on the three primary colours: blue, green and red/orange. In 1931 the Commission Internationale de l'Éclairage created the first mathematically defined colour spaces called CIE XYZ [63].

In the XYZ system Y is the brightness, Z is quasi-equal to blue simulation and X is quasi-equal to red simulation. The colour matching functions $\bar{x}(\lambda)$, $\bar{y}(\lambda)$, $\bar{z}(\lambda)$ can be assimilated to weight factors. The colours are obtained by mixing the three standard primaries:

$$\mathbf{C} = \bar{x}(\lambda) \mathbf{X} + \bar{y}(\lambda) \mathbf{Y} + \bar{z}(\lambda) \mathbf{Z} \quad (2.1)$$

generally written

$$\mathbf{C} = \mathbf{X}\mathbf{X} + \mathbf{Y}\mathbf{Y} + \mathbf{Z}\mathbf{Z} \quad (2.2)$$

If $I(\lambda)$ is the spectral power distribution, the three coordinates XYZ are given by:

$$X = \int_0^{\infty} I(\lambda) \bar{x}(\lambda) d\lambda \quad (2.3)$$

$$Y = \int_0^{\infty} I(\lambda) \bar{y}(\lambda) d\lambda \quad (2.4)$$

$$Z = \int_0^{\infty} I(\lambda) \bar{z}(\lambda) d\lambda \quad (2.5)$$

where λ is the wavelength of the equivalent chromatic light in nanometres.

The chromaticity of a colour is specified by the two derived parameters x and y .

$$x = \frac{X}{X + Y + Z} \quad (2.6)$$

$$y = \frac{Y}{X + Y + Z} \quad (2.7)$$

x and y can then be placed on the CIE 1931 colour space chromaticity diagram (see Figure 2-11).

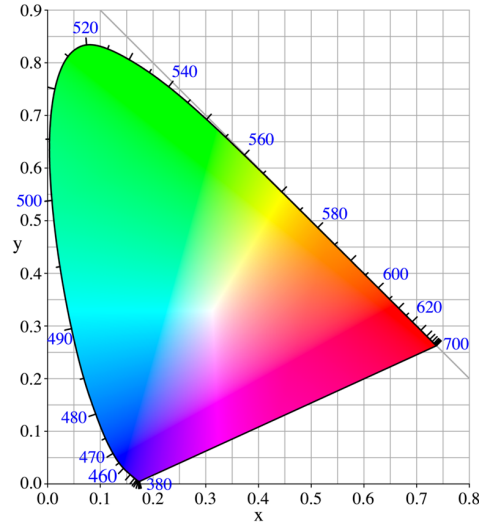


Figure 2-11 CIE 1931 colour space chromaticity diagram. Reprinted from [64].

The efficiency of OLEDs is mainly characterized by three values:

- The most commonly used value is the external quantum efficiency EQE or η_{ext} (in %) defined as the ratio between the number of emitted photons and the number of injected electrons. It can also be described as the product of the internal quantum efficiency η_{int} (number of photons emitted inside the OLED divided by the number of electrons injected) times the out-coupling efficiency χ

$$\eta_{ext} = \chi\eta_{int} \quad (2.8)$$

where the internal quantum efficiency is dependent on the device architecture and the material properties of the OLED:

$$\eta_{int} = \gamma\beta\eta_{PL} \quad (2.9)$$

with γ the number of excitons formed per injected unitary charge, β the number of emissive excitons over the total number of generated excitons, η_{PL} the photoluminescence quantum efficiency defined as the ratio between the number of radiative transitions and the number of total transitions from the excited state to the ground state in a given material.

The elementary processes for charge recombination, production of excitons, internal and external light emission in an OLED are shown in Figure 2-12.

Figure 2-12 Elementary processes for charge recombination, production of excitons, internal and external light emission in an OLED.

- The current efficiency η_c (in cd/A) is defined by the ratio of the luminance (luminous intensity per unit area) and the current density J flowing through the OLED.

$$\eta_c = \frac{\text{Luminance (cd/m}^2\text{)}}{J \text{ (A/m}^2\text{)}} = \frac{\text{Intensity (Cd/A)}}{\text{Current}} \quad (2.10)$$

- The luminous efficiency η_{lum} (in lm/W) gives the ratio of total light output in lumens to the electrical power in Watts.

$$\eta_{lum} = \frac{\phi_L}{V \cdot I} (\text{lumen/W}) \propto \frac{\eta_c}{V} \quad (2.11)$$

with ϕ_L the luminous flux, V the operating voltage and I the current.

The quantum efficiency is a radiometric value, whereas the current and the luminous efficiencies are photometric values. As a consequence the same quantum efficiency for a red, green and blue emitting OLED gives strongly different current and luminous efficiencies, due to a different luminous efficacy of radiation (quotient of the luminous flux by the corresponding radiant flux) of the three LEDs.

From these equations we can devise different strategies for increasing the quantum efficiency:

1 - Increasing the number of excitons formed by enhancing the electron/hole balance. This can be achieved by improving the charge injection with hole and electron-injecting/transporting layers and by improving the charge transport with new high mobility materials.

2 - Increasing the number of radiative excitons by increasing the number of singlet excitons and by converting triplet excitons into radiative species.

3 - Suppressing non-radiative decay channels by preventing aggregation quenching, reducing electrode quenching and contaminations.

In the present thesis several of these strategies were used: the incorporation of hole and electron-transporting layers and the use of phosphorescent copper-based complexes.

3 Experimental techniques

The present chapter describes the experimental methods used to characterise the materials and the devices depicted in the present thesis. This includes the photophysical, electrical and electrochemical techniques. The electrochemical measurements reported here were carried out in the chemistry department of University College London (UCL) with the help of Daren J. Caruana.

3.1 UV-Vis spectroscopy

UV-Vis spectroscopy is a molecular absorption spectroscopy. When atoms or molecules absorb a photon in the visible or ultraviolet radiation, the electrons are promoted from their ground state to an excited state. The type of excitation depends on the wavelength of the light. Electrons are promoted to higher orbitals by ultraviolet or visible light, pure vibrations are excited by infrared light, and pure rotations by microwaves [65].

A spectrometer is an instrument which measures the reflection or absorbance (transmittance) characteristics of a sample [66]. The spectrometer used at UCL is an Agilent 8453 and allows the measurement of the transmittance of the light between 190 and 1100 nm.

In the molecular system, UV-Vis spectroscopy deals with electronic transitions. Every electronic transition is characterized by the excitation of an electron from one energy level to a higher energy level. All the electronic transitions involved are: $\sigma \rightarrow \sigma^*$, $\pi \rightarrow \sigma^*$, $n \rightarrow \sigma^*$, $n \rightarrow \pi^*$, $\pi \rightarrow \pi^*$ as shown in Figure 3-1.

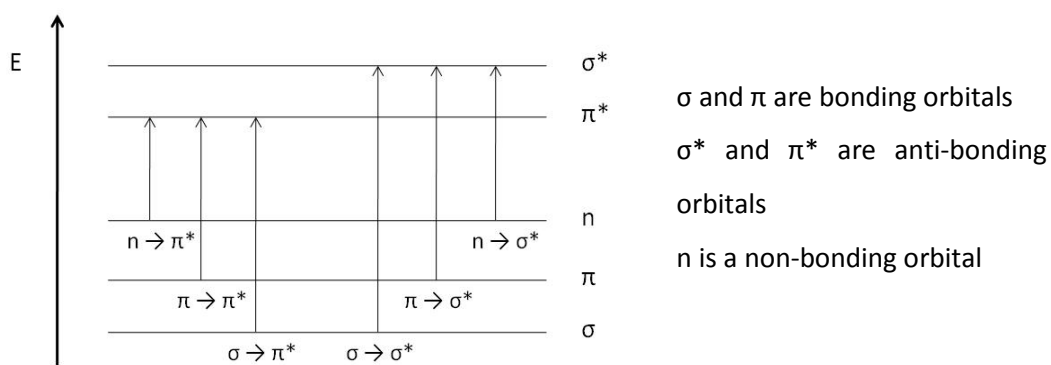


Figure 3-1 Possible electronic transitions in UV-Vis spectroscopy

The absorption spectrum is the absorption of light as a function of wavelength. The spectrum of an atom or molecule depends on its energy level structure, therefore, absorption spectra are useful for the identification of compounds. The interesting parameters are the absorption maxima, the shoulders and the intensity of the measured absorption. Measuring the concentration of an absorbing species in a sample is accomplished by applying the Beer-Lambert law [65].

It is important to always take into account the effect of the solvent because it has an influence on the intensity and the position of the band depending on whether it is polar or apolar. Indeed, polar solvents are capable of contracting the hydrogen bond and of associating with the compounds.

A UV-Vis spectrometer is constituted by the following elements:

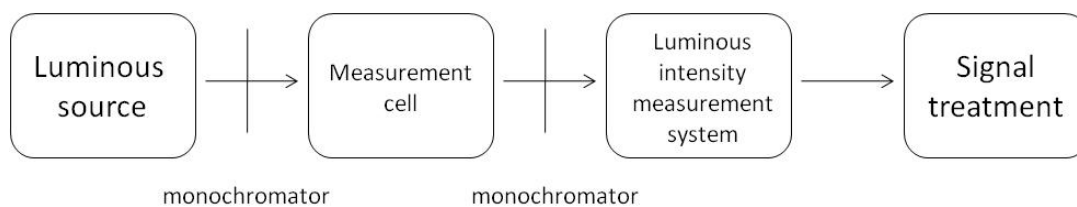


Figure 3-2 Scheme of a UV-Vis spectrometer

3.2 Photoluminescence measurements

Photoluminescence (PL) measurements are a non-destructive characterisation of materials in solution or solid-state. It consists of exciting a sample with a laser. If the energy of the photons are greater than the energy gap of the semiconducting material the sample emits photons. They are then collected and the response spectrum is measured.

The measurements were carried out at room temperature in air with a helium-cadmium laser at 325 nm or a topgan laser diode at 412 nm exciting the samples. The spectra were recorded with an ANDOR Shamrock spectrograph coupled with an ANDOR Newton CCD unit cooled at -50°C.

3.3 Time-correlated single photon counting (TCSPC)

To measure the lifetime of an excited state, time-resolved techniques such as time-correlated single photon counting (TCSPC) are commonly used. In single photon counting techniques photons are detected and counted in order to measure the luminescence decay of a sample. The system is calibrated so that less than one photon per pulse is detected [67]. The decay profile is determined by measuring the time between the excitation of the sample by the laser and the detection of a photon by the photomultiplier numerous times.

In simple cases, the luminescence decay curve is then deconvoluted and its monoexponential fit gives the lifetime value τ , as shown in the following equation:

$$I(t) = I_0 e^{\frac{-t}{\tau}} \quad (3.1)$$

Sometimes multiexponential decays are observed, showing the presence of different populations i.e. the existence of more than one emitting species. In such cases, the intensity decay is approximated as the sum of individual decays as shown in the following equation:

$$I(t) = \sum_{i=1}^n \alpha_i e^{-\frac{t}{\tau_i}} \quad (3.2)$$

With α_i the amplitude of the components and n the number of decays.

Time-resolved measurements were performed using a ps-pulsed diode laser (Edinburgh Instrument EPL-375), emitting at 371 nm, as the excitation source and entering from the polymer/material side. The instrument response function with the laser mentioned above was 270 ps wide (FWHM, Full Width at Half Maximum). The set that includes sample chamber, monochromator, photomultiplier tube and counter card was a commercially bought turn-key system (Edinburgh Instruments F-900).

3.4 IVL measurements

The setup for measuring electrical characteristics and light output of the light-emitting diodes contained a vacuum chamber for the sample so that all characteristics were measured under rough vacuum. The sample holder was connected to an electrical switch (pixel selector) which was connected to a sourcemeter (Keithley 2400). The sample itself was turned with the ITO towards a window, and a Si-photodiode was placed outside to measure the light coming out of the sample. The signal from the photodiode was connected to a preamplifier and subsequently detected by a multimeter (Keithley 2000). No integrating sphere was needed considering that, as it was the case in our sample configuration, we have a Lambertian emission from a flat surface. Taking into account the photodiode-sample distance and the size of the active surface of the photodiode a prefactor was calculated.

The electroluminescence spectra were measured in the same way using an ANDOR Shamrock spectrograph coupled with an ANDOR Newton CCD unit cooled at -50°C.

In the present work, when the values are reported, the luminance was taken for currents no larger than 4 mA (114 mA/cm²), since the electrodes are prone to sparking above this current. For near-infrared devices, the light turn-on voltage was defined as the voltage at which the measured light output reached 0.2 mW/m² above the background.

3.5 Thickness measurements

The thicknesses of the films were determined using a Dektak profilometer. After a scratch was made on the film surface of the sample, the stylus of the Dektak scanned the sample and the thickness of the film was determined by measuring the height difference between the film and the ITO revealed by the scratch.

3.6 Atomic Force Microscopy (AFM)

The Atomic Force Microscopy (AFM) is a very high resolution type of scanning probe microscopy (SPM) whose principle relies on the measure of the mechanical interactions between the extremity of a tip and the surface of a sample. It was invented by Binnig, Quate and Gerber in 1986 [68] and its success is due to its versatility: it is possible to scan in air, in liquid media or under a control atmosphere and almost any kind of surface can be used, including conductive and not-conductive samples. It can be used for imaging and measuring surfaces but for atomic manipulation as well.

The surface of the sample is scanned by a sharp tip placed at the end of a cantilever, typically made of silicon or silicon nitride. This miniature probe is brought close to the surface to analyse, and it is the interaction forces between the cantilever and the sample that are the working basics of an AFM. It relies on the fact that the amount of force between the probe and the sample is dependent on the spring constant (stiffness) of the cantilever and the distance between the cantilever and the surface of the sample. Piezoelectronic scanners together with a feedback loop control the motion of the probe

across the surface. The deflection of the probe is measured by the deviation of a laser beam reflected on the extremity of the cantilever.

The AFM can be operated in different mode, such as contact, tapping and non-contact, depending on the application.

The contact mode is a static mode in which the cantilever is “dragged” across the surface of the sample and the imaging of the surface is directly made from the deflection of the cantilever. In constant force mode the height above the surface is maintained constant by constantly adjusting the deflection of the cantilever.

In tapping mode, the cantilever is oscillated at a value close to its resonant frequency, for which the amplitude of oscillation is typically 20 to 100 nm, by a small piezoelectric element mounted in the AFM tip holder. The interactions of forces acting on the cantilever decrease the amplitude of its oscillation when it gets closer to the sample. The feedback loop then adjusts the height of the cantilever to maintain the oscillation amplitude constant and an image of the surface is obtained.

In non-contact mode the tip does not touch the sample surface. The oscillations of the cantilever are set slightly above its resonant frequency (amplitude of about 10 nm). The Van der Waals forces, which are dominant at this scale, cause the frequency or oscillation amplitude of the cantilever to shift from its original value. The feedback loop maintains the frequency or oscillation amplitude constant by adjusting the tip to the sample distance, and by plotting these distances one can construct an image of the sample surface. This mode is generally used for soft samples and minimizes the degradation of the sample and/or the tip [69, 70].

The measurements depicted in chapter 7 were done at the London Centre for Nanotechnology on a Bruker Dimension 3100 in air using tapping mode.

3.7 HOMO, LUMO determination via cyclic voltammetry

The knowledge of HOMO and LUMO energy levels is of tremendous importance for the design of an OLED and the understanding of its behaviour. Their energy is influenced by the chemical structure of the molecule, the electronic polarization of its surroundings

and its conjugation length in the case of polymers [71]. Two different classes of techniques can be used: the spectroscopic (Ultraviolet Photoelectron Spectroscopy and Inverse PhotoEmission Spectroscopy) or voltammetric methods.

Ultraviolet Photoelectron Spectroscopy (UPS) allows the direct determination of the ionization energy (E_i) whereas Inverse PhotoEmission Spectroscopy (IPES) allows a direct measurement of the electronic affinity ($\mathcal{A}e$) of a molecule on the surface of a thin film. Cyclic voltammetry leads to the measurement of the oxidation or reduction potential of a molecule which are indirectly linked to E_{HOMO} or E_{LUMO} , respectively.

E_{HOMO} and E_{LUMO} are, therefore, ideally determined via UPS and IPES respectively, however, the high cost and the complexity of these systems (ultra-high vacuum is required for example) leads many laboratories to use cyclic voltammetry.

3.7.1 Background on voltammetric techniques

In any voltammetric technique, a potential function is applied to the working electrode which is dipped in a solution containing electro-active compounds. The response of the electrochemical cell is measured by recording the current flow. Usually, the electrochemist is interested in the corresponding current-potential curve called voltammogram.

The different types of voltammetric techniques result from the diversity of potential excitation functions that can be applied to the working electrode as well as from the various ways to record and plot currents [72].

In potential sweep methods the potential of the working electrode (measured against the reference electrode of choice) is varied continuously according to a predetermined potential waveform (also called the excitation function), while the current (or some current function) is measured as a function of the potential [72].

3.7.1.1 Cyclic Voltammetry

Cyclic voltammetry is a very versatile electrochemical technique [73] for the characterization of electroactive species. The current response over a range of

potentials is measured, starting at an initial value and varying the potential in a linear manner up to a limiting value. At this limiting potential the direction of the potential scan is reversed and the same potential range is scanned in the opposite direction. Consequently, the species formed by oxidation on the forward scan can be reduced on the reverse scan [73].

The voltammogram is the plot of the current response function of the voltage as seen in Figure 3-3.

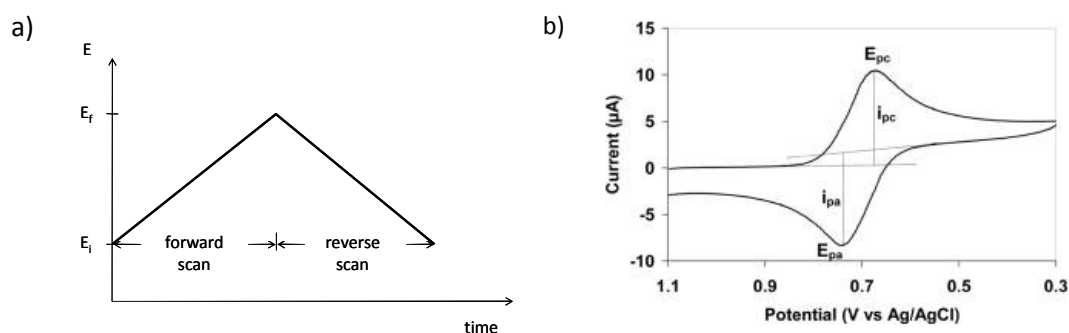


Figure 3-3. a) typical excitation function for cyclic voltammetry. Reprinted with permission from [72]. Copyright 1999 Wiley-VCH Verlag GmbH & Co. KGaA. and b) cyclic voltammogram. Reprinted with permission from [74]. Copyright 2000, Springer.

The characteristics of the voltammogram recorded depend on a number of factors including: the rate of the electron transfer reaction, the chemical reactivity of the electroactive species and the voltage scan rate.

The scan begins from the left hand side of the current/voltage plot where no current flows. As the voltage is swept further to the right a current begins to flow and eventually reaches a pick before dropping. The current is called faradic and results from electron transfer processes across the electrode-solution interface. The current depends on the square root of the scan rate [72].

The key advantage of cyclic voltammetry results from the reverse scan. The method provides valuable information regarding the stability of the oxidation states and the rate of electron transfer between the electrode and the analyte. Figure 3-3 shows a typical voltammogram of a reversible oxidoreduction: the electrochemical process is fast in the time scale of the experiment and the electrogenerated species are perfectly stable in

the electrolytic solution. Under these conditions and assuming that the solution is kept unstirred during the experiment, the ratio of the cathodic and anodic peak currents should be equal to one. Deviations from unity reveal the presence of chemical reactions involving either redox partner or both partners [72]. The average of the two peak potentials affords the half wave potential for the corresponding couple, that is:

$$E_{1/2} = (E_{pc} + E_{pa})/2. \quad (3.3)$$

The reversibility of a redox couple is verified by $n\Delta E = 59$ mV with ΔE the difference between E_{pc} and E_{pa} and n the number of electrons transferred in the overall reaction.

The solvent, the electrolyte and the electrodes have to be carefully chosen in order to avoid reactions with the sample or their degradations in the condition of the experiment since the accuracy of the measurement could be biased.

For more precision additional methods can be used to complement cyclic voltammetry such as Differential Pulse Voltammetry (DPV) and Sweep Wave Voltammetry (SWV). For more information see [72, 75].

3.7.1.2 Ferrocene, an internal standard

In aqueous solutions universally accepted reference electrodes such as the normal hydrogen electrode (NHE) or the saturated calomel electrode (SCE) exist and facilitate the measurement of the redox potentials. But electrochemical measurements in water are not always possible due to the insolubility or instability of the compound. Unfortunately, no universal reference electrode exists for nonaqueous solvents.

A good candidate as an internal standard demands a perfect reversible behaviour in a wide variety of solvents. The reproducibility of potential measurements is the key advantage of the ferrocene referencing system [76], this is why in 1984 the IUPAC Commission on Electrochemistry recommended the ferricenium/ferrocene couple as an intersolvental standard at any temperature [77].

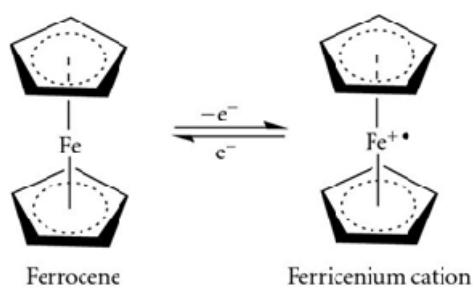


Figure 3-4 The ferrocene/ferricenium redox couple. Reprinted with permission from [78]. Copyright 2008 American Chemical Society.

Ferrocene is a very stable 18-electron system which undergoes a fast one-electron oxidation to yield the cationic ferricenium species at very accessible potentials (Figure 3-4). Its oxidized form is stable in most organic solvents with limitation in aqueous media especially in basic conditions [72].

3.7.2 Experimental procedure

The experiments were carried out using 0.05 M tetrabutylammonium hexafluorophosphate in acetonitrile as an electrolyte, gold as working electrode, Ag/AgCl wire as reference electrode and Pt as counter electrode.

The polymer (in toluene, p-xylene or chlorobenzene) was drop-cast on the working electrode and then inserted in the electrolyte. After the identification of the electrochemical behaviour of the compound, ferrocene was added to the cell with, ideally, the exclusion of air and water [77]. The electrochemical experiment was repeated, and the position of the waves could be directly compared to the potential of the ferricenium/ferrocene (Fc^+/Fc) couple. Sometimes the Fc^+/Fc couple is inappropriate due to overlapping waves. In these cases other compounds can be substituted such as decamethylferrocene. Potentials can, still, be related to Fc^+/Fc through a second experiment in which the potential difference between the ferricenium/ferrocene couple and the substituted couple is measured [76].

3.7.3 HOMO-LUMO calculations

Forrest et al. [79] have determined the relationship between the E_{HOMO} measured by UPS and the oxidation potential of molecular organic semiconductor. They compared the HOMO values of several molecules measured from UPS and their oxidation potentials measured via cyclic voltammetry and explained the results by a combination of solvation and image charge effects.

The relation is:

$$E_{\text{HOMO}} = -(1.4 \pm 0.1) \times (qV_{\text{CV}}) - (4.6 \pm 0.08) \text{ eV} \quad (3.4)$$

V_{CV} is the difference between the potentials at which the reference solute and samples are oxidized and q is the electron charge.

Then, in 2009, Forrest et al. [80] published a similar work on the LUMO determination where they compared IPES, electrochemical reduction potentials, optical bandgap and density functional theory (DFT) calculations methods. They concluded that the four approaches were valid if used appropriately.

When the reduction potential was available, the relation determined by Forrest et al. [80] was used:

$$E_{\text{LUMO}} = -(1.19 \pm 0.08) \times E_{\text{red}} - (4.78 \pm 0.17) \text{ eV} \quad (3.5)$$

with E_{red} the potential of the sample versus ferrocene.

However, due to the equipment and facilities available at UCL, the determination of the LUMO via optical bandgap calculations was used in most cases.

Actually the difference between the HOMO and LUMO level is called transport bandgap (E_{t}). However, since E_{t} is not easily accessible, the LUMO energy is approximated as the HOMO energy plus the optical energy gap (E_{opt}). The difference between E_{t} and E_{opt} is the exciton binding energy and can be as much as 0.4 to 1.4 eV [81].

The optical bandgap is estimated from the lowest energy peak of the absorption spectra.

The results obtained on some polymers and small molecules often used in organic electronic devices are shown in part 3.7.4.

All approaches used for the determination of the HOMO and LUMO of organic molecules present advantages and drawbacks. Even the direct measurement from UPS and IPES are not straightforward and variations in the values reported in the literature are frequent [82]. As explained previously the method used in the present work implies many approximations, however, the values, still, give a good idea of the actual relative energy levels of the materials investigated.

3.7.4 HOMO-LUMO measurements of some classic polymers and small molecules used in organic electronics devices.

The HOMO-LUMO energy levels of several commercial polymers and small molecules are reported in the following table. The experimental conditions, measurements and calculations were carried out according to the previous explanations.

Table 3-1 HOMO-LUMO energy levels of commercial polymers and small molecules measured at UCL.

	E_{HOMO} (eV)	E_{LUMO} (eV)
F8	-6.08 ± 0.33	-2.86 ± 0.41
F8BT	-6.04 ± 0.32	-3.29 ± 0.38
P3HT	-5.73 ± 0.30	-3.65 ± 0.34
PC ₆₁ BM	-6.32 ± 0.34	-3.79 ± 0.39
PFB	-4.90 ± 0.24	-1.63 ± 0.33
TFB	-5.35 ± 0.27	-2.11 ± 0.36
MDMO-PPV	-5.66 ± 0.30	-3.13 ± 0.35
PVK	-5.46 ± 0.28	-1.84 ± 0.39
ADS077RE	-5.36 ± 0.27	-3.39 ± 0.30

Note that where the HOMO and LUMO values measured at UCL are reported in a figure, the boxes represent the errors and the reported value is in the middle of each box.

Note:

1. F8: ADS129BE, batch 07C030A
2. F8BT: ADS133YE, batch 10G041A
3. P3HT: Aldrich 698997, batch MKBC8213
4. PC₆₁BM: Aldrich 684430, batch MKBC1782
5. PFB: ADS232GE, batch 10J020A
6. TFB: ADS259BE, batch 10K020A
7. MDMO-PPV: Aldrich 546561, batch MKBC7547
8. PVK: Aldrich 182605, batch 02609HJ
9. ADS077RE, batch 09D050A

PART II.

Phosphorescent OLEDs

4 Triplet excitons, phosphorescence and Cu-complexes

A solution to achieve efficient OLEDs is energy and charge transfer from host molecules to emissive guest molecules. In particular, the use of phosphorescent emitters as guests allows an increase in the efficiency because they can harvest triplet excitons. Cu based complexes are of particular interest because they can provide cheap and non-toxic electroluminescent materials with short excited-state lifetimes, high emission quantum yields and appropriate HOMO/LUMO energies.

4.1 Theory behind the triplet exciton

An exciton is an electrostatically bound electron-hole pair. The hole, as the conceptual and mathematical opposite of an electron, has a spin (m_s) of $\frac{1}{2}$ or $-\frac{1}{2}$. As a result, according to quantum mechanics, the total spin S of these electron/hole pair or exciton can only take the values of $S = 0$ ($M_S = 0$) or $S = 1$ ($M_S = +1, -1, 0$), where M_S denotes the quantum number for the z-component of the total spin.

$$\begin{array}{lll}
 \langle \uparrow\downarrow \rangle - \langle \downarrow\uparrow \rangle & M_S=0 & S=0 \text{ singlet} \\
 \langle \uparrow\uparrow \rangle & M_S=1 & \left. \vphantom{\langle \uparrow\uparrow \rangle} \right\} S=1 \text{ triplet} \\
 \langle \downarrow\downarrow \rangle & M_S=-1 & \\
 \langle \uparrow\downarrow \rangle + \langle \downarrow\uparrow \rangle & M_S=0 &
 \end{array}$$

The $S = 0$ state is called singlet state (denoted by S_n , where n is the vibronic sub-level), in contrast, the $S = 1$ state is called triplet state (denoted by T_n). The symbols \uparrow and \downarrow represent the possible values of m_s of the electron and hole. If each state has the same formation probability, three triplets are formed for one singlet.

Normally, the triplet state is at a lower energy level than the corresponding singlet state because electronic repulsion is higher for spin-paired electrons [46, 83]. Typical

energy levels/states and energy-transfer processes are described in the following diagram (Figure 4-1):

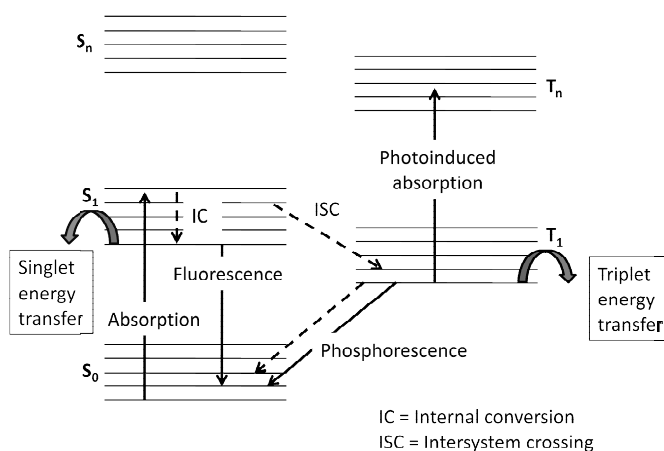


Figure 4-1 Simplified scheme of the electronic processes of organic molecules and oligomers. Plain arrows represent radiative decays and dashed arrows represent non-radiative decays. Reproduced with permission from [84].

In the phosphorescence mechanism the triplet excitons decay radiatively to the singlet ground state. These triplets were either directly created as triplets upon electron-hole recombination or they were initially singlet states that have undergone an intersystem crossing. Phosphorescence is very weak in purely organic compounds but becomes stronger when a heavy metal is incorporated because it allows the spin to flip. Indeed, in organic materials, most of the triplet states decay non-radiatively since they cannot spin-flip and, therefore, do not contribute to the light emission and limit the efficiency of the OLED.

Organometallic complexes are a very good choice as emissive species thanks to their strong spin-orbit coupling induced by the heavy atom they contain. This strong spin-orbit coupling leads to a very efficient intersystem crossing and thus to the formation of more triplet states and a higher phosphorescence rate ($T_1 \rightarrow S_0$). In the text, triplet emitters refer to these transition metal complexes.

Whereas for small molecule OLEDs the simple singlet:triplet ratio of 1:3 from the spin statistics seems to hold, this ratio seems to be possibly higher for polymer but is, still, under debate [85-88]. If we consider the spin statistics, a device, without triplet

emitters, has a maximal internal efficiency of 25 % and this value is up to 100 % for a device containing triplet emitters since they can harvest both singlet and triplet excitons and are, therefore, of tremendous importance for efficient OLEDs [89]. This rule does not apply if the recombination is not statistically controlled or if the excited state generated is not a pure singlet or triplet state [86].

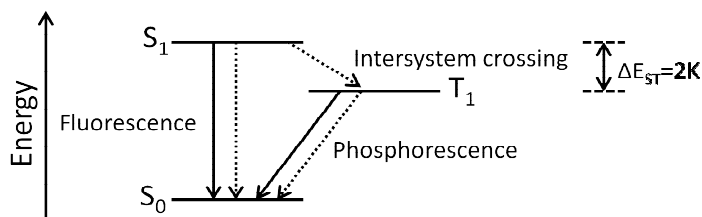


Figure 4-2 State diagram of singlet and triplet states. Solid lines represent radiative decay channels whereas dotted lines represent the non-radiative decay channels. Reproduced with permission from [90]. Copyright 2009, Elsevier.

The exchange energy (ΔE_{ST} , energy difference between singlet and triplet that are derived from the same electron orbital configuration, see Figure 4-2) is generally in the order of 0.7 to 1 eV and is precisely defined as twice the exchange integral K . It results from the interaction of the electron in the HOMO with that of the LUMO [91] and thus depends on the overlap of the electron and hole wave functions. The exchange energy of conjugated polymers is found to be almost constant and of 0.7 eV whereas the exchange energy of molecules depends on molecular size and can take a wide range of values [92].

ΔE_{ST} cannot be measured easily via absorption spectroscopy because the S_0 - T_1 transition occurs with a much lower rate than S_0 - S_1 transition. It is also not accurate to take the difference between the singlet absorption and the triplet emission as the former does not take into account the relaxation effect whereas the latter does. Therefore, the energy difference (ΔE_{ST}) between the singlet and triplet emission transitions at 77 K is generally taken as an estimation for the exchange energy [91].

In most cases organometallic guests are used within wide energy gap host materials. The non-radiative triplet from the host can be either Förster transferred to the singlet of the guest and then be converted into a triplet exciton by intersystem crossing or directly

transferred via Dexter mechanism to the triplet state of the guest (see Figure 4-3), resulting in high efficiency devices [93].

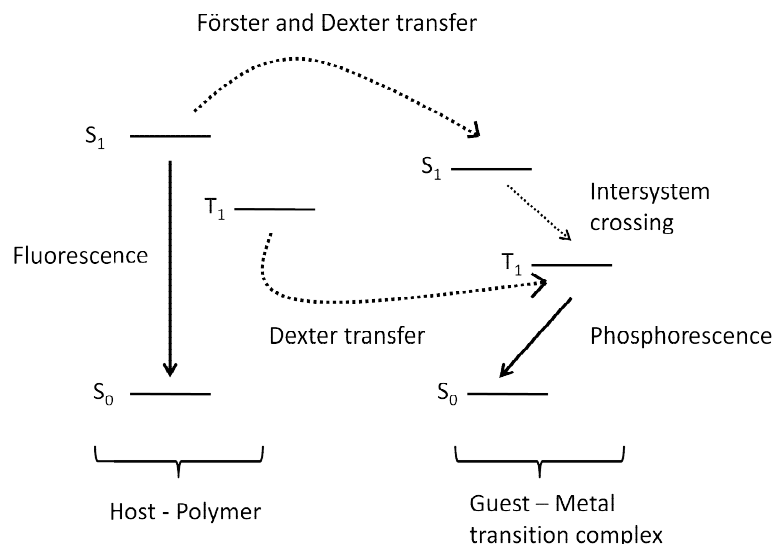


Figure 4-3 Schematic diagram of the fluorescent and phosphorescent transitions for host-guest systems. Adapted with permission from [94]. © 2002 IEEE.

Triplet excitons present long lifetimes, typically in the microsecond to the millisecond range [95] causing triplet-triplet annihilation ($T_1 + T_1 \rightarrow S_0 + S_1$) and concentration quenching and thus affecting the efficiency of the OLEDs [96]. Those are the reasons why the chemists from WWUM focused on organometallic compounds and tried to reduce their exciton lifetimes below the microsecond range.

4.2 *Cu-complexes and their applications in OLEDs*

4.2.1 *Theoretical background on transition metal complexes*

Copper is a transition metal that presents the electronic structure $[Ar]3d^{10}4s^1$. A transition metal is a d element which forms one or more stable ions which have incompletely filled d orbitals. In free transition metal atoms or ions the d orbitals are degenerated, it means that they all have the same energy.

A transition metal complex has a transition metal ion at its centre with a number of other molecules or ions surrounding it. These can be considered to be attached to the

central ion by co-ordinate (dative covalent) bonds. The molecules or ions surrounding the central metal ion are called ligands. The d orbitals are interacting with the electron cloud of the ligands resulting in a splitting of the d orbitals into different energy levels. This non-degenerate energy configuration depends on the geometry of the complex.

Crystal field theory is used to predict the energies and the distribution of the d orbitals and is briefly explained in part 4.2.1.2.

4.2.1.1 Transition metal complexes

In emissive metal complexes, the electron density in each of the frontier molecular orbitals is preferentially located at the metal or the ligand and is not equally delocalized between metal and ancillary ligands. The electronic transition can be considered as one-electron excitation that occurs among the associated frontier orbitals [97].

Different types of transitions depending on the nature of the electronically excited state can be listed:

- Metal-centered (MC) excited state (dd state) originate from electron hopping between the nonbonding (d_n) and the antibonding (d_{σ^*}) orbitals of metal complexes presenting partially filled d shell.
- Metal-to-Ligand Charge-Transfer (MLCT) excited state ($d\pi^*$ state). MLCT state involves electronic transitions from a metal-based d orbital to a ligand-based delocalized π^* antibonding orbitals [98]. Since the π^* ligand orbital is usually delocalized over the acceptor ligand, its population by MLCT excitation causes minimum structural distortions enabling efficient radiative decay with lifetimes ranging from ten nanoseconds to the microsecond.
- Ligand centered (LC) $\pi\pi^*$ or $n\pi^*$ excited states arise from electronic transitions between a π -bonding or a n-bonding orbital to a higher energy anti-bonding orbital that are mainly localized on the ligand chromophore.
- Ligand-to-Metal Charge-Transfer (LMCT) excited states (πd state). They are generated by electronic transitions from a π orbital, localised on a ligand, to a metal orbital. LMCT luminescence generally comes from complexes with high oxidation states metal atoms.

The relative order of these electronic transitions can be changed depending on the metal centre, the ligands or the geometry of the complex [99].

4.2.1.2 d^{10} transition metal complexes and the tetrahedral coordination

Crystal field theory is based on an ionic description of metal-ligand bonding. It provides a model for understanding the electronic structure, optical properties and magnetic properties of coordination complexes. The theory treats the complex as a central metal ion perturbed by the approach of negatively charged ligands [100].

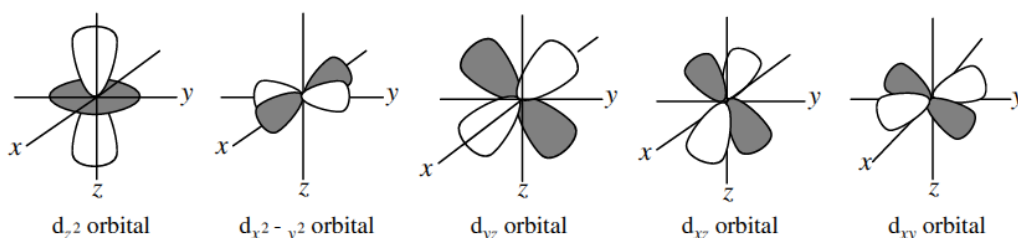


Figure 4-4 Scheme of the five d orbitals, reprinted with permission from [101]. Copyright 2004 Wiley and Sons.

By comparing Figure 4-4 and Figure 4-5 one can see that in tetrahedral complexes three of the d orbitals point almost towards the ligand and the other two points between the ligands. It is important to note that no d orbital points directly at the ligands. Repulsion between the ligand electrons and electrons in the three d orbitals that almost point at the ligands destabilizes them resulting in the formation of two energy levels of d orbitals e and t_2 . Indeed, although neither orbital points directly towards the ligands, an electron in d_{xy} will be closer to the ligands and so will be more repelled than those in $d_{x^2-y^2}$. Similarly, electrons in d_{xz} and d_{yz} are more repelled than in d_z^2 . Hence for a tetrahedral complex, the d_{xy} , d_{xz} and d_{yz} orbitals are higher in energy than $d_{x^2-y^2}$ and d_z^2 . The orbital energy level diagram for a tetrahedral complex is shown in Figure 4-5. t_2 orbitals are destabilized orbitals formed by d_{xy} , d_{yz} and d_{xz} and e orbitals are stabilized orbitals formed by d_z^2 and $d_{x^2-y^2}$. Δ_t is the energy gap.

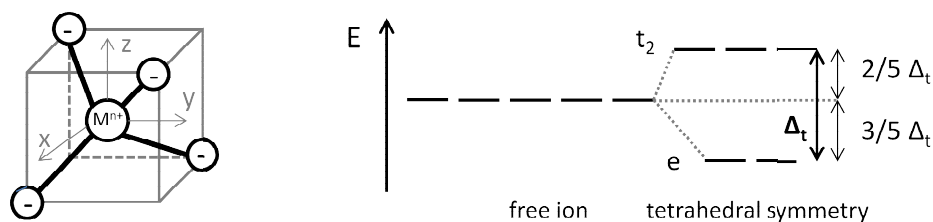


Figure 4-5 Scheme of the tetrahedral complex geometry (on the right) and scheme of the tetrahedral configuration (on the left).

Ligands arrangements in a tetrahedral geometry minimize inter-ligand repulsions. This configuration is usually preferred by d^0 and d^{10} metals. In particular, in a d^{10} metal centre the electronic charge presents a symmetric delocalization. Electronic absorption of light in these compounds is associated with $^1\text{MLCT}$ transitions from filled d orbitals to the empty π^* orbital of the ligand or with ^1LC from the π orbital to the π^* orbital of the ligand. Since d-d transitions are impossible ^1MC transitions are not observed.

4.2.1.3 The particular case of Cu-complexes

In its elementary form, copper has a filled d orbital (d^{10}) and only one electron in its 3s orbital. This electron is easily given and forms a +I oxidation state. Since its valence band is completely filled, copper in its first oxidation state has a symmetric localization of the electronic charge which leads the ligands to favour a tetrahedral configuration around the metal centre.

The photophysics of copper complexes is mainly dominated by charge transfer and intraligand transition. This is due to its d^{10} configuration that prevents the stabilisation of its excited states via the ligand field [99]. Emission from copper(I) complexes tends to be weak and short-lived and its phosphorescence emission wavelength span over the visible spectrum.

4.2.2 Literature review on Copper complexes based OLED

Literature on triplet materials is abundant but literature on the specific topic of copper based transition complexes is much more limited.

The first reported devices made with Cu(I)-complexes are based on tetranuclear copper complexes with a measured quantum yield of 0.42 in solution. The devices made with the structure ITO/Cu₄:PVK/TAZⁱ(4.5 nm)/Al exhibited a brightness of 50 cd.m⁻² at a current density of 20 mA.cm⁻², an EL efficiency of 0.1 % and a turn-on voltage of 12 V [102]. Tremendous progress have been made since this first article and Qisheng Zhang et al. published three articles [103-105] on the subject. The first two articles focused on green Cu^I phenanthroline complexes they used in OLEDs and LECs (Light-Emitting Electrochemical Cells). Using ITO/PEDOT:PSS/Cu^I:PVK/CBP/Alq₃/LiF/Al structures, they achieved current efficiencies up to 10.5 cd.A⁻¹ at 105 cd.m⁻², a maximum brightness of 1663 cd.m⁻² but turn-on voltages of 13 to 15 V and observed a red-shift of the EL spectra with increasing voltage due to the distortion of the molecules under strong electric field. They obtained a current efficiency of 56 cd.A⁻¹, an EQE of 16 % and a turn-on voltage of 2.9 V with electrochemical cells but faced problems of stability. In the last article they used more rigid phenanthroline complexes which exhibit red emission. Best results were achieved with thermal evaporated structures ITO/PEDOT:PSS/TCCz:Cu^I/TPBi/LiF/Al with 4.9 % EQE, current efficiency of 3.8 cd.A⁻¹ at 10 mA.cm⁻² and a turn-on voltage of 11 V. The same compound was tested in a PVK matrix and with BCP and Alq₃ as interlayers and they obtained 0.9 % EQE, 0.6 cd.A⁻¹ at 10 mA.cm⁻² and a turn-on voltage of 11 V. Finally, low turn-on voltages and high efficiencies were achieved by Guangbo Che et al. [106]. Their devices exhibited turn-on voltages of 4 V, a maximum current efficiencies of 11.3 cd.A⁻¹ and a maximum brightness of 2322 cd.m⁻² using an entire small molecules design ITO/2-TNATA (10 nm)/NPB (40 nm)/CBP:Cu-complex (30 nm)/TPBi (40 nm)/LiF/Al. More recently, the group of C. Adachi [107] achieved 15 % EQE and low turn-on voltage (5.6 V) green OLEDs by using efficient exciton confinement with the

ⁱ TAZ is an electron-transporting triazole derivative. For the meaning of the abbreviation of the compounds, please see section "List of abbreviations, mathematical symbols and compounds" at the end of the thesis.

structure ITO/PEDOT:PSS (40 nm)/[[Cu(dnbp)(DPEPhos)]BF₄:PYD2 (30 nm)/DPEPO (50 nm)/LiF (0.7 nm)/Al (100 nm).

4.3 How to choose a good host?

When phosphorescent compounds such as copper-complexes are used they need to be dispersed in a matrix called host. In the absence of this host the phosphorescent compounds would aggregate and triplet-triplet annihilation (spin-allowed process leading to one singlet excited state and a singlet ground state) would occur. The host can participate to the emission as well, ideally by transferring its excitons to the guest.

It is not always easy to find a good host for a phosphorescent guest and some rules have to be followed in order to fabricate efficient phosphorescent OLEDs:

To avoid the energy transfer of the triplet excitons from the guest to the host, the energy levels of the host should be chosen so that the exciton triplet energy of the host is higher than that of the guest [46, 90, 91, 108]. The exchange energy of the host material should thus be as small as possible to allow for both efficient charge injection into the host and efficient triplet emission from the phosphorescent guest [91]. Furthermore, the HOMO/LUMO of the guest and the host should permit a good charge injection from the host to the guest. Finally a good overlap between the emission of the host and the absorption of the guest would ensure an efficient Förster transfer from the host to the guest.

Materials with large bandgaps are more likely to present high triplet energies but are also more likely to suffer from charge injection problems due to misalignment of the HOMO and/or LUMO level with the Fermi levels of the electrodes. HTL and ETL are then often used to ensure a good charge injection [89].

5 Study of the TFB/PVK/TPBi structure spin-coated from chlorobenzene

Since phosphorescent compounds need to be incorporated in a matrix to avoid aggregation and triplet-triplet annihilation, the choice of the host and the interlayers are of tremendous importance. The choice of the host was made previously by Claudia Bizzarri from the university of Münster during a visit at UCL. She tested four different hosts that she selected according their triplet energy levels and HOMO/LUMO energy levels: poly(9-vinylcarbazole) (PVK), poly(9,9'-dioctylfluorene-co-bis-N,N'-(4-butylphenyl)-bis-(N,N'-phenyl-1,4-phenylene-diamine) (PFB); 4,4'-dicarbazolyl-1,1'-biphenyl (CBP) and 4,4',4''-tris(N-carbazolyl)triphenylamine (TCTA). TCTA being insoluble in chlorobenzene was ruled out and tests were performed on PVK, PFB and CBP. However, in the case of CBP and PFB, a large part of the emission was coming from the host and not from the copper complex. PVK was thus selected as a host for the fabrication of the phosphorescent OLEDs.

In this chapter, the matrix (PVK) and the interlayers that are used with the copper complexes in chapter 6 are presented. The photophysical properties of the materials and their performance in devices are also introduced.

5.1 Materials properties

5.1.1 PVK

A well-known polymer that exhibits a high triplet energy is poly(9-vinylcarbazole) (PVK) [91]. It consists of a non-conjugated main chain with carbazole units attached as side groups (see Figure 5-1). The carbazole groups confer the electrical and electroluminescence properties to the polymer [109]. Many carbazole derivatives have a sufficiently high triplet energy to be able to host triplet emitters, which can be explained by the fact that they present $n-\pi^*$ transition. It means that the optical transition involves

orbitals that have a different orientation in space and thus the wavefunction overlap in the exchange integral is small [90]. PVK is also widely used because of its excellent film forming properties, relatively good hole-transporting properties and its large energy gap [71].

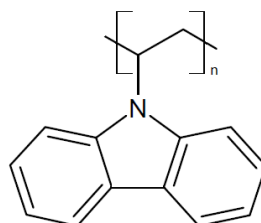


Figure 5-1 Chemical structure of PVK.

As mentioned before materials with high triplet energy often suffer from energy misalignment. Indeed, PVK has a LUMO level at about 1.8 eV (see part 3.7.4). The barrier for injection of electrons from Ca (work function: 2.9 eV) to PVK is then large and can result in devices with low luminance and high turn-on voltages [89]. Furthermore, PVK is a poor electron-transporter. Thus, to enhance the charge carrier balance in the devices an electron-transporter [71] need to be added by either mixing it with PVK or evaporating it on top of the PVK layer.

The electroluminescent spectrum (EL spectrum, see Figure 5-3) of PVK presents two major peaks that can be attributed to different molecular conformation of PVK [110, 111]. The main luminescent emission of PVK comes from trap states caused by two adjacent flat carbazole unit stackings relative to one another [112]. A lower energy trap state (430 nm) is formed when both benzene rings on adjacent carbazole groups overlap (face-to-face structure) (Figure 5-2. a)). A second higher energy trap state (380 nm) results from a partially eclipsed conformation that involves only one eclipsed aromatic benzene ring from each carbazole group (side by side conformation) (Figure 5-2. b)). In addition, an emission peak at about 590 nm is commonly observed.

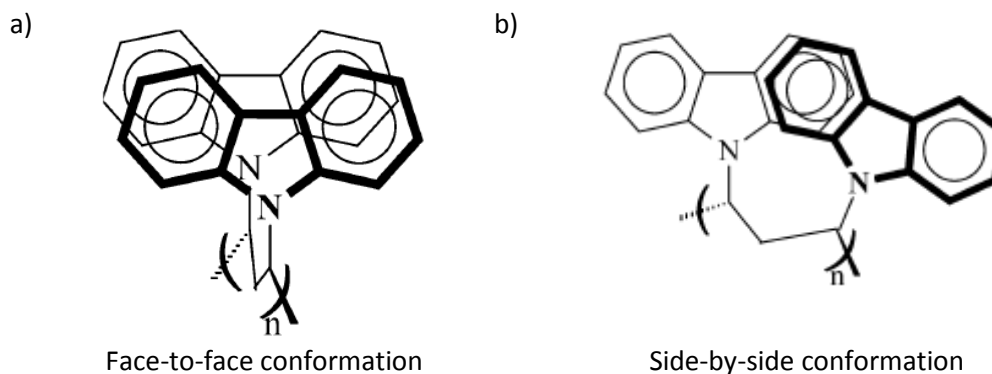


Figure 5-2 Representation of a) face-to-face conformation and b) side-by-side conformation of PVK. Reproduced with permission from [113]. Copyright 2006 American Chemical Society.

As seen in Figure 5-3, the spectra overlap between the absorption and the PL spectra is small, therefore, self-absorption should not have significant effect on the EL spectrum.

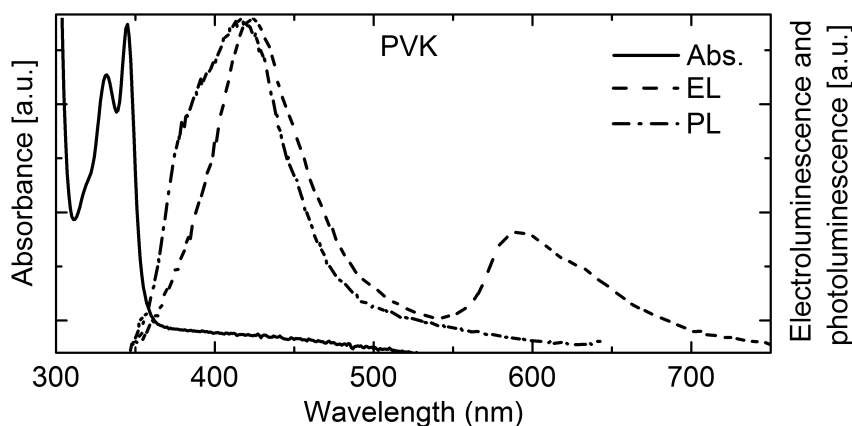


Figure 5-3 Absorption, electroluminescence and photoluminescence spectra of PVK. PL and absorption spectra are from a thin film of 1 wt.% PVK in chlorobenzene. The EL spectra is from a ITO/PEDOT:PSS/PVK/Ca/Al device.

Glowacki et al. [71] already reported the 10 nm shift between the EL and the PL spectra that is observed in Figure 5-3. Since the peak formed between 590 and 610 nm was also observed in PL measurements at 80 K the authors associated these bands to the triplet excimers [111, 114]. However, the presence of triplet phosphorescence was excluded by others [115] since they did not observe this peak in the PL spectrum [116, 117] and triplet phosphorescence had been previously reported around 500 nm [118, 119]. Monkman et al. concluded that the peak arises from impurities or chemical

reaction products [120]. The photophysical properties of PVK are summarized in Table 5-1.

Table 5-1 Summary of the photophysical data of PVK.

Absorption	Photoluminescence	Electroluminescence	Lifetime (430 nm, 200 ns)
296 nm 332 nm 345 nm	416 nm	425 nm 590 nm	$\tau_1: 0.67 \pm 0.04$ ns (18.2%) $\tau_2: 22.7 \pm 0.5$ ns (81.8%)

The differences between EL and PL spectra depicted in Figure 5-3 are due to the fact that for PL spectra the polymer is photo-excited whereas it is electro-excited in the case of EL spectra. The exciton formation in PL spectra can only result from energy transfer since no free carriers are generated by photo-excitation whereas in EL spectra both energy transfer and charge carrier trapping can be responsible [121].

The molecular conformation of PVK can be changed by using different solvent or different molecular weights of PVK [111]. Indeed, as the molecular weight increases a red-shift in the EL spectra of PVK is observed. This is due to more stacked carbazole groups on the same backbone leading to weaker interactions between carbazole groups on neighbouring molecules. Furthermore, the triplet exciton formation depends on molecular conformation as well as film morphology. The probability of triplet formation in conjugated polymers increases with decreasing conjugation length [122-124]. In the case of PVK conjugation length can be associated to side-by-side conformation, therefore, face-to-face conformation facilitates the triplet exciton formation. Furthermore, since the degree of face-to-face conformation increases as the molecular weight increases, PVK with high molecular weight is more suitable as a host for phosphorescent compounds [111].

The lifetime decays of PVK was measured via time correlated single photon counting spectroscopy (see part 3.3 and Table 5-1) and a biexponential decay with lifetimes similar to those in the literature was found [110, 125, 126]. The fast decay of 0.67 ns is attributed to the fully eclipsed configuration whereas the slow one of 22.7 ns is attributed to the partially eclipsed configuration [125].

Finally the HOMO and LUMO of PVK were measured as well (see part 3.7) and the results (HOMO at 5.4 eV and LUMO at 1.8 eV) are in agreement with the literature [117, 126-130]. The triplet energy level of PVK was usually reported to be around 2.5 eV [111, 131, 132]. However, Monkman et al. [120] reported it at 2.88 eV whereas 2.5 eV would be the energy of triplet dimer traps.

5.1.2 Incorporation of a hole-injecting layer: TFB

Poly[(9,9-dioctylfluorenyl-2,7-diyl)-alt-(4,4'-(N-(p-butylphenyl))diphenylamine)] (TFB), depicted in Figure 5-4, is a polymer that can be spin-coated to form an interlayer between the PEDOT:PSS layer and the active layer. After the deposition of TFB, devices were annealed at 180°C for an hour in order to form an insoluble thin layer of TFB. The insertion of a TFB interlayer is believed to prevent the exciton quenching at the PEDOT:PSS interface [133] and, therefore, improve the device efficiency [23]. It also acts as an electron-blocking layer in some cases.

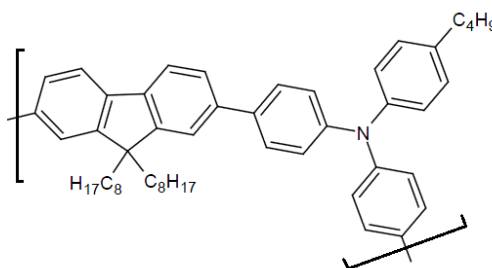


Figure 5-4 Chemical structure of TFB.

Redecker et al. [134] reported that the hole transport in TFB is nondispersive, and that its room temperature mobility is as high as $0.01 \text{ cm}^2 \text{ V}^{-1} \text{ s}^{-1}$ [135]. TFB is widely used in devices but few publications report its photophysical behaviour.

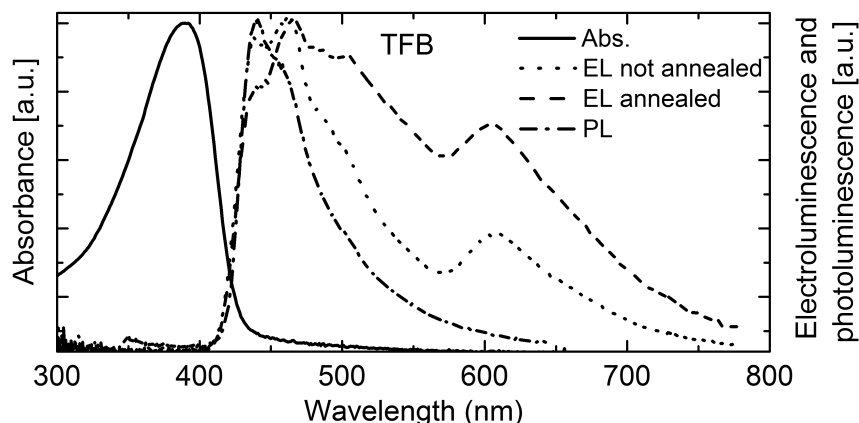


Figure 5-5 Absorption, electroluminescence (for not annealed and annealed devices) and photoluminescence spectra of pure TFB from a thin film of 2 wt. % in p-xylene.

Table 5-2 Summary of the photophysical data of TFB.

Absorption	Photoluminescence	Electroluminescence	Lifetime (435 nm, 20/50 ns)
390nm	440 nm	440 nm 465 nm 605 nm	$\tau_1: 0.162 \pm 0.002$ ns (82.6%) $\tau_2: 1.11 \pm 0.06$ ns (17.4%)

The data reported in Figure 5-5 Table 5-2 are comparable to the literature on TFB and similar to the data given from American Dye Source (ADS), who supplied the materials. We found a maximum absorption wavelength of 390 nm that ADS reported at 382 nm (THF). For the photoluminescence ADS gives a peak wavelength at 440 nm (THF), which we confirmed, and was reported at 435 nm [136] and 450 nm [137] in the literature. The EL spectrum is shown for non-annealed and annealed devices. The two first peaks are pointing at 440 nm and 465 nm with a second peak at 605 nm whereas Tsami et al. [138] reported 435 and 460 nm. The EL spectrum of the annealed devices is wider than the one of the non-annealed devices shifting the colour from blue to white. Finally the phosphorescence lifetime decay was too fast for the instrumentation of Clark et al. [137] and a double decay of 0.162 and 1.11 ns was measured at UCL. It should be noted that the first lifetime of 0.162 ns was actually below the laser pulse width of 300 ps and hence subject to a large uncertainty.

The HOMO-LUMO values measured at UCL (see part 3.7.4) of -5.35 eV and -2.11 eV are in agreement with the literature [124, 138-141] and its triplet energy was reported as 2.2-2.3 eV [142].

5.1.3 Incorporation of an electron-injecting layer: TPBi

Since carbazole derivatives are hole transporting polymers, their devices suffer from unbalanced charge carriers. To overcome this problem an electron-transporting layer can be evaporated on top of the PVK layer. TPBi then acts as an electron-injecting and transporting layer and eases the injection of the electrons from the cathode to PVK. Another solution would be to blend an electron-transporting compound directly with PVK [91].

In our case 1,3,5-tris(phenyl-2-benzimidazole)-benzene (TPBi, see Figure 5-6) was chosen and could be thermally evaporated on top of the active layer [105, 106, 143, 144].

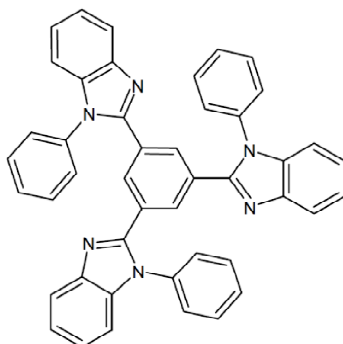


Figure 5-6 Chemical structure of TPBi.

Like TFB, TPBi is widely used in OLEDs devices but very little information on its photophysical behaviour was reported. The absorption and photoluminescence spectra of TPBi measured at UCL with the help of Marten Tolk are depicted in Figure 5-7.

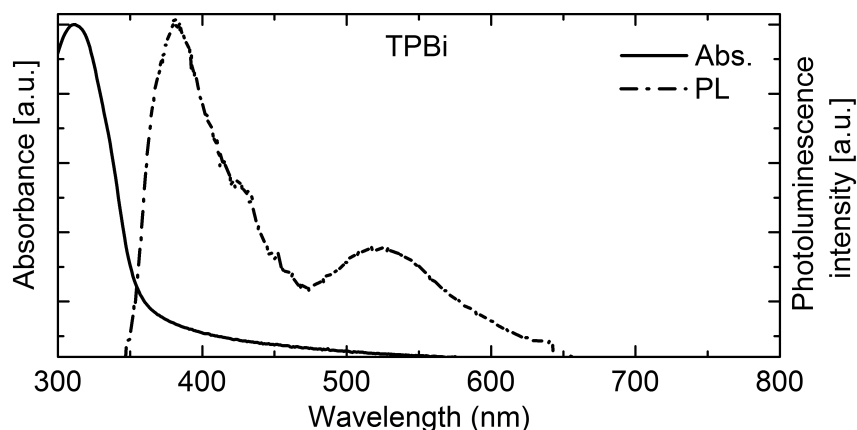


Figure 5-7 Absorption and PL spectra of pure TPBi from 30 nm thin-film (sublimed)

The maximum absorption wavelength of TPBi was measured at 311 nm (Lumtec, provider of this material reported it at 305 nm in THF). The main peak on the PL spectrum is at 382 nm which is in agreement with the literature [111] but we observed a second peak at 522 nm which is not reported. Finally the photoluminescence decay was found to be a biexponential decay of 0.24 and 5.1 ns.

Table 5-3 Summary of the photophysical data of TPBi.

Absorption	Photoluminescence	Lifetime (520/545 nm, 20 ns)
311 nm	382 nm ~ 522 nm	τ_1 : 0.24 ± 0.02 ns (45%) τ_2 : 5.1 ± 0.6 ns (55%)

It was not possible to measure the HOMO-LUMO energy levels of TPBi at UCL, thus, they are assumed to be at -6.7 and -2.7 eV respectively [145]. Its HOMO indicates that it is a very efficient hole-blocking layer. Its large energy gap means that it is a very good exciton blocking layer that should avoid exciton migration and formation occurring too close to the cathode. Its triplet energy level was reported at 2.6 eV [146].

5.2 Single and multilayer device properties

To study the behaviour of these three materials when used together in devices, their photophysical properties and devices characteristics were investigated.

5.2.1 PVK

The photophysical characteristics of PVK were already investigated in part 5.1.1. Devices with the architecture ITO/PEDOT:PSS/PVK/Ca/Al were prepared with a solution of 1 wt. % PVK in chlorobenzene deposited by spin-coating.

Since PVK is a good hole transporter and a bad electron transporter, devices made with PVK only show low efficiencies and low luminance that might be due to luminescence quenching by the electrodes (see Figure 5-8).

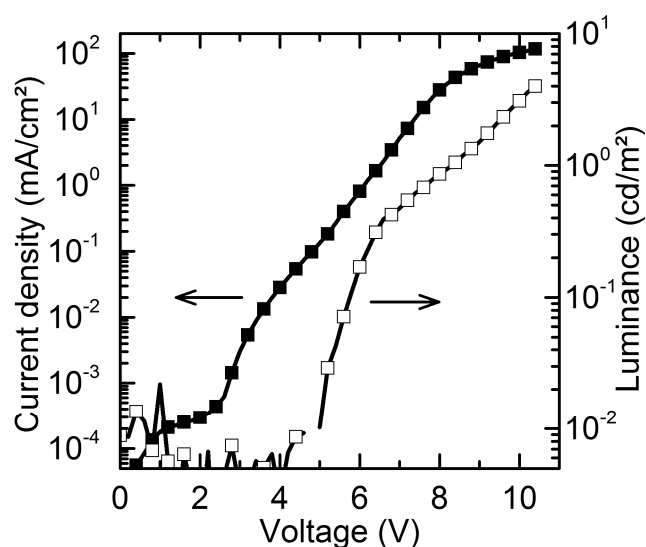


Figure 5-8 Current density (filled squares) and luminance (empty squares) function of the voltage for a ITO/PEDOT:PSS/PVK/Ca/Al device, thin film spun from PVK 1 wt.% in CB.

As presented in Table 5-4 the devices exhibited a violet light and had a turn-on-voltage of 6.2 V, an EQE of 0.02 % and a maximum luminance of 2.1 cd.m⁻².

Table 5-4 Summary of the properties of the ITO/PEDOT:PSS/PVK/Ca/Al devices in average.

	Max EQE (%)	Light turn on voltage (V)	Efficiency (@10 mA.cm ⁻²) (cd.A ⁻¹)	Max luminance (@114 mA.cm ⁻²) (cd.m ⁻²)	CIE coordinates
PVK	0.02 ± 0.02	6.2 ± 0.9	0.007 ± 0.008	2.1 ± 1.2	(0.28, 0.18)

PVK 1 wt. % in chlorobenzene.

5.2.2 TFB/PVK

The addition of a TFB interlayer was studied. TFB was spin-coated from a 2 wt. % p-xylene solution, annealed at 180°C for 1 hour prior to being spin rinsed with p-xylene. PVK was subsequently spin-coated on top of it.

After the spin rinsing step, the thickness of the TFB film was reduced from 100 nm to around 15 nm. Since such small thicknesses are difficult to measure with the profilometer the absorption of the different layers was measured and is displayed in Figure 5-9.

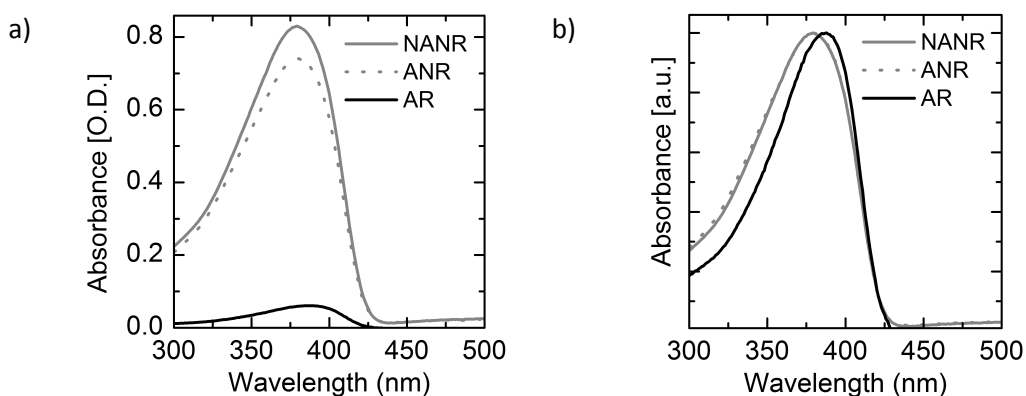


Figure 5-9 Absorption comparison between NANR (Not Annealed Not Rinsed), ANR (Annealed Not Rinsed) and AR (Annealed and Rinsed) samples of TFB (thin film of 2 wt.% in p-xylene) a) as measured and b) normalised.

As we can see there was a difference of 82.4 % in the absorbance values between the not rinsed not annealed and rinsed and annealed samples. This corresponds to a final thickness of 17.6 nm for the annealed and rinse sample which is in accordance with our first measurement and the literature [23, 147].

Besides we observed a red shift of 10 nm and a narrowing of the peak when the sample was annealed and rinsed which is probably due to an increased crystallinity of TFB.

The photophysical characteristics of TFB/PVK are shown in Figure 5-10 and Table 5-5.

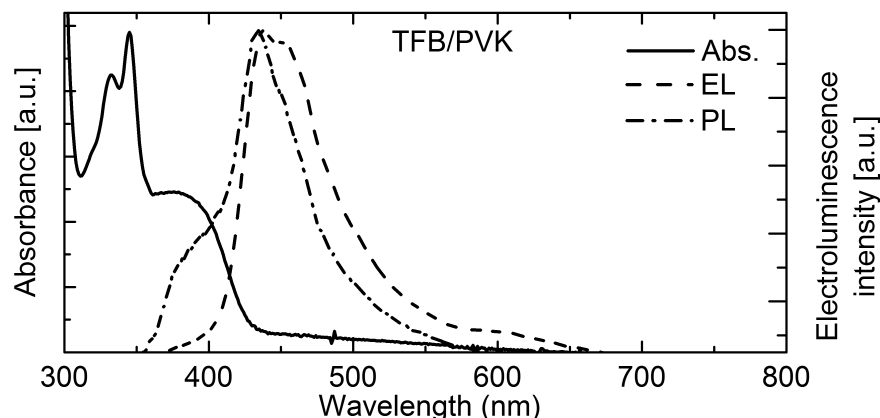


Figure 5-10 Absorption, PL and EL spectra of TFB/PVK samples. EL spectra of a ITO/PEDOT:PSS/TFB/PVK/Ca/Al device. All films were spun from a 2 wt. % TFB solution in p-xylene and a 1 wt. % PVK solution in chlorobenzene.

As we can see the double layer TFB/PVK might suffer from self-absorption since TFB absorbs where PVK emits. This might favour a Förster energy transfer from PVK to TFB and reabsorption via trivial energy transfer.

To compare the data, the absorption, PL and EL spectra of pure TFB and PVK are plotted together with the one of TFB/PVK in Figure 5-11.

The absorption and the PL spectra of the bilayer TFB/PVK are the superposition of the absorption and PL spectra of TFB and PVK indicating that no ground state interactions [120] are taking place. The first peak of the EL spectrum situated between 400 and 500 nm might also be the joint contribution of PVK and TFB. This result suggests that the recombination zone is situated at the interface between PVK and TFB and/or that an efficient Förster energy transfer from PVK to TFB is taking place and/or reabsorption via trivial energy transfer.

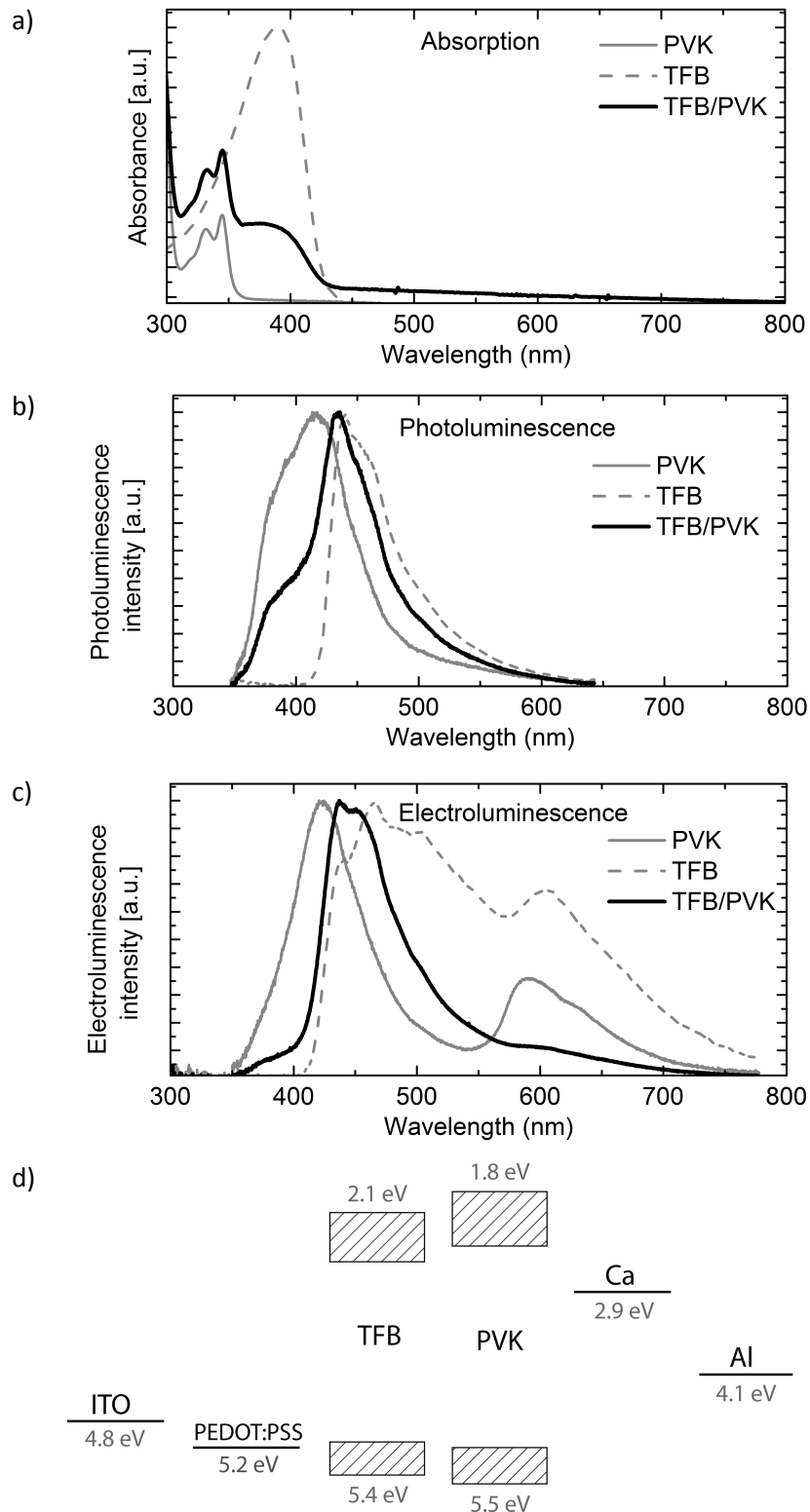


Figure 5-11 Comparison of a) the absorption b) the PL and c) the EL spectra of TFB, PVK and TFB/PVK in thin films and d) energy level of TFB and PVK compared to the work function of ITO, PEDOT:PSS, calcium and aluminum. The HOMO and LUMO levels of TFB and PVK were determined by cyclic voltammetry at UCL as described in the text and in part 3.7.4. Other values are from literature [148].

The HOMO-LUMO levels indicate that TFB might improve the injection of holes in the devices but cannot act as an electron blocking layer since its LUMO is lower than the one of PVK.

Table 5-5 Summary of the photophysical data of TFB/PVK.

Absorption	Photoluminescence	Electroluminescence	Lifetime (435 nm, 50 ns)
~384 nm 345 nm	434 nm	437 nm	τ_1 : 0.257 ± 0.001 ns (75.9%) τ_2 : 1.1 ns (19.5%) τ_3 : 22.7 ns (4.6%)

The photoluminescence decay of TFB/PVK showed a triple exponential decay with lifetimes of 0.26, 1.1 and 22.7 ns (see Table 5-5). The decay at 1.1 ns is characteristic of TFB whereas the one at 22.7 ns is characteristic of PVK. PVK and TFB both present a faster decay that might be reflected by the 0.26 ns component. There is thus no sign of the formation of an exciplex between TFB and PVK.

The current-voltage-light characteristics of the devices with the architecture ITO/PEDOT:PSS/TFB/PVK/Ca/Al are shown in Figure 5-12.

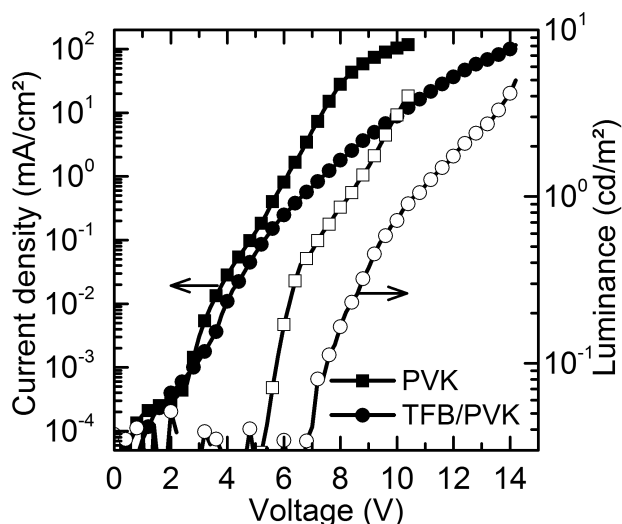


Figure 5-12 Current-voltage-light characteristics of a ITO/PEDOT:PSS/TFB/PVK/Ca/Al device (circles) compared to a ITO/PEDOT:PSS/PVK/Ca/Al device (squares). The current densities are represented by filled symbols and luminances by empty symbols.

Compared with pure PVK devices, the introduction of TFB does not improve the efficiency and the turn-on voltage but it increases the luminance and tunes the colour towards white.

Table 5-6 Summary of the properties of the ITO/PEDOT:PSS/TFB/PVK/Ca/Al devices in average compared to pure TFB (annealed devices) and pure PVK devices.

	Max EQE (%)	Light turn-on voltage (V)	Efficiency (@10 mA.cm ⁻²) (cd.A ⁻¹)	Max luminance (@114 mA.cm ⁻²) (cd.m ⁻²)	CIE coordinates
TFB	0.01 ± 0.00	5.3 ± 0.1	0.001 ± 0.000	13 ± 1.0	(0.28, 0.32)
PVK	0.02 ± 0.02	6.2 ± 0.9	0.007 ± 0.008	2.1 ± 1.2	(0.28, 0.18)
TFB/PVK	0.01 ± 0.01	7.1 ± 0.7	0.006 ± 0.003	4.9 ± 1.1	(0.19, 0.16)

TFB 2 wt. % p-xylene, PVK 1 wt. % in chlorobenzene

According to the HOMO/LUMO levels of PVK and TFB (Figure 5-11 d)) the injection of holes should be eased. However, the turn-on voltage increases with introduction of TFB, which might be due to charge trapping and/or the formation of a dipole at the organic/organic interface.

5.2.3 PVK/TPBi

In the following, the addition of 30 nm thick TPBi on top of PVK is investigated. The photophysical characteristics of PVK/TPBi are shown in Figure 5-13 and Table 5-7. The overlap between the absorption and emission spectra is small indicating that self-absorption could be neglected.

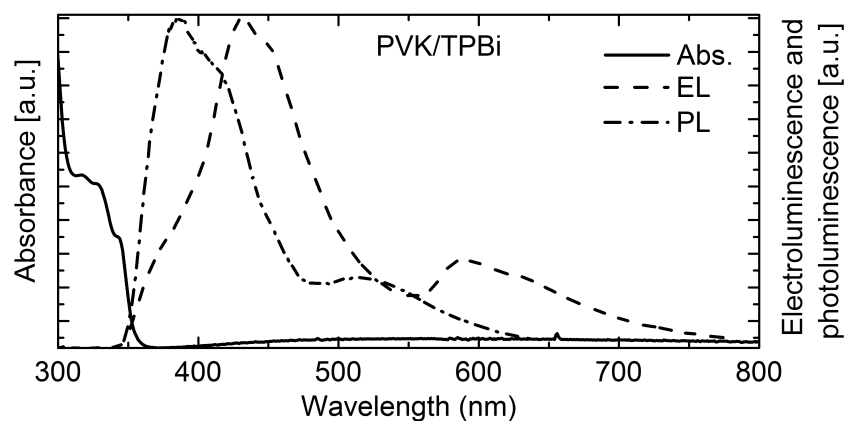


Figure 5-13 Absorption, photoluminescence and electroluminescence spectra of PVK/TPBi. All spectra are from a thin film of 1 wt. % PVK in chlorobenzene and 30 nm thick evaporated layer of TPBi. The EL spectrum is from a ITO/PEDOT:PSS/PVK/TPBi/Ca/Al device.

The comparison with pure PVK and pure TPBi is depicted in Figure 5-14. Once again the absorption and PL spectra of PVK/TPBi seem to be the superposition of the single compounds. Besides, one can see a shoulder around 380 nm and a broadening of the first EL emission peak compared to PVK. The emission at 380 nm could be due to a bit of emission from TPBi due to charge trapping at the TPBi/PVK interface. The second peak at 590 nm is attributed to PVK.

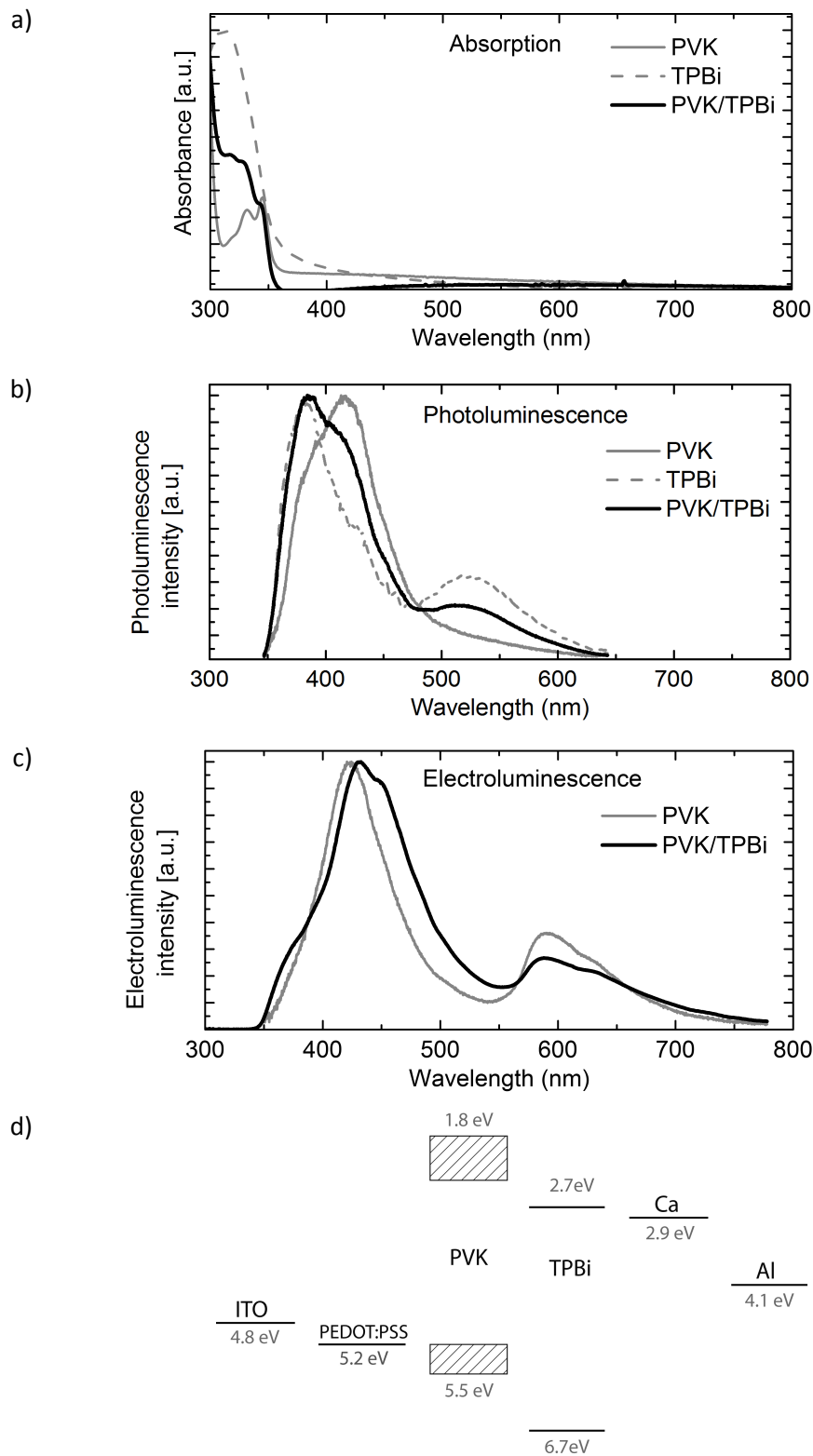


Figure 5-14 Comparison of a) the absorption b) the PL and c) the EL spectra of PVK, TPBi and PVK/TPBi in thin films and d) energy level of PVK and TPBi compared to the work function of ITO, PEDOT:PSS, calcium and aluminum. The EL of TPBi is not shown since no data are available. The HOMO and LUMO levels of PVK were determined by cyclic voltammetry at UCL as described in the text and in part 3.7.4. Other values are from literature [145, 148].

Photoluminescence decay measurements were also carried out on PVK/TPBi layers on spectroasil. At a wavelength of 430 nm a triple exponential decay was observed with lifetimes of 0.67, 3.55 and 22.7 ns. The long decay is characteristics of PVK, the medium one can be attributed to TPBi whereas the short one might be the short decays of both PVK and TPBi.

Table 5-7 Summary of the photophysical data of PVK/TPBi.

Absorption	Photoluminescence	Electroluminescence	Lifetime (430 nm, 200 ns)
~342 nm	386 nm ~521 nm	432 nm 590 nm	<u>430 nm, 200 ns</u> τ_1 : 0.67 ns (14.8%) τ_2 : 3.55 ns \pm 0.16 (20.8%) τ_3 : 22.7 (64.4%)

The IVL curves of the ITO/PEDOT:PSS/PVK/TPBi/Ca/Al devices are presented in Figure 5-15.

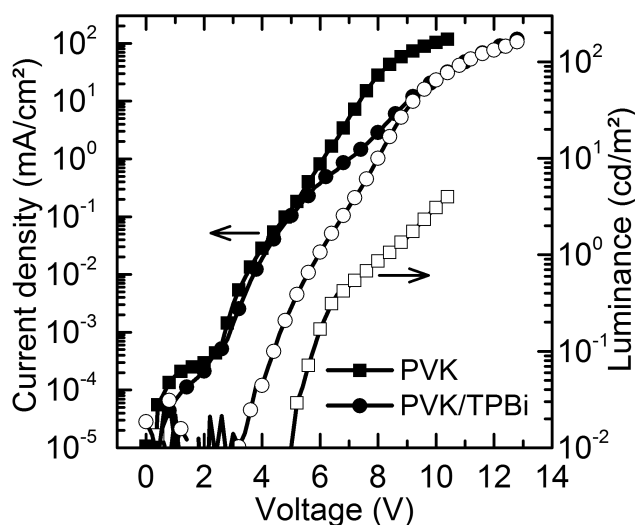


Figure 5-15 Current-voltage-light characteristics of a ITO/PEDOT:PSS/PVK/TPBi/Ca/Al device (circles) compared with pure PVK devices (squares). The current densities are represented by filled symbols and luminances by empty symbols.

The introduction of a TPBi layer on top of PVK dramatically increased the external quantum efficiency of the devices from 0.02 to 0.27 % and decreased the turn-on voltages from 6.2 V to 4.7 V (see Table 5-8 and Figure 5-15). This is due to a better charge carrier balance and injection in the devices and an emission zone further away

from the cathode thanks to an effective electron injection, electron transport and exciton blocking by TPBi.

Table 5-8 Summary of the properties of the ITO/PEDOT:PSS/PVK/TPBi/Ca/Al devices in average compared to pure PVK devices.

	Max EQE (%)	Light turn on voltage (V)	Efficiency (@10 mA.cm ⁻²) (cd.A ⁻¹)	Max luminance (@114 mA.cm ⁻²) (cd.m ⁻²)	CIE coordinates
PVK	0.02 ± 0.02	6.2 ± 0.9	0.007 ± 0.008	2.1 ± 1.2	(0.28, 0.18)
PVK/TPBi	0.27 ± 0.12	4.7 ± 1.7	0.24 ± 0.09	107 ± 106	(0.24, 0.17)

PVK 1 wt. % in chlorobenzene, 30 nm sublimed TPBi

5.2.4 TFB/PVK/TPBi

Finally the photophysical characteristics of TFB/PVK/TPBi were studied and are reported in Figure 5-16 and Table 5-9.

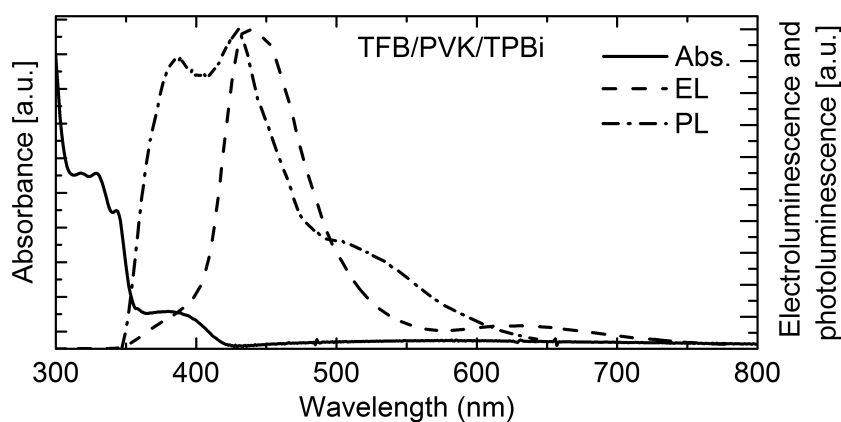


Figure 5-16 Absorption, photoluminescence and electroluminescence spectra of TFB/PVK/TPBi. All spectra are from a thin film of 2 wt. % TFB in p-xylene, 1 wt. % PVK in chlorobenzene and 30 nm thick evaporated layer of TPBi. The EL spectrum is from a ITO/PEDOT:PSS/TFB/PVK/TPBi/Ca/Al device.

The comparison with the pure materials is shown in Figure 5-17. Once again the absorption and PL spectra of TFB/PVK/TPBi seem to be the superposition of the single compounds.

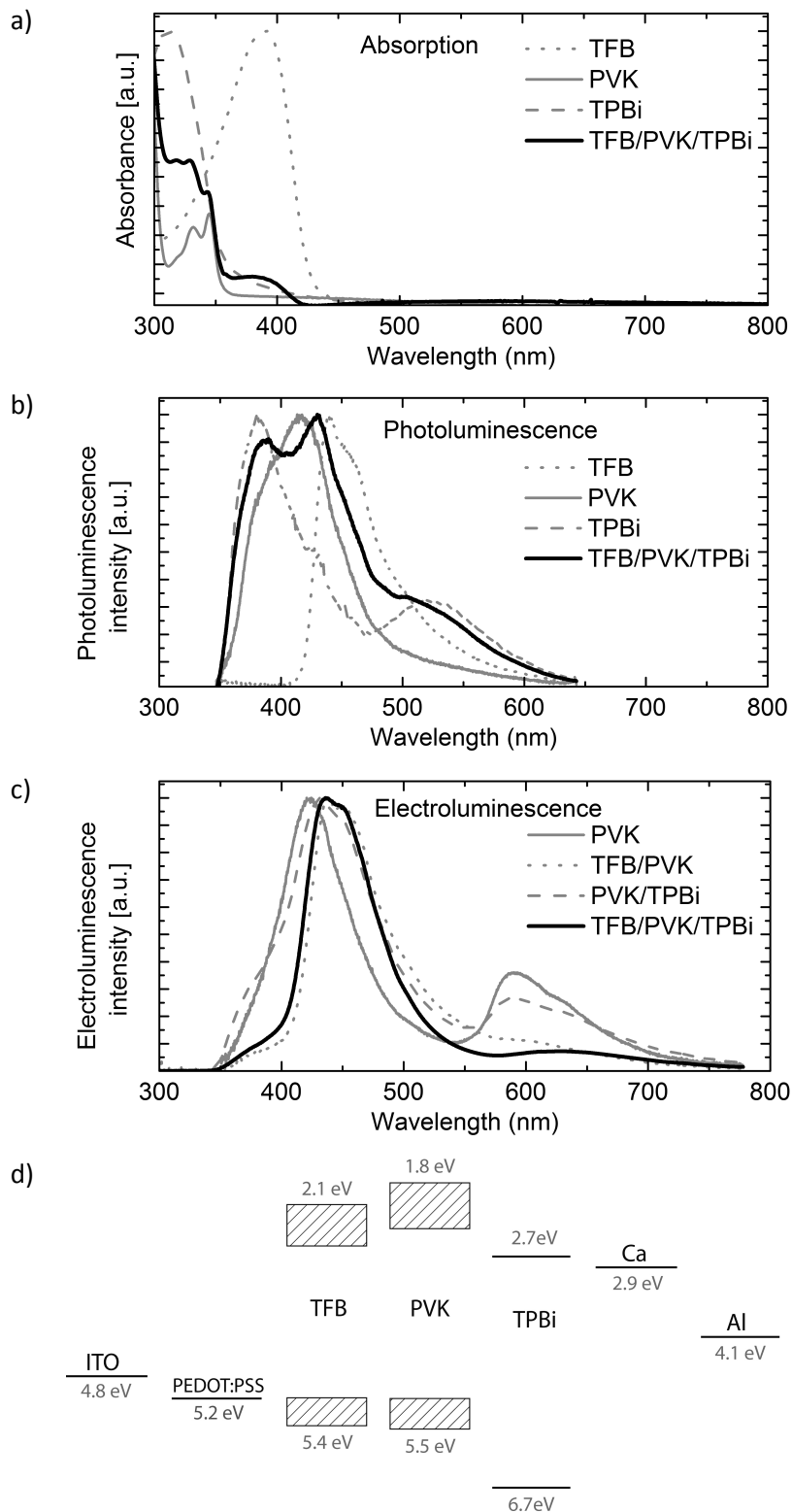


Figure 5-17 Comparison of a) the absorption b) the PL and c) the EL spectra of TFB, PVK, TPBi and TFB/PVK/TPBi in thin films and d) energy level of TFB, PVK and TPBi compared to the work function of ITO, PEDOT:PSS, calcium and aluminum. The HOMO and LUMO levels of TFB and PVK were determined by cyclic voltammetry at UCL as described in the text and in part 3.7.4. Other values are from literature [145, 148].

The EL spectra is very close to the one of TFB/PVK indicating that the recombination zone is mostly situated at the TFB/PVK interface and/or that an efficient Förster energy transfer from PVK to TFB is taking place and/or reabsorption via trivial energy transfer.

The photoluminescence decay of the trilayer was measured but could not be fitted to extract the lifetime.

Table 5-9 Summary of the photophysical data of TFB/PVK/TPBi.

Absorption	Photoluminescence	Electroluminescence	Lifetime (nm, ns)
~ 391 nm	387 nm 429 nm ~520 nm	438 nm	-

The devices with the architecture ITO/PEDOT:PSS/TFB/PVK/TPBi/Ca/Al exhibited an EQE of 0.61 %. The introduction of a TFB layer on PVK/TPBi devices had more influence than on pure PVK devices. In this case the EQE was almost doubled (from 0.27 to 0.61 %) but the turn-on voltage increased from 4.7 to 5.1 V.

Table 5-10 Summary of the properties of the ITO/PEDOT:PSS/TFB/PVK/TPBi/Ca/Al devices in average compared to pure TFB, pure PVK, TFB/PVK and PVK TPBi devices.

	Max EQE (%)	Light turn on voltage (V)	Efficiency (@10 mA.cm ⁻²) (cd.A ⁻¹)	Max luminance (@114 mA.cm ⁻²) (cd.m ⁻²)	CIE coordinates
TFB	0.01 ± 0.00	5.3 ± 0.1	0.001 ± 0.000	13 ± 1	(0.28, 0.32)
PVK	0.02 ± 0.02	6.2 ± 0.9	0.007 ± 0.008	2.1 ± 1.2	(0.28, 0.18)
TFB/PVK	0.01 ± 0.01	7.1 ± 0.7	0.006 ± 0.003	4.9 ± 1.1	(0.19, 0.16)
PVK/TPBi	0.27 ± 0.12	4.7 ± 1.7	0.24 ± 0.09	107 ± 106	(0.24, 0.17)
TFB/PVK/TPBi	0.61 ± 0.23	5.1 ± 1.7	0.45 ± 0.24	249 ± 100	(0.18, 0.11)

One can see in Table 5-10 and Figure 5-18 how the TFB/PVK/TPBi devices had improved characteristics compared to the pure PVK devices.

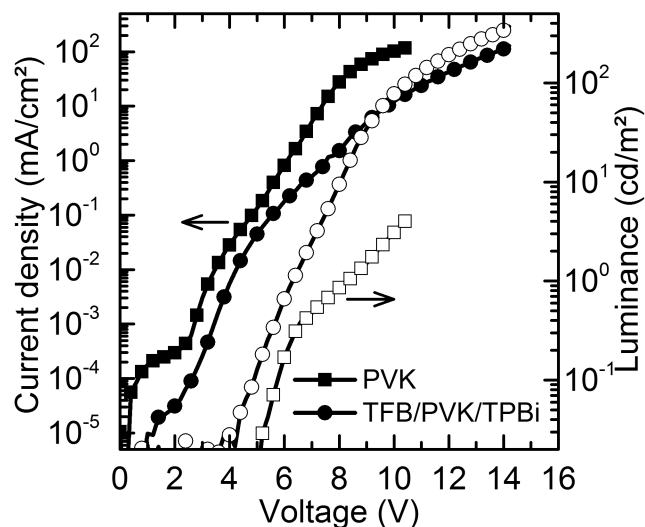


Figure 5-18 Current-voltage-light characteristics of a ITO/PEDOT:PSS/TFB/PVK/TPBi/Ca/Al device (circles) compared with pure PVK device (squares). The current densities are represented by filled symbols and luminances by empty symbols.

5.3 Conclusion

This chapter introduced the materials that were used together with novel phosphorescent compounds described in chapters 6 and 7.

The importance of the introduction of interlayers was shown: the introduction of TFB and TPBi to PVK devices led to devices with efficiencies 30 times better and lower turn-on voltages. They thus allow better injection of the charge carrier and a better balance of the charges within the device.

The photophysical properties of the single layer and multilayer devices were presented. The introduction of TPBi does not have major effect on the emission of the PVK devices, however, when TFB is used it participates to the emission. This indicates that the recombination zone is situated at the TFB/PVK interface and/or that an efficient Förster energy transfer from PVK to TFB is taking place and/or reabsorption via trivial energy transfer. Finally, the formation of new electrical species such as exciplexes was not observed.

6 OLED devices doped with Cu-complexes and spin-coated from chlorobenzene

This chapter focuses on the properties of organic light-emitting diodes, OLEDs, incorporating copper complexes from the University of Münster (WWUM), group of Luisa De Cola and synthesized by Claudia Bizzarri.

Efficient emission from the three primary colours is required for the fabrication of full colour displays. Therefore, emission wavelengths (λ_{em}), lifetimes (τ) and quantum yields (ϕ_p) must be carefully considered when designing new phosphorescent materials. Efficient red and green emitters are already available, however, blue emitters remain very challenging. Indeed, they require a large energy gap between the excited state and the ground state, making the injection of the charges more difficult.

Ideally phosphorescent compounds should have a lifetime of 5 to 50 μ s at room temperature and not longer to avoid the saturation of the excited states. Indeed, if a molecule stays in the excited state for a long period, the conversion of electronic energy into light becomes the limiting factor and inhibits the repopulation of the excited state. Furthermore, ideally the phosphorescent quantum yield of the triplet emitter should be higher than fluorescent emitter and thus at least 0.25 at room temperature. Finally the phosphorescent compounds should exhibit reversible redox behaviour, be stable and undergo vacuum sublimation or have a good solubility in organic solvents.

In copper complexes we know that the photophysics is mainly governed by the ligands, offering the possibility to tune the emission colour of the complexes. In this chapter the characteristics of devices based on six different copper complexes containing phenanthroline like ligands are presented.

6.1 The Copper compounds

When in its oxidative state +I the d orbitals of copper are completely filled and the electronic distribution of charge can be assumed as symmetrically localized around the metal centre leading to a tetrahedral conformation of the ligands. Since the d orbitals are completely filled, electronic transitions between them are prevented and as long as the π orbitals from the ligands are accessible, luminescence comes from MLCT states [149]. In solution, copper (I)-complexes exhibit a pseudo-tetrahedral geometry due to intra- and inter molecular π -stacking interactions between the ligands [150]. Since phenanthroline-like ligands exhibit low energy empty π orbitals and Cu^+ ion is easily oxidized, the lowest MLCT state can be populated upon light excitation [151].

In its excited state, the metal centre is formally oxidized from Cu (I) to Cu (II) [152, 153]. Cu (II) character favours a flattening distortion inducing a decrease in the energy available in the excited state and a reduction of the excited state lifetime. The MLCT state promotes a structural change that leads to the formation of a fifth coordination site, which can be filled by solvent or counterions via nucleophilic attacks. Exciplexes (excited state complexes), that deactivate via non-emissive path, could then be formed.

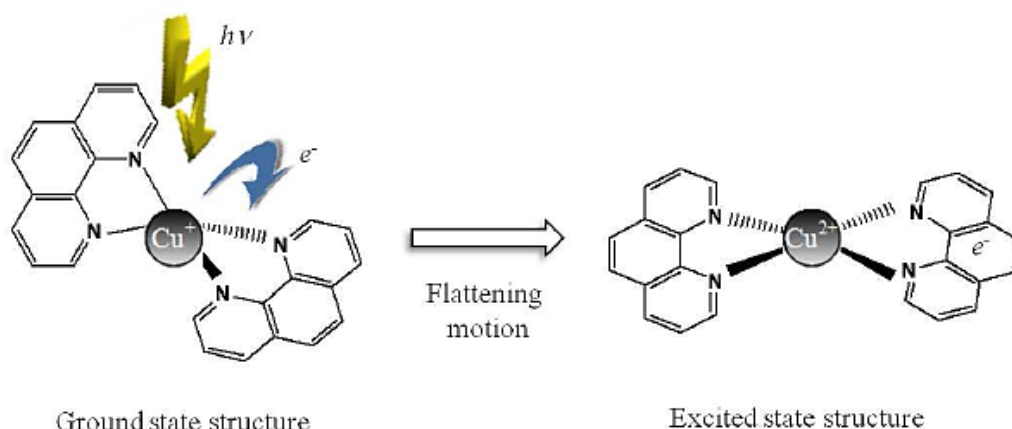


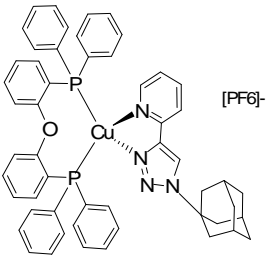
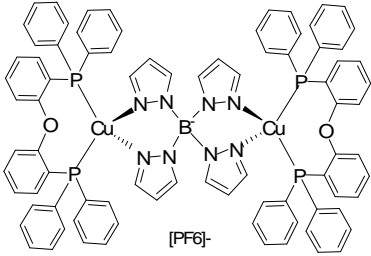
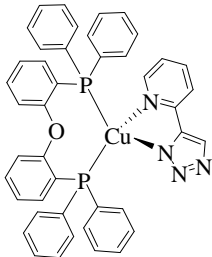
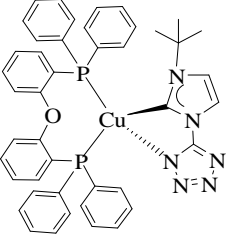
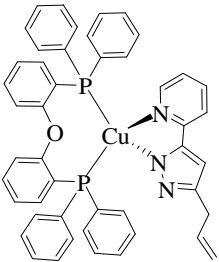
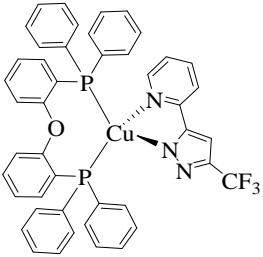
Figure 6-1 Flattening process of a Cu(I)-complex upon excitation. Reprinted with permission from [151].

Bulky substituents are one of the solutions to avoid flattening distortions in the excited state [154]. Indeed, they might reduce the extent of the distortion and prevent nucleophilic attacks to the newly formed Cu (II) ion, thus, limiting the formation of exciplexes [155].

The structures of the molecules are depicted in Table 6-1 and the photophysical and electrochemical data in Table 6-2. The molecules can be separated into two classes: the charged compounds (A and B) and the neutral compounds (C, D, E and G). They all contain bis[2-(diphenylphosphino)phenyl]ether ligand (DPEPhos) known to prevent exciplex formation between the tetrahedral complexes and the molecules of the solvent [156]. However, one can notice that the quantum yield of these compounds is higher in films than in solutions (see Table 6-2), which is believed to be the consequence of solvent induced exciplex quenching [103] in solution. The charged compounds are all PF_6^- salts to avoid nucleophilic attack by counterions.

Using different ancillary ligands the emission properties of these complexes are tuned from blue to green.

Table 6-1 Cu(I)-complexes, synthesized at WWUM

A	B
	
C	D
	
E	G
	

Photophysical characterizations of these compounds were carried out mostly at Münster University, group of Luisa De Cola and the results are summarized in Table 6-2. They were performed in dichloromethane, a non coordinating solvent, to avoid the dissociation of DPEPhos [157, 158].

6.1.1 Absorption

An intense absorption in the 260 to 300 nm region is observed in Figure 6-2 and attributed to π - π^* transitions localised on the chelating phosphine and called ligand-centered transitions (LC) [149]. The shoulders appearing between 300 nm to 355 nm are due to electronic transitions from the d orbital of the metal centre to the π^* of the ancillary ligand. Finally, the lower energy absorption bands, localized between 350 nm and 400 nm are less intense and can be assigned to a singlet MLCT transition involving a d metal orbital and a π^* ligand orbital [151].

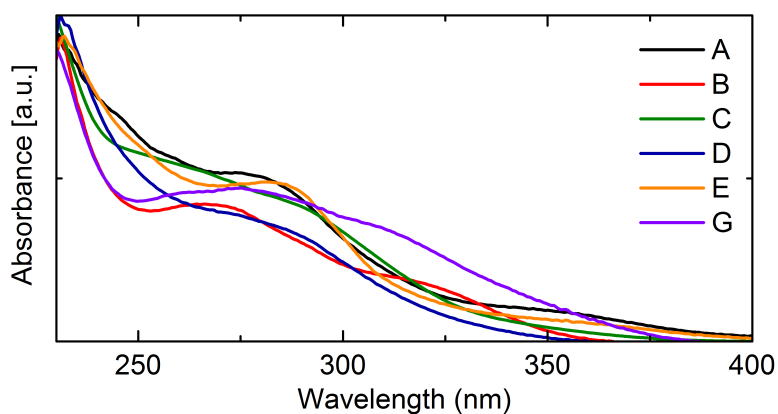


Figure 6-2 Absorption spectra of the compound in dichloromethane solution [data from WWUM].

One can notice that the compounds absorb at very low wavelengths making the choice of the host even more difficult since polymers such as PVK emits in the blue at around 416 nm (see part 5.1.1). This configuration is thus not ideal for energy transfer to take place.

6.1.2 Emission properties in solution at room temperature

The photoluminescent spectra at room temperature were measured from oxygen free dichloromethane to avoid quenching from oxygen. All compounds are luminescent, exhibit broad unstructured emission and a large stoke shift characteristic of metal-to-ligand charge transfer phosphorescence. Since the emissive state has a $d-\pi^*$ character, the colour of the luminescence could be tuned by using different ancillary ligands. The HOMO values are predominantly influenced by the DPEPhos-Cu(I) moiety whereas the LUMO is principally influenced by the ancillary ligands via their π^* orbitals [158-160].

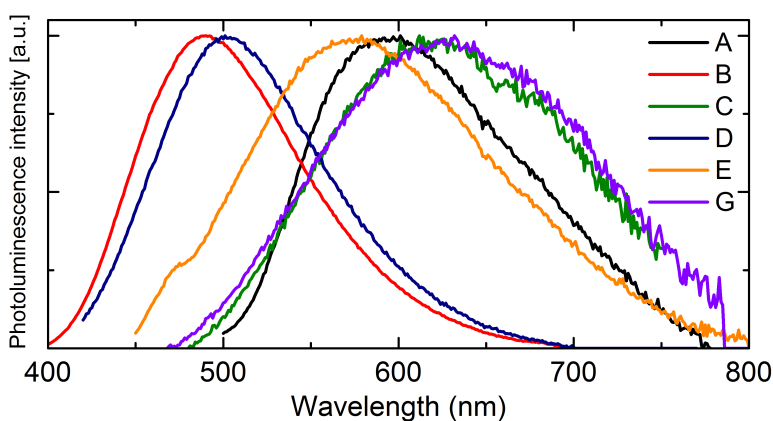


Figure 6-3 Photoluminescence spectra of the compounds in deoxygenated dichloromethane solution at room temperature [Data from WWUM].

The quantum yields displayed in Table 6-2 were calculated using the relative method [161]. The fact that they are low in solution could be explained by the fact that the MLCT states of Cu(I) are quenched in solution [162, 163].

6.1.3 Emission in solid state at low temperature

At low temperature, bond vibrations and rotations are restrained due to the rigid environment formed by the glassy solvent. As a consequence the emission spectra are blue shifted leading to a decrease of the stoke shift. Since the solvent molecules are prevented from rearranging around the excited complex, there is no solvent

stabilization [164]. Distortions are inhibited and lifetimes are enhanced up to the microsecond range.

The triplet energy levels reported in Table 6-2 were deduced from the photoluminescence spectra carried out at low temperature.

6.1.4 Emission in solid state at room temperature

Photoluminescence measurements in solid state were performed on films drop cast from dichloromethane. The PL quantum efficiency in thin film is higher than in solution and is a consequence of the fact that in solution exciplex formation is favoured between the solvent and the distorted tetrahedral Cu (I) complex in its excited state [165].

Asano et al. [166] reported that phenanthrolines copper (I) complexes exhibit thermally activated delayed fluorescence at room temperature. However, this was not confirmed by experiments carried on these copper compounds [151].

Considering the photophysical properties of these compounds, their stability and their good solubility in organic solvents, devices were made using PVK as the matrix and TPBi as the electron injection layer.

Table 6-2 Photophysical and electrochemical data of the new Cu(I)-complexes. Data from WWUM.

Compound	SOLUTION ^a				THIN FILM				
	λ_{em}	HOMO	LUMO	Φ	λ_{em}	Φ	τ	Emission at 77K	Triplet energy E_T
A	600 nm	-5.12 ± 0.10 eV	-2.62 ± 0.49 eV	0.13 % (dcm)	519 ^b nm 510 ^d nm	1 % ^b 30.7 % ^d	21.75 μ s (%) ^d 36.75 μ s (%) ^d	512 nm	2.44 eV
B	463 nm	-5.15 ± 0.10 eV	--	3.4 % (dcm)	452 ^b nm 453 ^d nm	4.5 % ^b 15.4 % ^d	6.59 μ s (21.5 %) ^d 24.5 μ s (78.5 %) ^d	434 nm	2.87 eV
C	615 nm	-5.10 ± 0.10 eV	--	0.58 % (dcm)	504 ^b nm 506 ^d nm	20 % ^d	32.5 μ s ^d	520 nm	2.40 eV
D	549 nm	-5.06 ± 0.09 eV	-2.72 ± 0.49 eV	0.45 % (dmf)	490 ^b nm 454 ^d nm	4 % ^b 2 % ^c 12 % ^d	21.1 μ s ^d	445 nm	2.80 eV
E	578 nm	-5.03 ± 0.09 eV	-2.66 ± 0.49 eV	0.61 % (dcm)	525 ^b nm 505 ^d nm	5 % ^b 22 % ^c 33.5 % ^d	5.7 μ s (6.2 %) ^d 21.1 μ s (93.8 %) ^d	515 nm	2.42 eV
G	632 nm	-4.96 ± 0.09 eV	-2.44 ± 0.51 eV	0.08 % (dcm)	531 ^b nm	9 % ^b 12 % ^d	25.2 μ s ^d	528 nm	2.36 eV

^a photophysics measured in dry and freshly distilled DCM; quantum yield Φ measured in specified different solvents; electrochemistry in dry DMF. HOMO-LUMO values are calculated from potential values.

^b neat film;

^c 5% in PMMA;

^d 10% in PMMA.

6.2 Experiments

6.2.1 Fabrication of the devices

At first all compounds were tested within devices with the structure: ITO/PEDOT:PSS/PVK:Triplet/TPBi (30 nm)/Ca (30 nm)/Al (150 nm). The ITO was oxygen plasma treated for 10 minutes immediately prior to the spin-coating of the PEDOT:PSS, which was then baked under nitrogen atmosphere at 180°C for 10 minutes on a hot plate to remove any remaining solvent.

The active layer consisted of either the pure polymer (PVK) or a blend of PVK with triplet emitters. These were spin-coated in nitrogen atmosphere from 1 wt. % solutions of the polymer or blends in chlorobenzene. The thickness of these films was around 70 nm.

6.2.2 PVK/TPBi devices

PVK/TPBi devices are described in part 5.2.3.

6.2.3 Discussion on the energy levels

The energy diagram of the materials used in the devices is shown in Figure 6-4. The HOMO and LUMO levels of TFB, PVK and TPBi were already compared and discussed in chapter 5. In the presence of a guest, exciplexes may be formed at the PVK/guest interface (in case of the formation of a favourable dipole, see part 2.5) and at the TPBi/guest interface. For the devices with a TFB interlayer even more exciplexes could be formed at the TFB/guest interface.

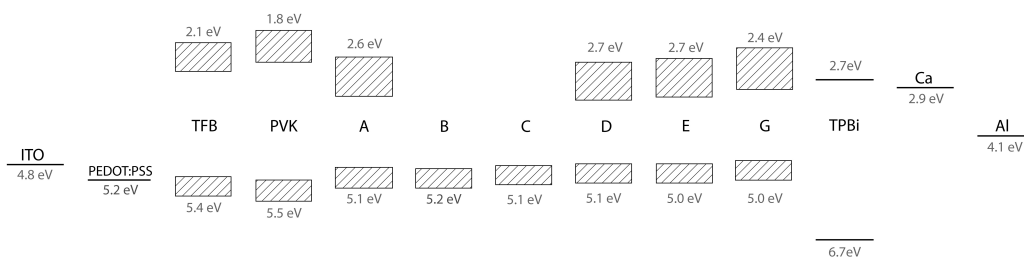


Figure 6-4 Energy diagram of the materials used in this chapter compared with the work functions of the electrodes. The HOMO and LUMO levels of A, B, C, D, E and G were determined by cyclic voltammetry at WWUM and TFB and PVK at UCL, the errors on the values are represented. No LUMO data are available for B and C. Other values were taken from literature [145, 148].

The triplet energies of the compounds are plotted in Figure 6-5. One can notice that the situation is not ideal for all compounds. As it has already been said the triplet energy level of the host has to be higher than that of the guest. In case of PVK, the dimer emission acts as a trap [120] and, therefore, the triplet energy of the compounds should be lower than that of the dimer emission to avoid back transfer of energy from emitter to host. Compounds B and D have their triplet levels lying close to the one of PVK and, therefore, above the one of the dimer emission meaning that the recombination is more likely to happen on the host than on the guest. The other compounds seem to have their triplet levels below the one of PVK and of the dimer emission and consequently are in the desired configuration.

In order to confine the triplet excitons within the emissive layer it is also desirable that the triplet energy levels of the hole and electron injection layers are higher than that of the guest and the host. TPBi should thus confine the triplet excitons of the compounds A, C, E and G but not the ones of PVK. TFB will not act as a confinement layer with its triplet energy level at 2.25 eV and, therefore, below the ones of PVK and the copper complexes.

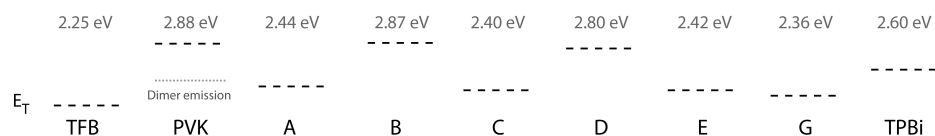


Figure 6-5 Triplet energy E_T of each compound. The values of the triplet energy and the dimer emission energy (2.5 eV) of PVK has been taken from [120], TFB from [142], TPBi from [107].

6.2.4 Effect of the triplet concentration

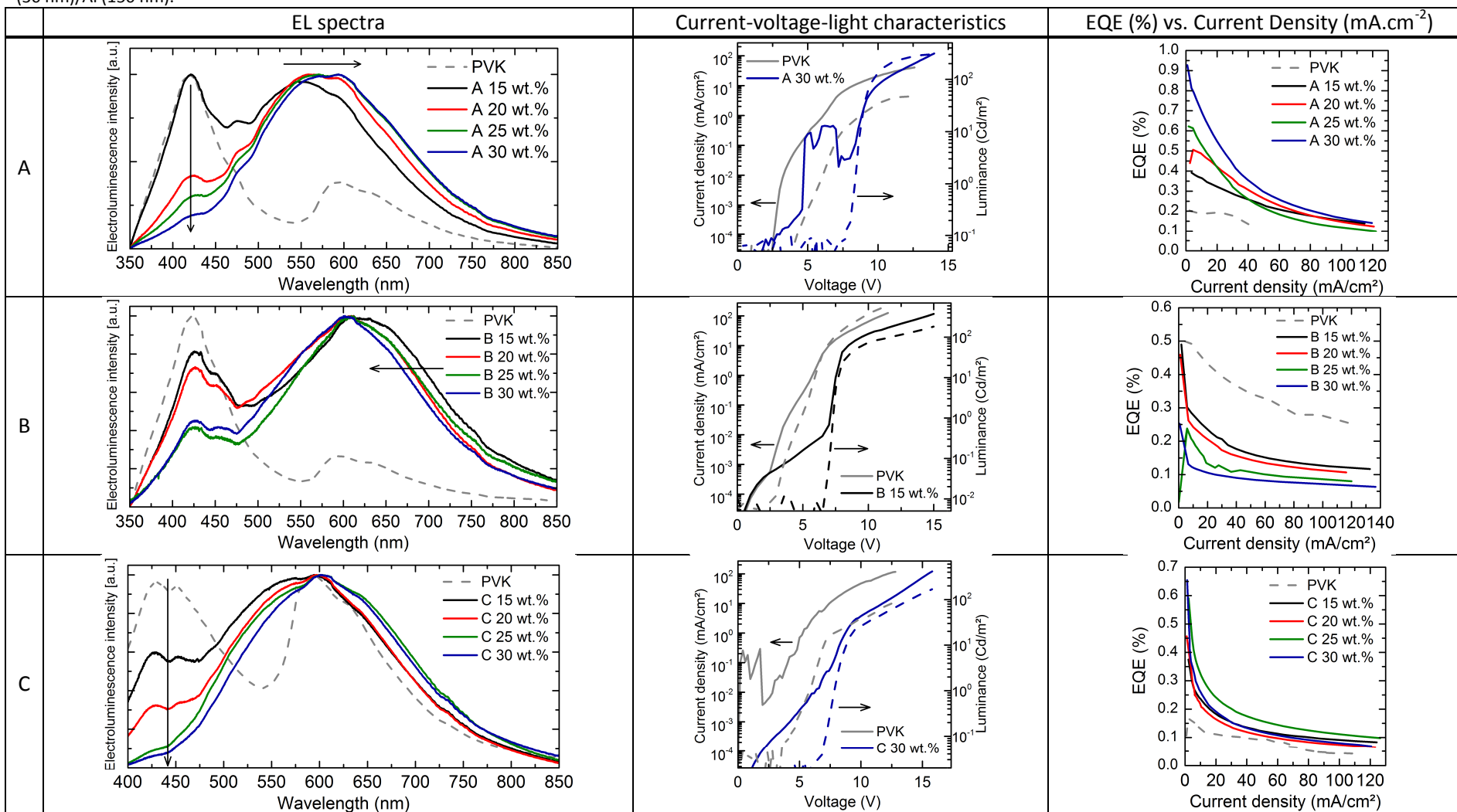
6.2.4.1 Results

All compounds were tested with 15, 20, 25 and 30 wt. % in PVK and the corresponding device parameters as well as the electroluminescence spectra, current-voltage-light characteristics, EQE versus current density and CIE coordinates are shown in Table 6-3 ,Table 6-4 and Table 6-5.

Table 6-3 Properties of the ITO/PEDOT:PSS/PVK:copper complex/TPBi/Ca/Al devices over a range of triplet compositions.

Wt. %	Max EQE (%)	Light turn on voltage (V)	Efficiency (@10 mA.cm ⁻²) (cd.A ⁻¹)	Max luminance (@114 mA.cm ⁻²) (cd.m ⁻²)	CIE coordinates	
A	0	0.18 ± 0.03	3.8 ± 0.3	0.14 ± 0.02	51 ± 10	(0.29, 0.21)
	15	0.39 ± 0.14	8.8 ± 0.8	0.58 ± 0.09	212 ± 40	(0.32, 0.35)
	20	0.50 ± 0.30	7.4 ± 1.2	0.71 ± 0.20	197 ± 50	(0.37, 0.41)
	25	0.57 ± 0.23	7.5 ± 1.5	0.89 ± 0.19	220 ± 90	(0.39, 0.43)
	30	0.90 ± 0.14	7.6 ± 1.4	1.15 ± 0.19	250 ± 50	(0.40, 0.44)
B	0	0.50 ± 0.10	5.1 ± 0.5	0.67 ± 0.06	460 ± 100	(0.26, 0.18)
	15	0.49 ± 0.05	8.3 ± 1.3	0.34 ± 0.04	177 ± 13	(0.37, 0.34)
	20	0.45 ± 0.14	7.2 ± 0.3	0.32 ± 0.03	160 ± 20	(0.38, 0.35)
	25	0.26 ± 0.10	7.6 ± 0.9	0.25 ± 0.04	120 ± 20	(0.42, 0.39)
	30	0.23 ± 0.09	7.3 ± 0.3	0.19 ± 0.02	115 ± 15	(0.40, 0.39)
C	0	0.18 ± 0.10	4.8 ± 0.2	0.19 ± 0.16	72 ± 15	(0.36, 0.28)
	15	0.38 ± 0.11	9.0 ± 0.6	0.39 ± 0.06	167 ± 20	(0.37, 0.38)
	20	0.48 ± 0.17	8.8 ± 0.8	0.41 ± 0.07	140 ± 26	(0.39, 0.37)
	25	0.55 ± 0.21	8.4 ± 1.3	0.42 ± 0.16	146 ± 68	(0.35, 0.37)
	30	0.58 ± 0.23	8.2 ± 1.4	0.40 ± 0.08	148 ± 32	(0.34, 0.39)
D	0	0.14 ± 0.08	8.7 ± 4.0	0.03 ± 0.01	12 ± 2	(0.35, 0.32)
	15	0.081 ± 0.010	10.9 ± 0.3	0.06 ± 0.01	22 ± 5	(0.37, 0.36)
	20	0.089 ± 0.020	11.1 ± 1.4	0.07 ± 0.01	29 ± 4	(0.39, 0.38)
	25	0.098 ± 0.020	10.7 ± 0.7	0.10 ± 0.02	53 ± 14	(0.40, 0.38)
	30	0.11 ± 0.01	9.7 ± 0.7	0.11 ± 0.01	75 ± 20	(0.44, 0.45)
E	0	0.19 ± 0.04	3.3 ± 0.1	0.20 ± 0.04	112 ± 35	(0.32, 0.24)
	15	0.41 ± 0.12	10.3 ± 3.7	0.52 ± 0.23	228 ± 35	(0.43, 0.44)
	20	0.51 ± 0.16	10.4 ± 0.6	0.59 ± 0.08	192 ± 47	(0.44, 0.47)
	25	0.56 ± 0.25	11.0 ± 0.4	0.61 ± 0.11	176 ± 52	(0.43, 0.46)
	30	0.76 ± 0.28	10.6 ± 1.0	0.75 ± 0.05	197 ± 61	(0.42, 0.46)
G	0	0.21 ± 0.03	3.7 ± 0.3	0.20 ± 0.03	101 ± 09	(0.32, 0.26)
	15	0.91 ± 0.35	8.7 ± 0.5	0.84 ± 0.17	125 ± 40	(0.41, 0.43)
	20	1.18 ± 0.34	9.1 ± 0.4	0.75 ± 0.23	99 ± 48	(0.41, 0.44)
	25	1.21 ± 0.29	8.8 ± 0.7	1.00 ± 0.37	106 ± 65	(0.41, 0.46)
	30	1.10 ± 0.40	7.8 ± 1.6	0.90 ± 0.23	85 ± 31	(0.42, 0.46)

Table 6-4 Electroluminescence spectra, current-voltage-light characteristics, EQE versus current density of the devices made with the structure ITO/PEDOT:PSS/PVK:triplet/TPBi (30 nm)/Ca (30 nm)/Al (150 nm).



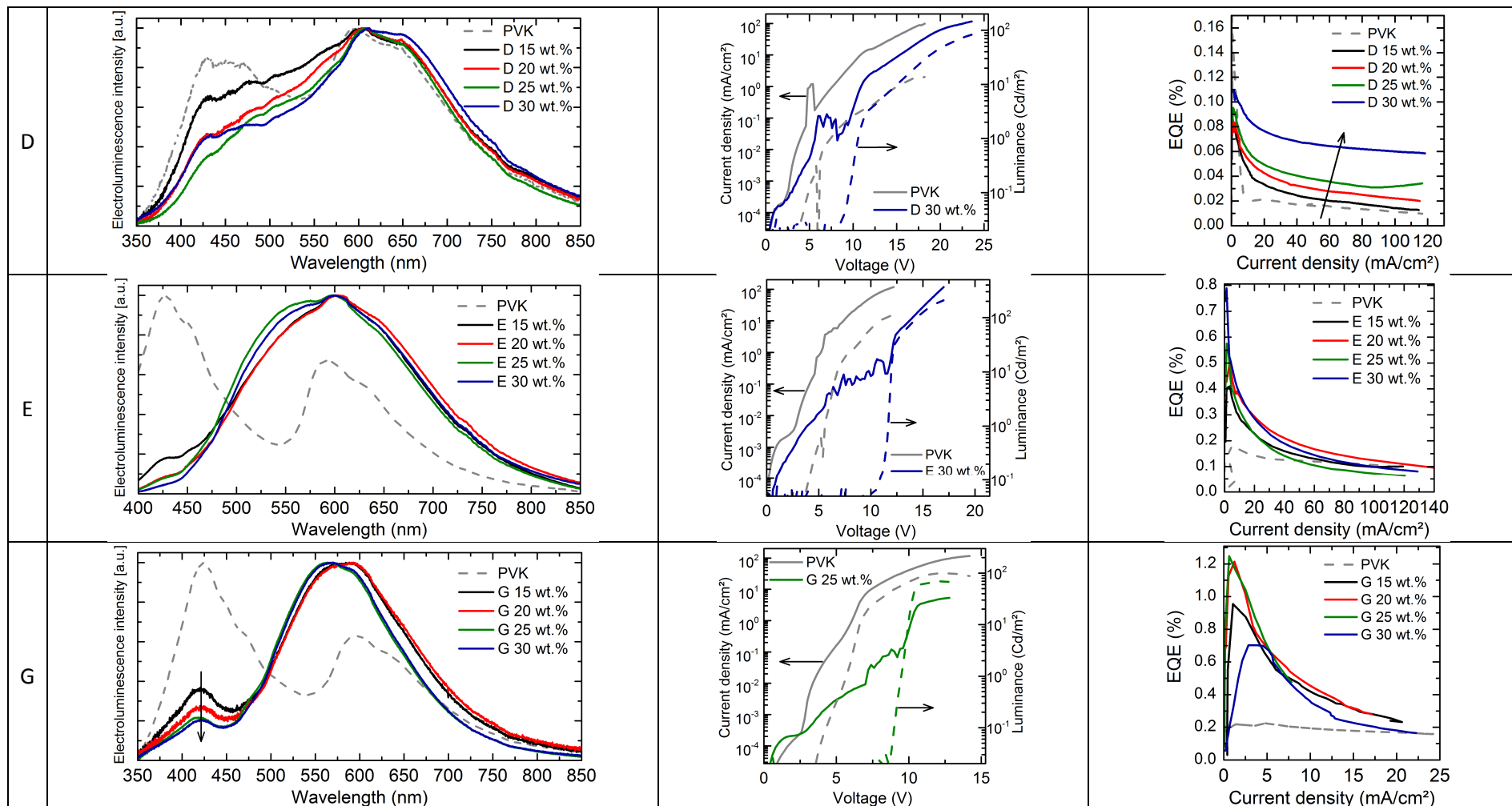
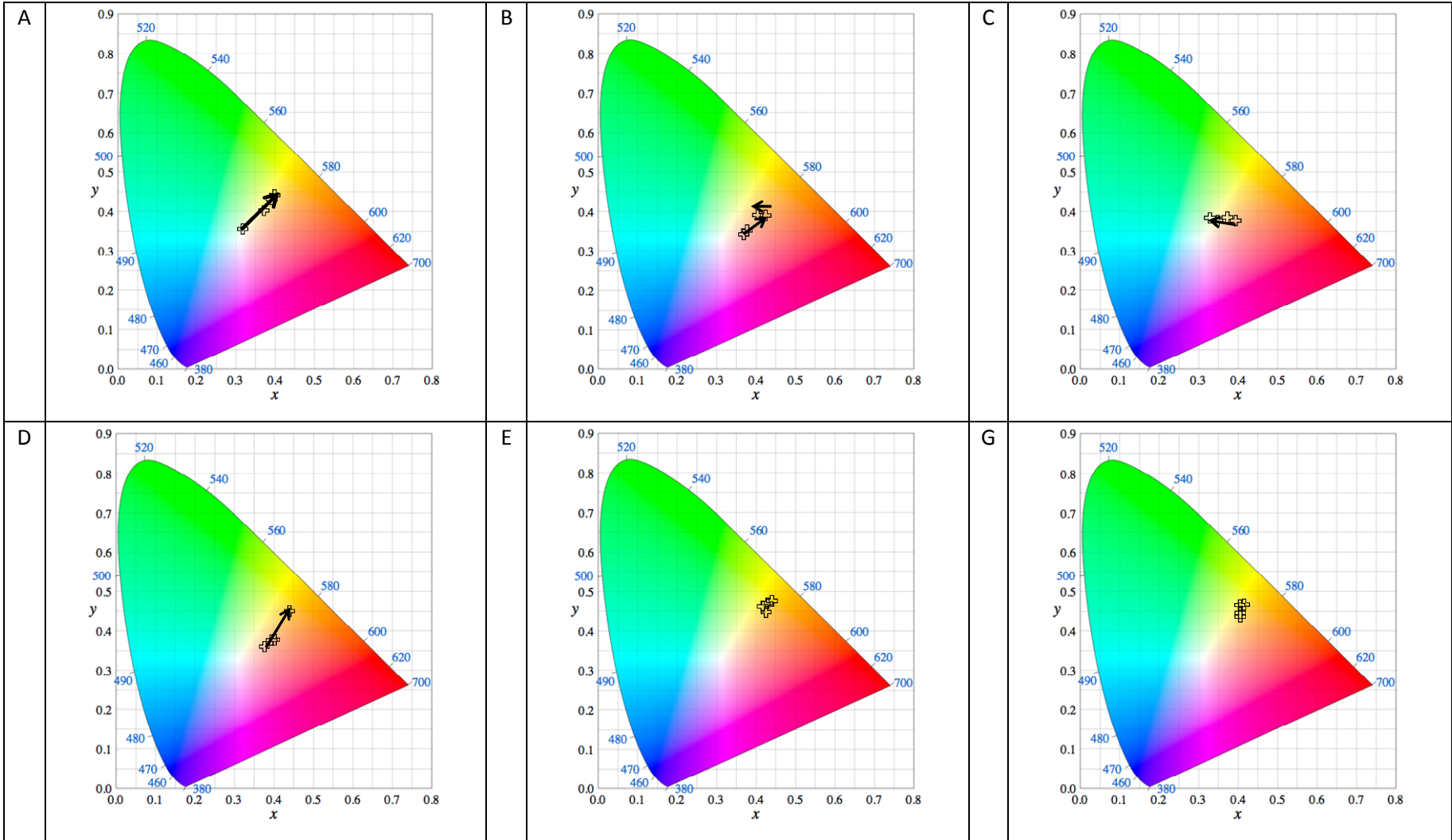


Table 6-5 CIE coordinates of the devices for the different concentrations



Compound A

The EQE of compound A increased with its concentration of PVK from 0.39 to 0.90 %, and the comparison between the EL spectra clearly shows an enhanced energy transfer from PVK to the guest with increasing concentration. The CIE coordinate calculations show a straight line from white to orange with increasing concentration of A from 15 to 30 wt. %. No trend was observed in the light turn-on voltages which varied between 7.4 and 8.8 V. This compound showed the highest luminance of all the compounds tested with a maximum luminance of 350 cd.m⁻² and the best current efficiency (1.15 cd.A⁻¹). However, it showed degradation at high voltages, possibly due to charge migration under electric field.

Compound B

Contrary to compound A, the EQE decreased with increasing B concentration from 0.49 to 0.23 %. The best efficiency was then obtained for 15 wt. % devices (lowest concentration tested). The EL spectra show a bad energy transfer from PVK to the triplet emitter, this was expected considering the triplet energy levels configuration (see Figure 6-5). Again no trend could be extracted out of the light turn-on voltages which ranged from 7.2 to 8.3 V. The colour was in the white/orange region. The EQE of the triplet devices did not exceed the one of pure PVK, but the pure PVK device in this batch was particularly efficient.

Compound C

The EQE of compound C increased from 0.38 to 0.58 % when the concentration increased from 15 to 30 wt. % with turn-on voltages varying between 8.2 and 9 V. The EL spectra taken at different concentration show a good energy transfer from the guest to the host confirming the data on the energy levels.

Compound D

Again the EQE increased with increasing concentration of PVK but values were low and did not even exceed the EQE of pure PVK (0.081 to 0.11 %). This may be due to an

experimental error on the thickness of PVK which appeared pink instead of violet. But low efficiencies were expected since the triplet level configuration is unfavourable (i.e. the triplet level of the guest is higher than the one of PVK). Once again no trend was noticed for the turn-on voltages which are between 9.7 and 11.1 V, but they were the highest ones among all the batches tested. The colour was white/orange but contained pink arising from PVK emission.

Compound E

Compound E presented one of the best neat film photoluminescence efficiency, but the devices exhibited efficiencies up to only 0.76 % at 25 wt. %. The turn-on voltages were among the highest of all materials and ranged from 10.3 to 11 V. The energy transfer was very good already at 15 wt. %, which is the reason why the colour did not change dramatically with increasing concentration but stayed in the yellow range.

Compound G

Compound G showed the highest neat film PL efficiency. Its EQE increased with higher concentration and its EL spectra show a rather good energy transfer (but not as good as compound A). The best efficiency was achieved for 25 wt. % with 1.21 % EQE. The current densities were much lower than the ones of the other compounds. The colour was in the yellow range. Again no trend could be observed from the turn-on voltages which were between 7.8 and 9.1 V.

General observations

Looking at the behaviour of the PVK/TPBi devices (without addition of a triplet emitter) for each batch, the EL spectra and the characteristics of the devices are varying from batch to batch. These variations could be due to differences in the thickness or concentration of PVK of the layers [40].

As we can see on the EQE versus current density graphs in Table 6-4, all devices undergo a decrease in efficiency with increasing current density/ brightness often due to triplet-triplet quenching. Indeed, when sufficient triplet excited states are formed, they

can undergo the spin-allowed process called triplet-triplet annihilation (TTA) leading to one singlet excited state S_1 and a singlet ground state S_0 ($T_1 + T_1 \rightarrow S_0 + S_1$) [156, 167]. In this case, the decay of the singlet excited states will lead to delayed fluorescence.

As expected from the triplet energy level comparison, compounds A, C, E and G showed good energy transfer from PVK to the triplet emitter contrary to B and D. These results tend to prove that despite the small overlap between the PL of PVK (or PVK/TPBi) and the absorption of the metal transition complex, energy transfer was taking place and this will be confirmed by the PL measurements performed on compound A in part 6.3.1.2.

For all compounds the effect of the electric field on the emission wavelength was negligible since the EL spectra were not affected by a change in the driving voltage (not shown), reflecting the rigidity of the molecules.

In the case of direct carrier trapping, the guest molecules would act as shallow trapping centres, which would trap charge carriers and, therefore, change the charge density. The current-voltage characteristics would, thus, be dependent on the guest concentration whereas in case of energy transfer, current-voltage characteristics are not sensitive to the variation of the guest concentration [121]. Since for all compounds the current-voltage characteristics were not dependent on the doping concentration (not shown), energy transfer might explain the obtained EL spectra rather than charge carrier trapping.

When the PL emission of the compounds was measured, they all presented different maximum emission wavelengths and thus different colours. However, once blended with PVK in devices they all emitted in the white/orange region. This issue will be discussed in part 6.3.

6.2.5 Insertion of a hole-injecting layer: TFB

6.2.5.1 Preliminary test

To try to further enhance the characteristics of the devices, a hole-injecting layer was added: TFB. Before studying the effect of the concentration of the triplets on the characteristics of the devices, a quick test was done on A, C, E and G at 25 wt. % in PVK

to see the general influence of TFB and which material benefits the most from its insertion.

Devices were made with the architecture ITO/PEDOT:PSS/TFB/PVK:A, C, E or G 25 wt. %/TPBi/Ca/Al. It has to be kept in mind that for this experiment the amount of material weighed was low (~2 mg) leading to a high uncertainty on the mass measured and then on the concentration of the solutions. TFB (2 wt. % in p-xylene) was spin-coated on top of PEDOT:PSS, then annealed at 180°C for 1hour prior to being spin-rinsed with p-xylene. The results are summarised in Table 6-6 and Figure 6-7.

First of all, the comparison of the EL spectra (see Figure 6-6) of TFB/PVK/TPBi devices with PVK/TPBi devices (without guest) shows a small red-shift, a narrowing of the emission and a very weak emission around 600 nm.

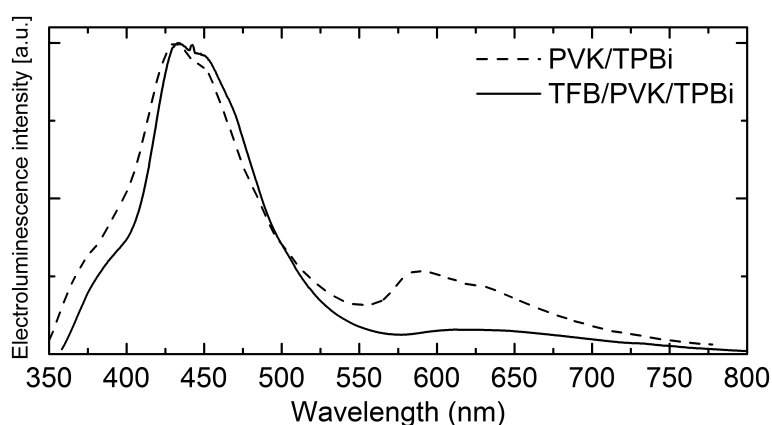


Figure 6-6 EL spectra comparison between PVK/TPBi and TFB/PVK/TPBi devices.

Table 6-6 Properties of the ITO/PEDOT:PSS/TFB/PVK:copper complex/TPBi/Ca/Al devices in average.

Wt. %	Max EQE (%)	Light turn on voltage (V)	Efficiency (@10 mA.cm ⁻²) (cd.A ⁻¹)	Max luminance (@114 mA.cm ⁻²) (cd.m ⁻²)	CIE coordinates
TFB/PVK	0.46 ± 0.08	5.3 ± 1.6	0.28 ± 0.04	173 ± 10	(0.18, 0.12)
A 25	1.07 ± 0.19	6.7 ± 2.5	1.55 ± 0.14	407 ± 81	(0.33, 0.40)
C 25	0.71 ± 0.12	6.3 ± 0.9	0.81 ± 0.08	207 ± 39	(0.34, 0.37)
E 25	0.66 ± 0.12	7.2 ± 0.3	0.76 ± 0.14	317 ± 42	(0.30, 0.29)
G 25	0.85 ± 0.08	6.7 ± 1.5	1.19 ± 0.13	335 ± 69	(0.35, 0.35)

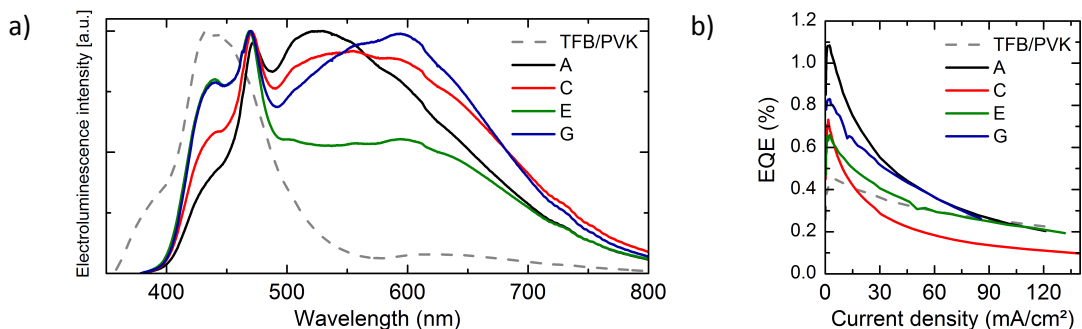


Figure 6-7 a) Electroluminescence spectra and b) EQE versus current density of pure PVK (dashed line), PVK with 25 wt.% of A, C, E and G with the structure ITO/PEDOT:PSS/TFB/PVK:triplet/TPBi (30 nm)/Ca (30 nm)/Al (150 nm).

From the EL spectra of devices containing a triplet emitter (see Figure 6-7), one can see the formation of a peak at the same wavelength of 468 nm for each compound. This could be due to emission from pure TFB or the formation of an exciplex at the interface TFB/guest with the electron on the guest and the hole on TFB. Due to the high uncertainty on the LUMO values, it is difficult to check if this hypothesis is consistent with the energy levels.

By comparing Table 6-3 and Table 6-6, one can see that the insertion of the TFB interlayer did not have a significant influence on the EQEs of the devices but did have a positive effect on the light turn-on voltage, the current density, the current efficiency and the luminance. These improvements are the consequences of a better hole injection and have already been observed by different groups [18, 23, 168].

Compound A shows the best overall results and a good improvement of its characteristics. Indeed, its EQE increased from 0.6/0.9 to 1.1 %, the current efficiency from 0.89/1.15 to 1.55 cd.A⁻¹, its maximum luminance from 220/250 to 410 cd.m⁻² and its turn-on voltage dropped from 7.5/7.6 to 6.7 V.

From these results the use of TFB as an interlayer seems to be a good approach to improve the overall characteristics of the devices. The next step was to study the effect of the guest concentration on the performances of the devices.

6.2.5.2 Effect of the guest concentration

Since compound A showed the best characteristics and the lowest contribution of TFB on its EL spectra after the first TFB test, it was decided to study the effect of the guest concentration on the characteristics of the devices.

Devices were made using the same procedure as the previous devices with a concentration of A of 25, 30, 35 and 40 wt. % in PVK.

Table 6-7 Properties of the ITO/PEDOT:PSS/TFB/PVK:A/Ca/Al devices over a range of triplet concentrations.

Wt. %	Max EQE (%)	Light turn on voltage (V)	Efficiency (@10 mA.cm ⁻²) (cd.A ⁻¹)	Max luminance (@114 mA.cm ⁻²) (cd.m ⁻²)	CIE coordinates	
A	0	0.35 ± 0.11	4.8 ± 1.4	0.22 ± 0.06	140 ± 47	(0.19, 0.12)
	25	0.77 ± 0.08	5.9 ± 1.7	1.20 ± 0.75	395 ± 112	(0.29, 0.32)
	30	0.82 ± 0.12	5.6 ± 1.6	1.27 ± 0.11	421 ± 97	(0.32, 0.36)
	35	1.12 ± 0.41	5.8 ± 1.8	1.50 ± 0.11	479 ± 230	(0.33, 0.37)
	40	1.21 ± 0.09	5.6 ± 1.4	1.78 ± 0.10	408 ± 71	(0.33, 0.39)

The results presented in Table 6-7 show an improvement of the characteristics with increasing concentration of A. An EQE of 1.21 % and a current efficiency of 1.78 cd.A⁻¹ were achieved with a turn-on voltage of 5.6 V. These results were the best of all experiments. The EL spectra in Figure 6-8 show again a peak but at 453 nm instead of 468 nm that could be an indication of the presence of exciplexes at the interface TFB/guest (see part 3.2.4.1). However, due to the complexity of the system (the three compounds exhibit similar absorption and/or emission spectra), it was not possible to check this assumption via time resolved techniques. The origin of the shift of the peak between the two experiments (parts 6.2.5.1 and 6.2.5.2) might be due to a small shift in the wavelength calibration of the ANDOR that presents a sharp increase in its response function between 460 and 500 nm. A small shift at these wavelengths can thus lead to a significant error.

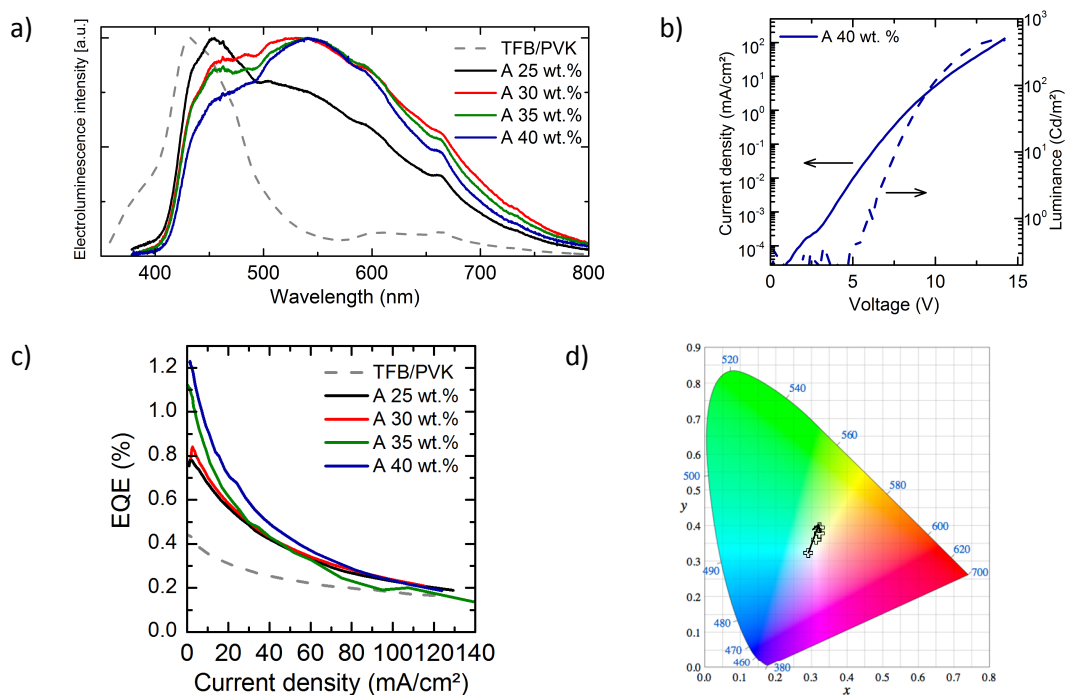


Figure 6-8 a) Electroluminescence spectra, b) current-voltage-light characteristics, c) EQE versus current density and d) CIE coordinates of the devices made with the structure ITO/PEDOT:PSS/TFB/PVK:A/TPBi (30 nm)/Ca (30 nm)/Al (150 nm) with concentration of A of 0 (dashed line), 25, 30, 35 and 40 wt. %.

The colour achieved with this configuration and material A is close to white as we can see on Figure 6-8 d).

Park et al. reported the triplet energy of TFB to be between 2.2 and 2.3 eV. TFB, therefore, does not confine the triplet exciton within the emissive layer since the triplet level of A is 2.4 eV (see Figure 6-5) and 2.5 eV for PVK (triplet dimer trap). This could explain the fact that the external quantum efficiencies of the devices were not significantly enhanced and that the concentration of copper complexes in the host had to be increased when TFB was added despite the improved charge injection.

6.3 Photophysical results

The fact that all devices exhibited a white orange colour despite of the blue or green compounds aroused the question of an exciplex formed at the PVK/guest interface. In an attempt to understand better the origin of the electroluminescence spectra

measured from the devices, photophysical experiments on compound A were performed.

6.3.1 Compound A

6.3.1.1 Pure A

The absorption maximum of A is around 277 nm and its maximum PL is at 520 nm as seen in Figure 6-9.

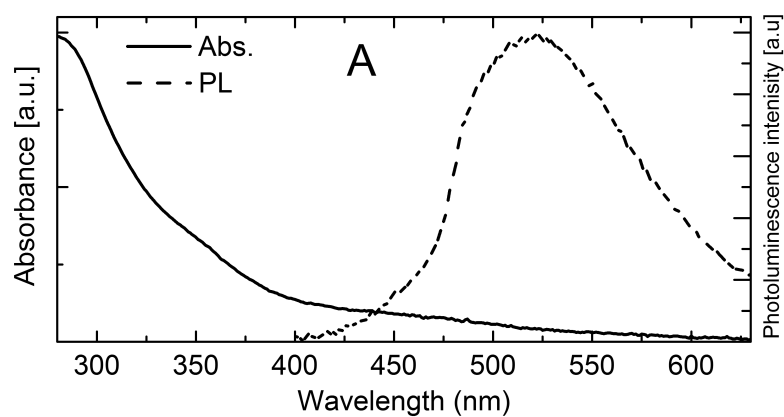


Figure 6-9 Absorption (black line) and PL spectra of pure A 1wt.% in chlorobenzene (black dashed line).

The photoluminescence decay of pure A, spin-coated from 1 wt. % in chlorobenzene, was measured and is shown in Figure 6-10. The exponential fit indicates that the triplet exciton lifetime is 10 μ s. The faster decay could not be resolved with our equipment.

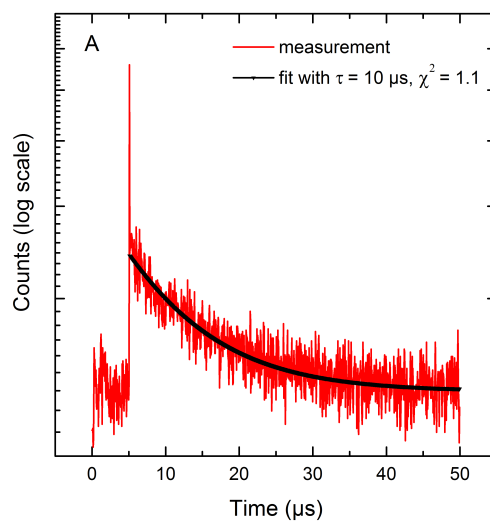


Figure 6-10 Time resolved photoluminescence spectra with a pulsed laser beam at 371 nm entering from the polymer side. Emission at 520 nm.

All the results regarding absorption and emission maxima as well as lifetimes are gathered in Table 6-8.

Table 6-8 Summary of the photophysical data of A.

	Absorption	Photoluminescence	Lifetime
A (CB)	~ 277 nm	520 nm	(520 nm, 20 & 50 μs) $\tau_1: 0.034 \pm 0.001$ ns (1.5%) $\tau_2: 10.52$ μs (98.5%)

6.3.1.2 Blend of PVK and A

In the same way the absorption and PL spectra of the blend PVK:A with 25 wt. % of A in PVK were measured and are plotted in Figure 6-11.

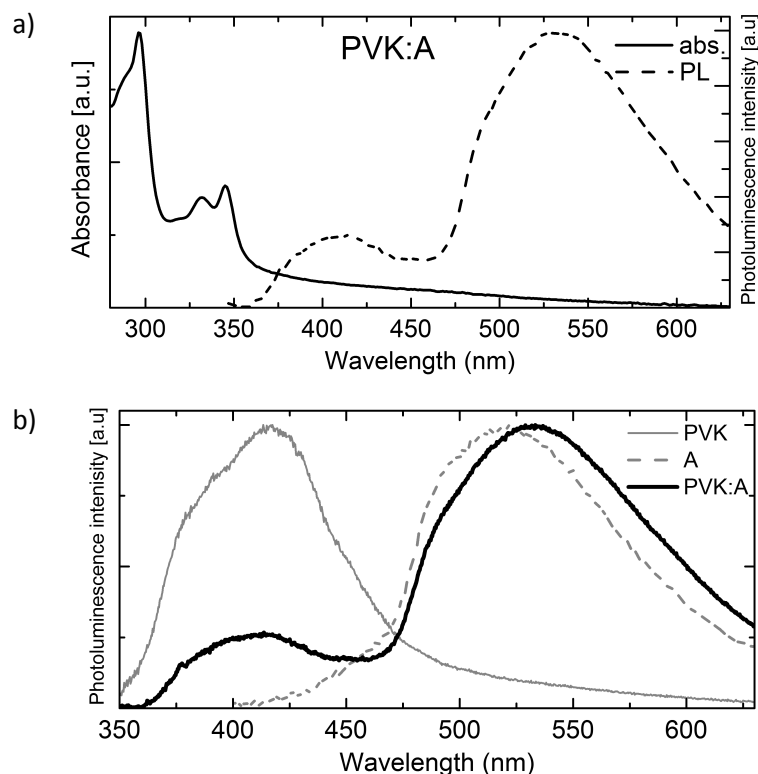


Figure 6-11 a) Absorption and PL (dashed line) spectra of A:PVK. 25 wt. % of A in PVK and overall concentration of 1 wt.% in CB. b) Comparison between the PL of PVK (grey line), A (grey dashed line) and PVK:A (black line)

In the ideal case, the singlet (triplet) energy level of the host should be higher than that of the guest. In the case of the singlet (triplet) energy level of the host lower than that of the dopant, no Förster energy transfer from the host to the metal complex would take place and consequently no emission from the dopant would be observed on the PL spectra. Furthermore, in the case of an ideal singlet energy levels position but with the triplet level of the host lower than that of the guest, a back transfer of the exciton to the host via Dexter transfer could take place, and luminescence from the metal complex would be very low [169].

We can see in Figure 5-11 that when PVK and A are mixed, the emission principally comes from A with a small peak around 420 nm assigned to PVK. Therefore, we can conclude that there is no substantial back transfer from the guest to the host via Dexter energy transfer and that Förster energy transfer from the host to the guest seems to take place.

Furthermore, we observed a red-shift of the PL emission from A to the blend PVK:A of 12 nm (0.05 eV) that could indicate the formation of an exciplex at the interface PVK/A.

The photoluminescence decay of the PVK:A blend was measured (see Figure 6-12). If fitted with a single exponential decay the lifetime is $3.9 \mu\text{s}$, whereas if fitted with a biexponential decay the lifetime are $1.14 \mu\text{s}$ and $10 \mu\text{s}$ (see Table 6-9). Comparing this result with the lifetimes of PVK and A separately, a new species, possibly a triplet exciplex [170], with a lifetime of $1.14 \mu\text{s}$ seems to be formed.

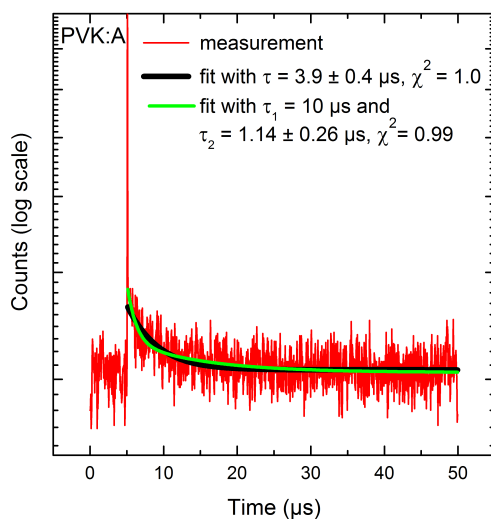


Figure 6-12 Time resolved photoluminescence spectra with a pulsed laser beam at 371 nm entering from the polymer side.

Table 6-9 Summary of the photophysical data of A:PVK.

	Absorption	Photoluminescence	Lifetime
A 25 wt.% in PVK (CB)	296 nm 332 nm 345 nm	415 nm 532 nm	(535 nm, 50 μs) $\tau_1: 3.9 \pm 0.4 \mu\text{s}$ or $\tau_1: 1.14 \pm 0.26 \mu\text{s}$ (19.4%) $\tau_2: 10 \mu\text{s}$ (80.6%)

6.3.2 Summary on the photophysics of PVK, A and PVK:A

PVK has a maximum of photoluminescence (PL) intensity at 416 nm (with a shoulder at around 380 nm) followed by a rather long tail with emission at wavelengths over 520 nm. PVK shows a biexponential decay with $\tau_1 = 0.67$ ns and $\tau_2 = 22.7$ ns. Emission from states with the latter lifetime has the higher contribution (82 %) to the emission. Therefore, this lifetime of 22.7 ns can be used to determine if emission from PVK is occurring or not when the triplet emitter A is added to the host layer of PVK. The biexponential decay for PVK was reported in the literature and was attributed to two excimer/dimer states with different lifetimes and peak emissions at around 380 and 430 nm [110, 120, 125, 126, 171].

The compound A emits at 520 nm with a biexponential decay. The shorter lifetime is so short that we cannot measure it with our setup. The majority of emission comes from a decay with a lifetime of 10 μ s (see Figure 6-10). A blend of PVK:A on the other hand emits with a bi- or tri-exponential decay. The smallest lifetime is again too small to be measured accurately with our setup. Fitting the decay with a monoexponential decay results in a lifetime of 3.9 μ s. Fitting it with a biexponential decay with one lifetime fixed at 10 μ s results in $\tau_1 = 10$ μ s and $\tau_2 = 1.14$ μ s (see Figure 6-12).

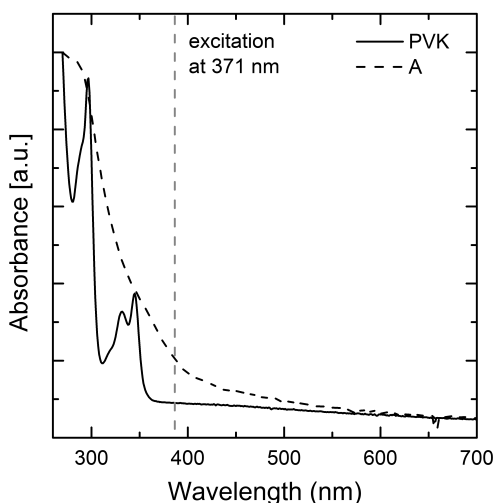


Figure 6-13 Absorption spectra of PVK and A. The excitation wavelength of 371 nm used for the lifetime measurements is indicated in grey.

There is no indication of emission from a state with a lifetime of 22.7 ns. Therefore, one may conclude that there is, indeed, negligible emission from PVK at 535 nm. However, one also needs to take into account the different absorption of PVK and A at the excitation wavelength of 371 nm (see Figure 6-13). PVK absorbs much less strongly so that only A might be effectively excited.

The same experiment with a higher energy laser would thus be needed to confirm the experiments. However, the 12 nm shift between the PL of A and PVK:A together with the formation of a new population with a lifetime of 1.14 μ s suggest the formation of an exciplex at the interface PVK/A.

6.4 Conclusion

The copper complexes investigated in this report are promising materials for application in phosphorescent OLEDs. They are based on cheap and non-toxic copper molecules and exhibit good characteristics.

Indeed, EQEs as high as 1.21 % have been demonstrated with compound G and luminances as high as 250 $\text{cd}\cdot\text{m}^{-2}$ with compound A. Compounds A, C, E and G show good charge and energy transfer from PVK to triplets contrary to B and D. These results were foreseen since B and D triplet levels are not in an ideal configuration if we compare them with the one of PVK and its dimer emission. Due to very broad emission spectra the colour of all devices are in the yellow/orange range and not in the blue or green region as it could have been expected from the photoluminescence spectra of the compounds. The photophysical measurements performed on A and PVK:A suggests the formation of a triplet exciplex. However, the experiment should be repeated with a higher energy laser to be confirmed.

Inserting a hole injection layer improves the overall characteristics of the devices leading to better current efficiencies, luminances and turn-on voltages. Furthermore, the emission of the interlayer (in this case TFB) contributes to the electroluminescence spectra leading to whiter light. However, the triplet energy level of TFB being below the ones of the copper complexes and PVK, it does not confine the triplet exciton within the

emissive layer. A more suitable hole injection layer may, thus, improve the devices even more. A good candidate might be TCTA since its triplet energy is reported at 2.7 eV [142].

It seems that the main difficulty in the making of solution-processable phosphorescent OLEDs with these copper complexes is the lack of good phosphorescent hosts available on the market with convenient triplet energy level and emission.

An alternative method for improving the charge carrier balance and shifting the recombination zone away from the cathode interface would be to use a copolymer incorporating an electron-transporting moiety in its backbone. The density of minority charge carriers would increase and consequently the charge carrier balance improve. This method is preferred since it enables higher current densities and, therefore, higher luminances at lower voltages. Furthermore, this approach would avoid the deposition of the electron-transporting layer and hence suppress a time-consuming and expensive step. However, these kinds of polymers are difficult to obtain.

7 On the importance of the solvent for phosphorescent OLEDs based on Cu-complexes

It is well-known that by changing experimental parameters such as the solvent, the thickness of the film and the annealing steps it is possible to tune the photophysics and the performance of devices made of organic materials.

When choosing a solvent for making polymer films, one needs to opt for one that sufficiently dissolves the polymer and the dopant, does not react with or introduce impurities, and produces a pinhole-free thin film on the substrate. PVK is soluble in most of the common organic solvents [169].

In solution of high enough concentration, polymer chains tend to interpenetrate each other and thus form aggregates. Aggregates are not only concentration dependent but solvent dependent as well [25]. It was reported that aromatic solvents such as chlorobenzene (CB) have a preferential interaction with the aromatic part of the polymer chain and that non-aromatic solvents such as tetrahydrofuran (THF), on the other hand, have a preferential interaction with the polymer's non-aromatic groups influencing the aggregation of the polymers [42, 172]. It is believed that these conformational differences in solutions are preserved and survive into the film influencing the morphology and photophysics of the resulting films [25, 173].

The effect of the solvent on PVK devices was partially studied by Vaeth et al. [169], Qiang et al. [111] and Alonso et al. [40]. The solvent used to make the polymeric solution would have an influence on the device performances by tuning the molecular conformation of PVK (see part 5.1.1). In this chapter, PVK was used in two different solvents in order to compare their influence on the characteristics of the devices.

Experimental details:

PVK was purchased from Sigma-Aldrich (Mw: 1, 100 000 g.mol⁻¹). Chlorobenzene and tetrahydrofuran were purchased from Sigma Aldrich and the solutions were done in air.

Substrates were rinsed with acetone and then cleaned successively in acetone and isopropanol in the ultrasonic bath for 15 minutes.

The ITO was oxygen plasma treated for 10 minutes immediately prior to the spin-coating of the PEDOT:PSS, which was then baked at 180°C for 10 minutes on a hot plate.

The active layer consisted of either a pure polymer (PVK) or a blend of PVK with G (see part 6.1). These were spin-coated in nitrogen atmosphere from 1 % by weight solutions of the polymer or blends in CB or THF. The thickness of these films is around 80 nm.

TPBi (30 nm), Ca (30 nm) and Al (150 nm) were thermally evaporated on top of the active layer at $\sim 10^{-6}$ mBar.

7.1 Preliminary experiments

7.1.1 Influence of the solvent on the absorption spectra of PVK

Firstly the absorption spectra of PVK spin-coated from CB and THF were compared (see Figure 7-1). Very small differences at low wavelengths were observed indicating that there is no difference in their ground state interactions.

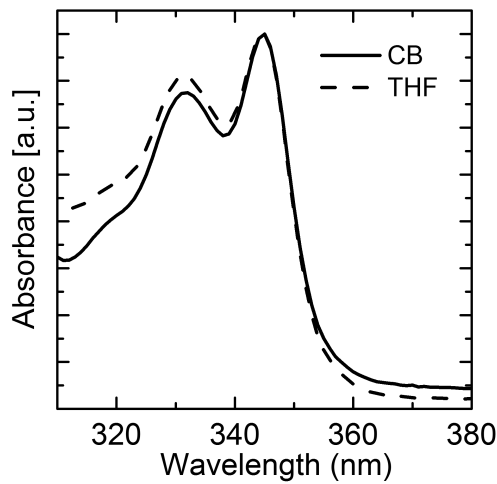


Figure 7-1 Absorption spectra of 1 wt. % PVK in CB and in THF measured from thin film.

7.1.2 Influence of the solvent on pure PVK devices

Devices with the structure: ITO/PEDOT:PSS/PVK/Ca/Al were made with PVK spin-coated from THF and CB. The comparison between the EL spectra is shown in Figure 7-2.

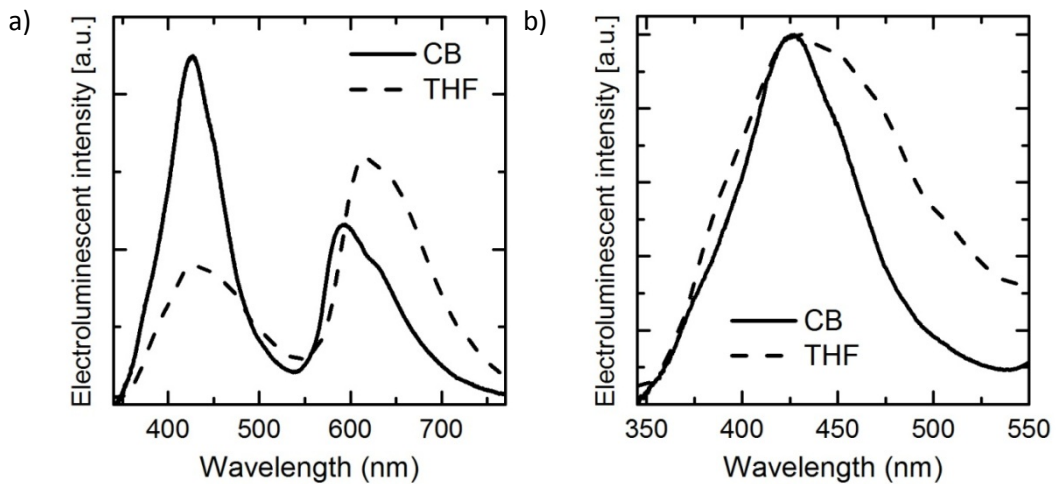


Figure 7-2 Comparison between the electroluminescence spectra of PVK in CB (plain line) and in THF (dashed line) normalised a) on the integral b) on the maximum of the first emission peak.

As seen in part 5.1.1, the EL spectrum of PVK presents two major peaks that were attributed to different molecular conformations of PVK: face-to-face (~430 nm) and side-by-side (~380 nm). In addition, an emission peak at about 600 nm is commonly observed

in electroluminescence from PVK. This 600 nm peak was attributed to a triplet excimer [111] or to impurities/chemical reaction products [120].

Hence the EL spectra depicted in Figure 7-2 would indicate that the films spin-coated from THF have more side-by-side conformation than the films spin-coated from CB. Indeed, chlorobenzene interacts with the aromatic carbazole group, leading to more face-to-face configuration where there is π -electron overlap between neighbouring carbazole groups and, therefore, better transport properties. On the contrary, THF interacts with the non-aromatic backbone of PVK maximizing the side-by-side conformation of PVK.

The difference in the relative intensity of the two principal peaks might be due to a difference of the thickness of the films [40]. Moreover, the 25 nm red-shift of the second EL peak observed for the THF solution could be due to different molecular conformations [111] or the sign of the presence of aggregates.

The performances of the devices are summarized in Table 7-1. The devices in THF present lower EQEs, higher turn-on voltages and similar luminances. According to Heeger et al. [86] the efficiency of films depends on the thickness of the films and films below 100 nm are even more sensitive because of quenching by the cathode. The thicknesses of the layers were measured and were about 80 nm, however, a slight difference can lead to a real difference in efficiencies. Better performances in CB than THF were already reported for MEH-PPV by A. Monkman [61] and T.-Q. Nguyen [42].

Table 7-1 Summary of the properties of the ITO/PEDOT:PSS/PVK/Ca/Al devices in average for PVK spin-coated from CB and THF solutions.

	Max EQE (%)	Light turn on voltage (V)	Efficiency (@10 mA.cm ⁻²) (cd.A ⁻¹)	Max luminance (@114 mA.cm ⁻²) (cd.m ⁻²)
PVK - CB	0.02 ± 0.02	6.2 ± 1.0	0.007 ± 0.009	2.2 ± 1.3
PVK - THF	0.01 ± 0.01	8.4 ± 2.9	0.007 ± 0.008	2.2 ± 1.4

Furthermore, it is well known that the thickness of the film has an influence on the turn-on voltage of devices being higher for higher thicknesses [40, 174]. But the fact that CB interacts more with the carbazole units than the backbone might also mean that the carbazole groups have the tendency to face outside leading to a better electrical contact with the anode and better charge injection [25]. On the contrary, when PVK is spin-

coated from THF, it is the non-conjugated backbone that might face outside leading to a poor electrical contact with the anode (see Figure 5-2) and, therefore, higher turn-on voltages and lower injection currents (see Figure 7-3) [173].

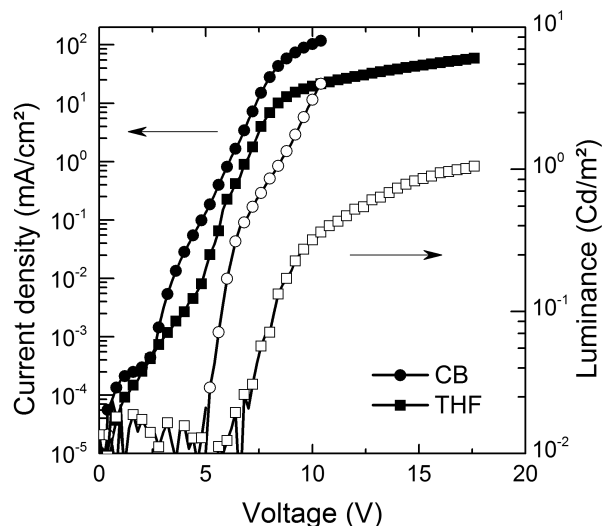


Figure 7-3 Current density (filled symbols) and luminance (empty symbols) of the devices ITO/PEDOT:PSS/PVK/Ca/Al spin-coated from chlorobenzene (circles) and from THF (squares).

From Figure 7-3 it is observed that the CB devices show higher injection currents than the THF devices. The difference in the injection current density was also observed by Liu et al. [25] for MEH-PPV devices spin-coated from THF and dichlorobenzene (DCB). This could be due to at least three different reasons: (1) the morphology from the CB film might yield a better contact with the anode layer, (2) the polymer film spun from CB has higher carrier mobility than that of THF thin film or (3) the barrier for electron/hole injection is lower for CB devices.

As discussed previously, this could be due the fact that in CB the carbazole groups have the tendency to face outside and are thus arranged around the non-conjugated polymer backbone that would, therefore, be hidden inside. This arrangement of the polymer would lead to a better electrical contact with the anode and thus better charge injection and also a better charge transport because the charge carriers could hop from carbazole groups to carbazole groups more easily.

The devices were investigated by atomic force microscopy (see Figure 7-4) with the help of Marten Tolk at UCL. As it can be seen on the snapshot, the general aspect of the thin film spin-coated from THF seems rough and affected by phase segregation whereas

the thin films spin-coated from CB are smooth. However, when measured on a 1 μm scale, the surface roughness (root mean square) of the films from CB and THF are 0.37 nm and 0.34 nm, respectively, and thus comparable.

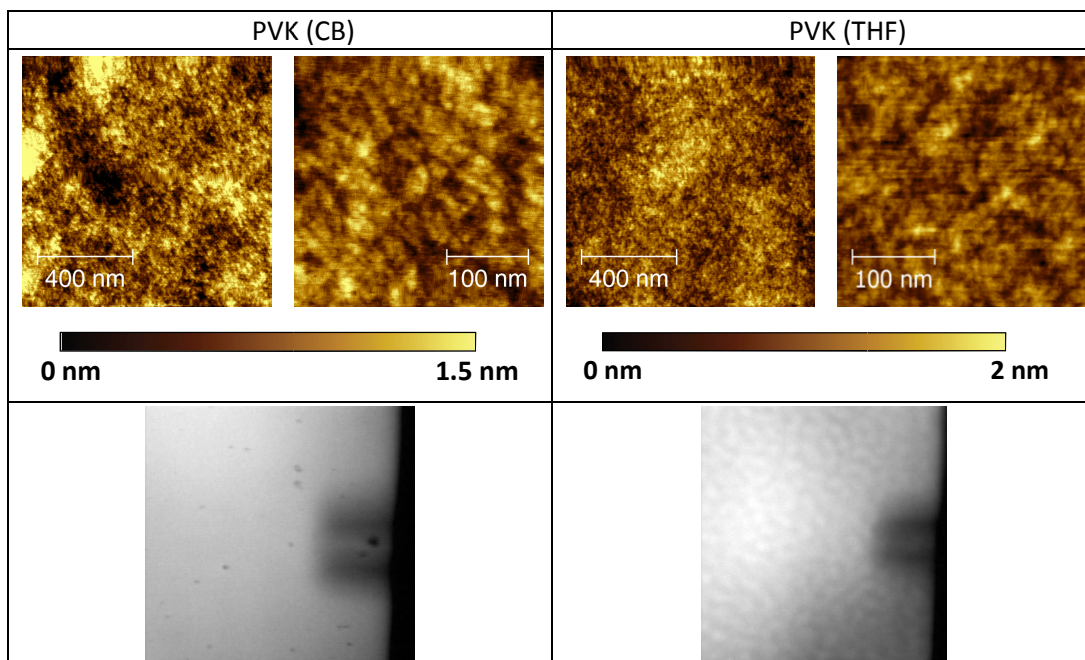


Figure 7-4 Atomic force microscopy of PVK spin-coated from CB (left) and from THF (right) on ITO substrates covered with an 80 nm thick PEDOT:PSS layer and snapshots of the electrodes (bottom row).

7.1.3 Influence of the solvent on PVK/TPBi devices

Devices with the structure: ITO/PEDOT:PSS/PVK/TPBi/Ca/Al were made with PVK in CB and in THF. Their EL spectra are shown in Figure 7-5.

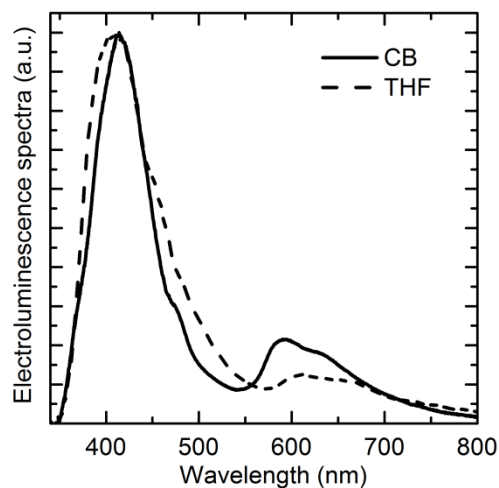


Figure 7-5 Comparison between the electroluminescence spectra of PVK/TPBi with PVK spin-coated from CB (plain line) and THF (dashed line).

Once again the difference in the relative intensity of the two peaks might be due to a difference of the thickness of the films [40], however, the peak in the 600 nm area seems to be more preminent when films are spin-coated from CB.

We can clearly see an enhanced emission at 380 nm when the film is spin-coated from THF that is not observed for the film spin-coated from CB, confirming the hypothesis of a higher ratio of side-by-side conformation in THF than in CB. Additionally we observe a red-shift of the spectra in THF compared to the one in CB mostly on the peak at 610 nm. This could be due to more interchain interactions in THF than CB, explaining this red-shift and the overall broadening of the EL spectra.

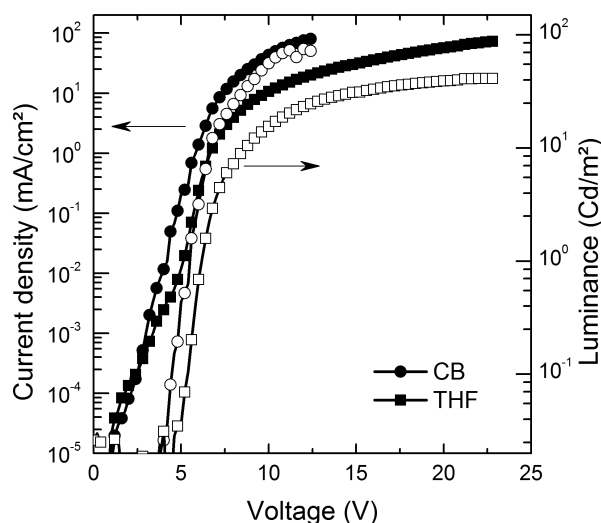


Figure 7-6 Current density (filled symbols) and luminance (empty symbols) of the ITO/PEDOT:PSS/PVK/TPBi/Ca/Al devices spin-coated from CB (circles) and from THF (squares).

Table 7-2 Summary of the properties of the ITO/PEDOT:PSS/PVK/TPBi/Ca/Al devices in average for PVK spin-coated from CB and THF solutions.

	Max EQE (%)	Light turn on voltage (V)	Efficiency (@10 mA.cm ⁻²) (cd.A ⁻¹)	Max luminance (@114 mA.cm ⁻²) (cd.m ⁻²)
PVK/TPBi - CB	0.25 ± 0.12	4.8 ± 1.8	0.19 ± 0.03	92 ± 109
PVK/TPBi - THF	0.29 ± 0.05	5.6 ± 1.1	0.17 ± 0.01	39 ± 10

Once again the current densities in the devices made from THF were lower than that of CB despite the addition of TPBi. The turn-on voltages were higher for devices spin-coated from THF than from CB. As discussed previously, this difference could come from a higher thickness of the THF film [61] and from the difference of configuration of PVK in the different solvents. Furthermore, the EQE was this time higher in THF but the luminance was lower.

7.2 Influence of the solvent on the phosphorescent OLEDs

The copper complex G was blended with PVK and devices were fabricated with a TPBi interlayer on top.

Devices made from chlorobenzene exhibited good overall characteristics (see part. 6.2.4) whereas no light could be obtained from the devices made from THF.

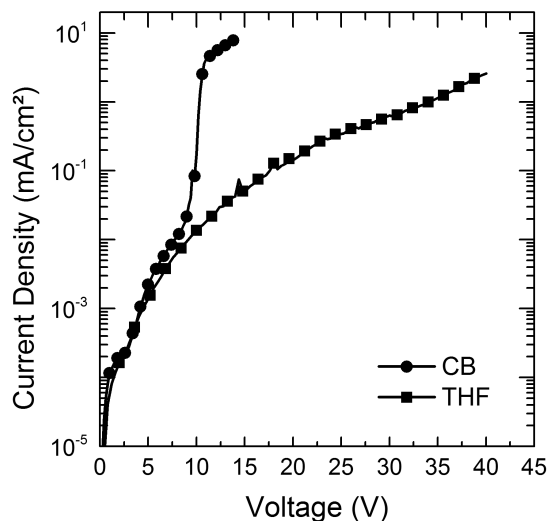


Figure 7-7 Comparison of the current density of PVK:G 25 wt. % spin-coated from CB (circles) and from THF (squares).

Figure 7-7 shows the comparison between the current density of devices spin-coated from CB and THF. In an attempt to understand why the devices made from CB exhibits good characteristics whereas no working devices could be made from THF, atomic force microscopy was performed on the samples with the help of Marten Tolk.

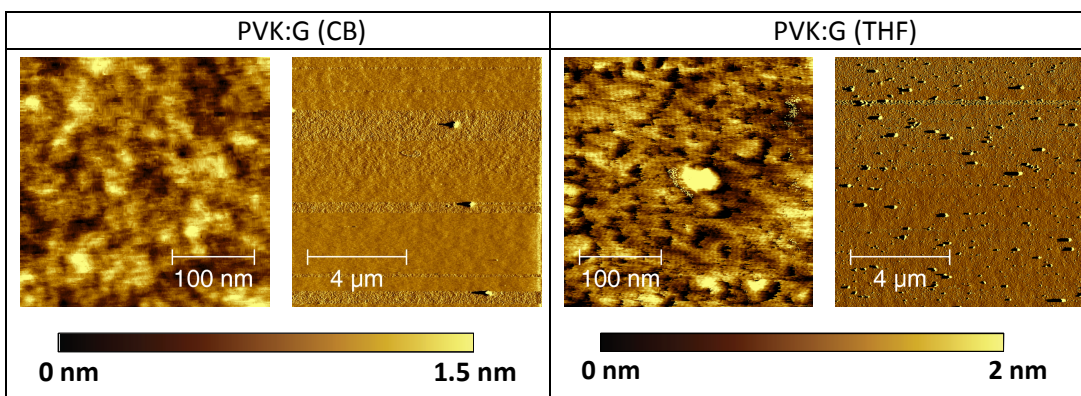


Figure 7-8 Atomic force microscopy of PVK:G spin-coated from CB (left) and from THF (right) on ITO substrate covered with a 80 nm thick PEDOT:PSS layer. The images with the 4 μm scale bar show the amplitude of the vibrating AFM probe (not the topography).

It is clear that there were more clusters in the devices made from THF than CB. The surface roughness was 0.28 nm for the CB samples and 1.03 nm (0.37 nm without the high clusters) for the THF ones. Thus, CB seems to be a better solvent for G than THF, resulting in a better dissolution and minimizing the formation of clusters.

The snapshots of the electrodes (Figure 7-9) show the presence of “craters” on the electrodes. This phenomenon was already observed by several groups [175-177] on polymeric devices.

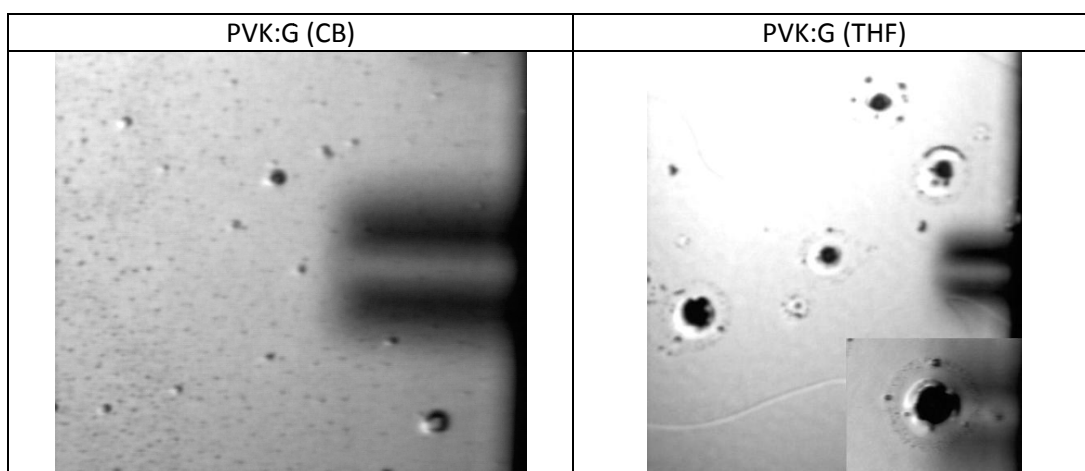


Figure 7-9 Snapshots of the electrodes on films of PVK:G spin-coated from CB (left) and THF (right).

Scott et al. [175] attributed these craters to the presence of localised electrical shorts where a rather large fraction of the current passes through a small area explaining a reduced current in the rest of the diode. However, Kim et al. [178] demonstrated that the black spots formation was associated with cathode pinhole defects and could be formed on top of both ITO and glass. By using in-situ Raman spectroscopy they showed that the non-emissive disk surrounding the pinhole (as seen in Figure 7-9) is composed of locally reduced PEDOT while the electroluminescent polymer is not affected. From their experiments they conclude that pinholes are formed on particles during the metal evaporation introducing a pathway for the diffusion of moisture and oxygen that will then electrochemically react with PEDOT:PSS.

If we also consider that THF is well-known to be miscible with water (BHT is typically used as a stabilizer in THF, however, the THF used in this experiment did not contain any inhibitor) and that the solution preparation was done in air. Oxygen might thus be

present in higher quantities in the solution made with THF than in the solution made from chlorobenzene.

The presence of more and bigger clusters in phosphorescent OLEDs made from THF due to aggregation of the triplet emitters together with a higher water and oxygen content of THF compared to CB might explain the formation of pinholes on the cathode and, therefore, the failure of the devices made from THF.

One way of resolving this issue might be to use THF handled only in inert atmosphere and to encapsulate the devices to prevent oxygen and moisture from entering the devices.

7.3 Conclusion

As seen in this chapter, the choice of the solvent is of tremendous importance when fabricating devices. It was demonstrated that in pure PVK devices, the performances in CB and THF are comparable except for the turn-on voltage which is higher in THF devices. That could be explained by several factors such as a difference in thickness (not proven by profilometry) but also a less good contact with the anode due to the side-by-side conformation.

When the copper complex G is introduced, the change of solvent has a crucial importance since the devices are efficient when spin-coated from CB but do not even emit a measurable light output when spin-coated from THF. The morphologic differences were observed by AFM and the presence of bigger clusters on THF films was shown. These clusters might lead to localised electrical short and/or create pinholes that allow moisture and oxygen to diffuse in the device and react with PEDOT-PSS leading to the failure of the devices.

PART III Near Infrared
OLED

Near-infrared and infrared OLEDs (700-2500 nm) have received growing attention over the last years because of their diverse potential applications such as optical communications, night vision readable displays, laser technology, sensors, wound healing and photodynamic therapy [167, 179-191].

However, achieving efficient near-infrared (NIR) emission is a challenging target due to the so-called energy gap rule which predicts that non-radiative decay rate increases exponentially with decreasing energy separation for a series of related excited states based on the same chromophore i.e. the quantum efficiency decreases with the energy gap [192-194].

Several classes of materials have been used to obtain NIR emission. The most common approach is to employ rare earth metal organic complex of lanthanides (Er^{3+} , Nd^{3+} , Tm^{3+} , Yb^{3+}) [195-211]. Lanthanide-containing materials have the advantage of featuring narrow-bandwidth emission in the near-infrared band (800 to 1600 nm) but have low photoluminescence efficiencies. For example Schanze et al. [212] reported EL EQE ranging from 8×10^{-4} to 2×10^{-4} % at $1 \text{ mA} \cdot \text{cm}^{-2}$ using Ln^{3+} in a porphyrin/polystyrene matrix and similarly O'Riordan et al. [213] obtained an EL EQE of 0.007 % at 1065 nm emission with a $\text{Nd}(\text{9-hydroxyphenalen-1-one})_3 \cdot 2\text{H}_2\text{O}$ complex based OLEDs. To date most EL performances obtained with Ln^{3+} complexes have EQE of less than 0.1 % making it, still, very challenging to develop efficient materials suitable for NIR emission.

The second class of materials is the transition metal complexes using phosphorescent emitters to achieve NIR emission [214-220]. One of the first group demonstrating this concept was Baldo et al. [221] with a platinum complex exhibiting 4 % EQE at 650 nm. Then, Williams et al. [222] used an iridium complex and obtained an efficiency of 0.1 % with a maximum emission at 720 nm, soon after Borek et al. [223] achieved 6.3 % EQE with platinumporphyrin compounds that emit at 769 nm and about 8 % EQE at 772 nm [224]. However, 772 nm is, still, far from the telecommunication window (1300 – 1500 nm) needed for some applications.

These two classes of materials being widely used for NIR emitters, some have had the idea to combine lanthanides and metal transition complexes together. Indeed, the use of strongly absorbing chromophores as sensitizers for the f-block emission of the lanthanides allows one to overcome the fact that the 4f-4f transitions of the lanthanide ions are forbidden and that their absorption is very weak [225, 226]. The first to report

such compounds are Klink et al. [227] where they sensitized Nd^{III} and Yb^{III} by ruthenium(II) tris(bipyridine) ([Ru(bpy)₃]²⁺) and ferrocene. Subsequently many d-block chromophores were studied [121, 228-233] and Chen et al. [225] reported an EQE of 0.3 % with a maximum radiance of 6.1 μW.cm⁻¹ at 1060 nm.

Finally the last class of materials contains the low band gap organic chromophores [234-238]; semi-conducting nanoparticles [239-243] and polymers [202, 244-251] with the emergence of acceptor-donor-acceptor (ADA) or donor-acceptor-donor (DAD) polymers [252, 253]. For example, Yang et al. reported D–A–D oligomers that displayed an EL spectrum peaking at 815 nm and an EQE of 1.6 % [254]. Furthermore, Qian et al. [255] reported a D-A-D type chromophores with an emission exclusively at 1080 nm and an EQE of 0.28 %.

The first chapter in this section focuses on NIR OLED incorporating a benzoselenadiazole copolymer blended in different hosts and leading to 0.21 % efficiency at 835 nm. Whereas in the second chapter near-infrared emission at 800 nm was observed from compounds originally emitting at 515 and 540 nm thanks to what is believed to be an exciplex.

8 OLEDs based on a benzoselenadiazole compound

The present chapter reports on the properties of organic light-emitting diodes, OLEDs, incorporating a polymer from the University of Wuppertal Poly[4,4-bis(2-ethylhexyl)-4H-cyclopenta[1,2-b:5,4-b']dithiophene-2,6-diyl-co-4,7-di(thiophen-2-yl)benzo[c][1,2,5]selenadiazole-4,7-diyl], TBST in short. The structure of this molecule is shown in Figure 8-1, and incorporates a benzoselenadiazole unit obtained by replacing the usual sulphur atom of a benzathiadiazol by a selenium atom. Because the selenium atom is bigger and more electron-rich than the sulphur atom, the substitution results in a lower energy-gap polymer with red-shifted emission [256]. TBST also incorporates a cyclopentadithiophene (CPDT) unit not dissimilar from a fluorene unit, where phenyl rings were replaced by thiophenes. In this structure the two thiophenes are forced to be essentially coplanar. This also extends the effective conjugated length of the polymer and again contributes to lowering the bandgap. The planar structure should facilitate carrier transfer between two conjugated main chains, thereby allowing good hole mobilities [257]. These two units are separated by thiophene spacers.

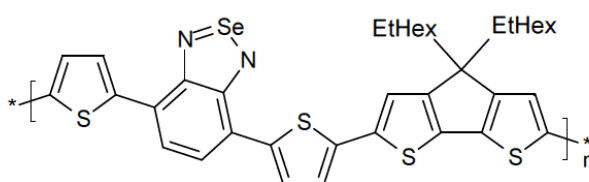


Figure 8-1 Chemical structure of TBST.

8.1 Experimental details

8.1.1 Materials

Two host materials were blended with TBST: poly[2-methoxy-5-(3',7'-dimethyloctyloxy)-1,4-phenylenevinylene] (MDMO-PPV) (Sigma-Aldrich) and poly[(9,9-dioctylfluorenyl-2,7-diyl)-alt-co-(1,4-benzo-{2,1',3}-thiadiazole)] (F8BT) (American Dye Source, M_w : 46,000 $\text{g}\cdot\text{mol}^{-1}$). In some devices a poly[(9,9-dioctylfluorenyl-2,7-diyl)-co-(4,4'-(N-(p-butylphenyl))diphenylamine)] (TFB) (American Dye Source, M_w : 68,000 $\text{g}\cdot\text{mol}^{-1}$) interlayer was used as well.

Ternary blends were made of TBST with F8BT (American Dye Source, M_w : 23,000 $\text{g}\cdot\text{mol}^{-1}$) and Poly(3-hexylthiophene-2,5-diyl) (P3HT) (Sigma-Aldrich – Plextronics, M_n : 30,000-60,000 $\text{g}\cdot\text{mol}^{-1}$).

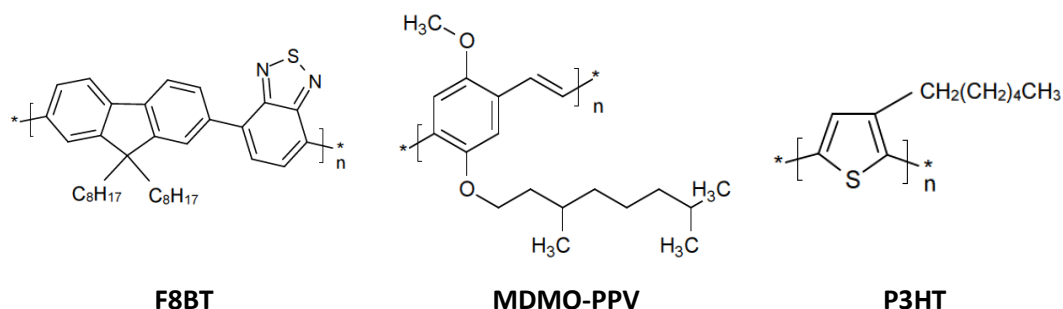


Figure 8-2 Chemical structure of F8BT, MDMO-PPV and P3HT.

The optical properties of TBST in solution are summarised in Table 8-1.

Table 8-1 Optical properties (from solution in CHCl_3) and polymer parameters for TBST (data from University of Wuppertal).

	Absorption peak positions (nm)	PL peak position (nm)	M_n (g/mol)	M_w (g/mol)	Polydispersity
TBST	353 456 671	816	10,300	20,000	1.94

8.1.2 Energy levels of the materials

The HOMO-LUMO levels of TBST were determined by cyclic voltammetry experiments carried out by Dietrich Breusov in the laboratory of Dr. Daren Caruana in the chemistry department of UCL according to part 3.7.4. These are plotted in Figure 8-4, Figure 8-11 and Figure 8-18.

8.1.3 Devices

Devices were made with the structure: ITO/PEDOT:PSS (80 nm)/active layer/Ca (30 nm)/Al (150 nm). The ITO was oxygen plasma treated for 10 minutes immediately prior to the spin-coating of the PEDOT:PSS, which was then baked at 180°C for 10 minutes on a hot plate.

The active layer consisted of either a pure polymer (F8BT, MDMO-PPV or TBST) or a blend with the NIR polymer. These were spin-coated in nitrogen atmosphere from 2 wt. % of the polymers/blends in toluene for F8BT devices and 1 wt. % for MDMO-PPV devices. The thicknesses of these films were around 100 nm.

8.2 Results

8.2.1 Pure material OLEDs

First of all the properties of the pure materials (F8BT, MDMO-PPV and TBST) were studied. Their absorption spectra are plotted alongside their electroluminescence and photoluminescence spectra in Figure 8-3.

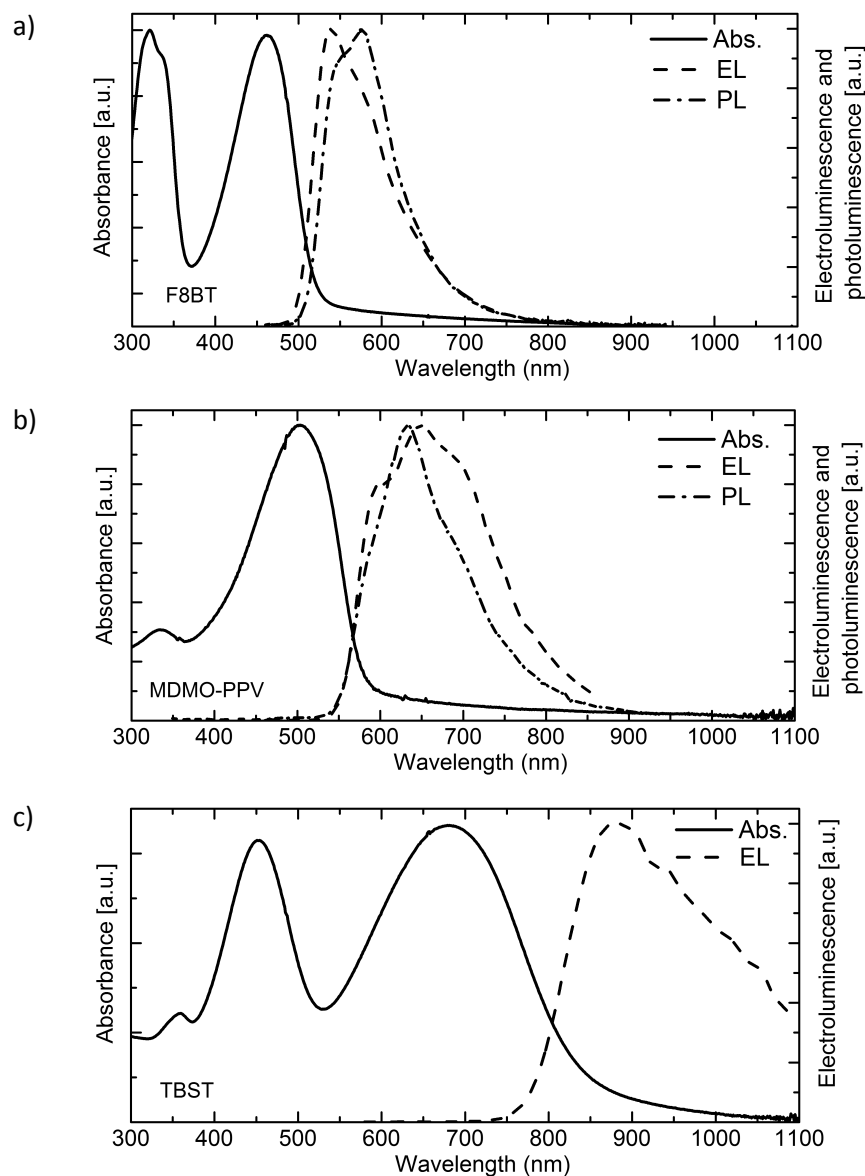


Figure 8-3 Absorption, Electroluminescence and Photoluminescence spectra (excitation at 325 nm for F8BT and 412 nm for MDMO-PPV) of thin films of a) F8BT, b) MDMO-PPV and c) TBST spin-coated from toluene.

F8BT is a green light-emitting copolymer (see Figure 8-2) widely used as a host with good electron and hole transport properties [258, 259]. The maximum absorption peak of F8BT is at 461 nm and corresponds to π - π^* transitions [260], its PL exhibits two main emission peaks at 550 and 580 nm. These values are in agreement with the literature [209, 258, 261-263].

MDMO-PPV is a red/orange copolymer with good hole transport properties that shows a maximum absorption peak at 503 nm, EL at 650 nm and PL at 633 nm [264-266].

As expected the electroluminescence spectra show that emission of TBST is coming from the near-infrared with a maximum emission peak at 880 nm and a maximum absorption peak at 680 nm.

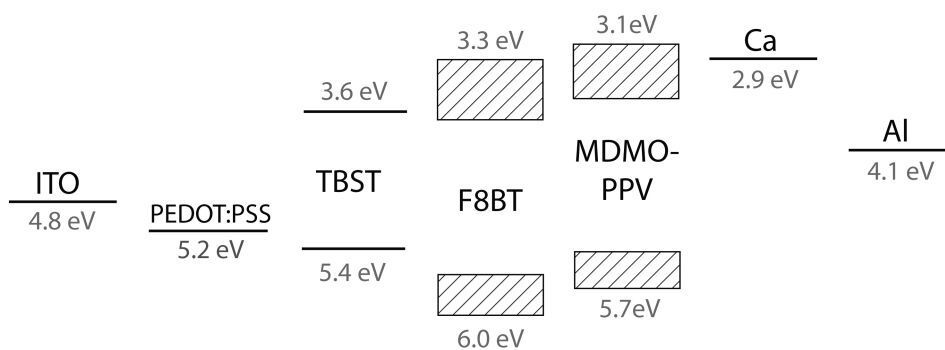


Figure 8-4 Energy diagram of the materials used in these experiments compared with the work functions of the electrodes. The HOMO and LUMO levels of TBST, F8BT and MDMO-PPV were determined by cyclic voltammetry at UCL as described in the text and in part 3.7.4. Other values are from literature [148]. The error on F8BT and MDMO-PPV values are represented.

All three materials have LUMOs lying below the Fermi level of calcium (2.9 eV, Figure 8-4), thus resulting in a pinning of the electrode Fermi level to the material's LUMO and allowing good electron injection. The HOMO level of F8BT (6.0 eV) is very deep and sits well below the Fermi level of the anode, that of TBST (5.4 eV) is just below the anode. Therefore, the fact that the light turn-on voltage of TBST was lower than F8BT (1.4 V and 2.9 V respectively) was, indeed, expected. MDMO-PPV has its HOMO lying at 5.7 eV, i.e. between F8BT and TBST, its light turn-on voltage is, indeed, located between that of TBST and F8BT (see Figure 8-5 and Table 8-2).

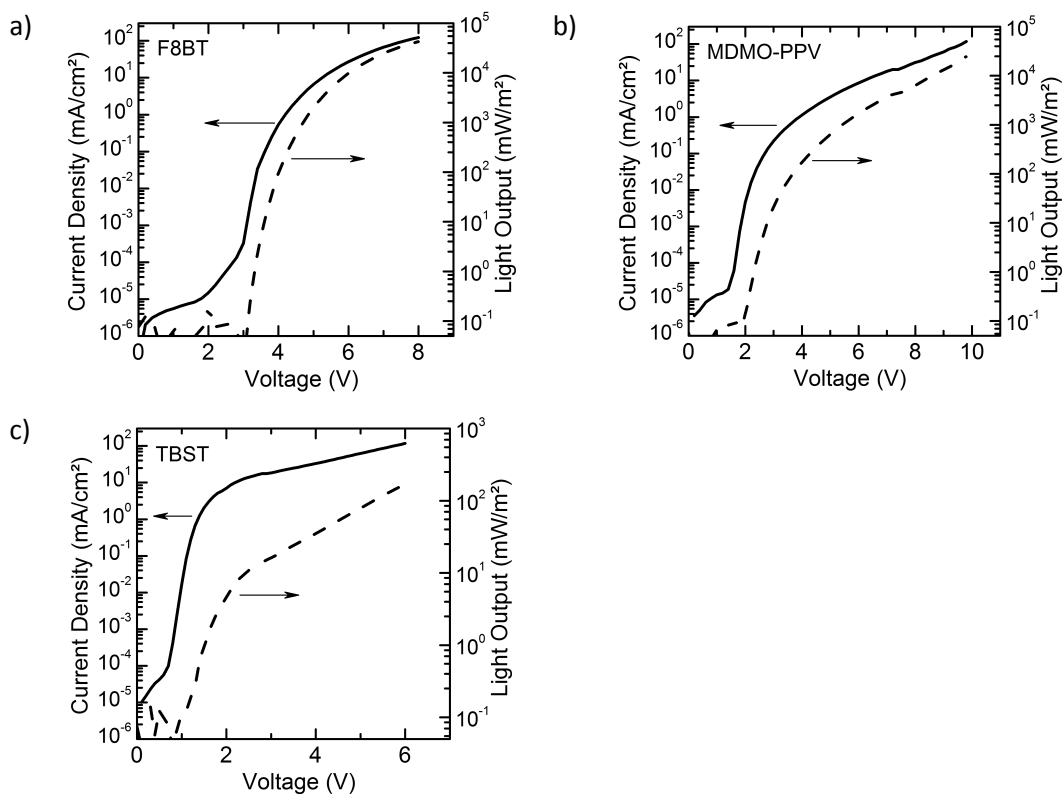


Figure 8-5 Current-voltage-light characteristics of pure material devices a) F8BT, b) MDMO-PPV and c) TBST.

It can be seen from Figure 8-5 and Table 8-2 that the maximum light output was given out by F8BT devices (35000 mW/m²) as one might expect given the known success of F8BT as a green emitting polymer for PLEDs. As expected from the energy gap rule, TBST gave out two hundred times less light power at 180 mW/m². This trend in the maximum light was reflected in the greater efficiencies with F8BT (1.51 %) than with MDMO-PPV (1.09 %) and TBST (0.012 %).

Table 8-2 A summary of the principle properties of the ITO/PEDOT:PSS/F8BT or MDMO-PPV or TBST/Ca/Al devices in average.

Polymer	Max. EQE (%)	Light turn-on voltage, V _{on} (V)@ 0.2 mW/m ²	Max. light output (mW/m ²) @ 114 mA/cm ²
F8BT	1.51 ± 0.25	2.89 ± 0.40	35000 ± 4000
MDMO-PPV	1.09 ± 0.10	2.02 ± 0.20	22700 ± 4000
TBST	0.012 ± 0.002	1.44 ± 0.15	180 ± 50

8.2.2 Blended active layer OLEDs

In order to enhance the emission from TBST, aggregation should be minimized and the energy transfer from a host to the NIR material via Förster energy transfer maximised. F8BT and MDMO-PPV were chosen as hosts since the HOMO and LUMO of TBST are falling within the HOMO-LUMO gap of F8BT and MDMO-PPV (see Figure 8-4), an ideal situation for charge and energy transfer from the host to the guest.

Furthermore, if we compare the absorption of TBST with the PL of F8BT and MDMO-PPV, the overlap between absorption and photoluminescence spectra is good enough to expect some Förster energy transfer from the hosts to the guest (see Figure 8-6).

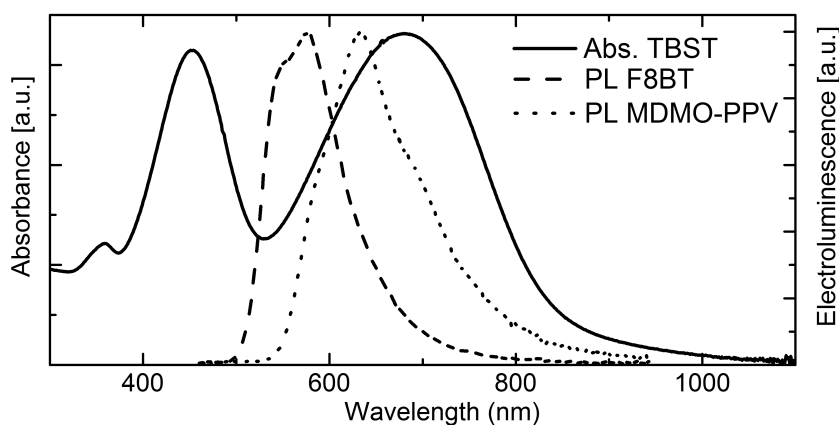


Figure 8-6 Absorption spectrum of TBST compared with the photoluminescence spectra of F8BT (dashed line) and MDMO-PPV (dotted line) in thin films spin-coated from toluene solutions.

Blended devices were made under the same processing conditions as the pure material devices (ITO/PEDOT:PSS/active layer/Ca/Al) but using an active layer of a blend of either F8BT or MDMO-PPV with the infra-red emitter TBST. Solutions were spin-coated from 2 wt. % in toluene for F8BT blends and 1 wt. % for MDMO-PPV blends.

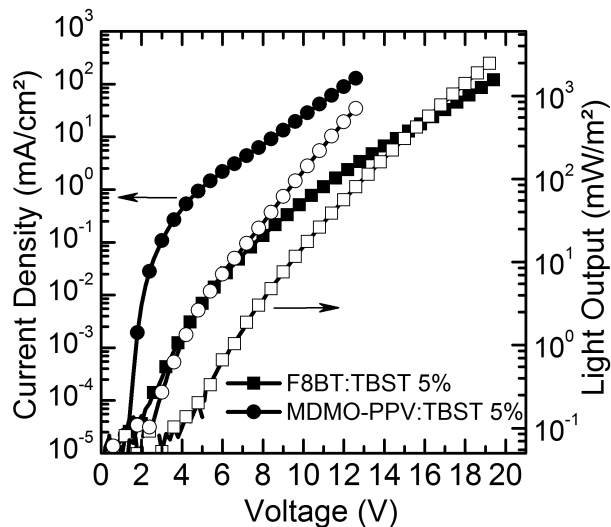


Figure 8-7 Current-voltage-light characteristics of blend devices: F8BT:TBST 5 wt. % (squares), MDMO-PPV:TBST 5 wt. % (circles). The current densities are represented by filled symbols and light outputs by empty symbols.

As we can see in Figure 8-7, when MDMO-PPV was the host, the currents were higher, the turn-on voltages lower and the maximum light outputs lower than with F8BT as a host.

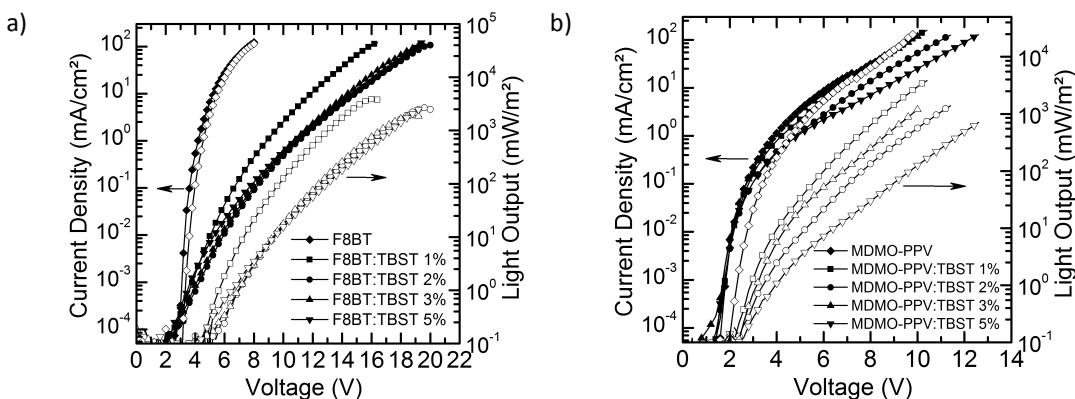


Figure 8-8 Current-voltage-light characteristics of blend devices a) F8BT:TBST and b) MDMO-PPV:TBST for the different concentrations of TBST (1, 2, 3 and 5 wt. %) compared to the pure material devices. The current densities are represented by filled symbols and light outputs by empty symbols.

In both cases, when TBST was added to the host, the current densities and light outputs decreased and the turn-on-voltages increased (Figure 8-8). When F8BT was the host the current densities and light outputs decreased until they stabilised. Indeed, the curves for 2, 3 and 5 wt. % are similar. On the contrary when MDMO-PPV was used as a

host the current densities and light outputs of the devices decreased with increasing concentration of TBST. Generally, in the case of charge trapping, the current-voltage characteristics would be dependent on the guest concentration whereas in case of energy transfer, the current-voltage characteristics are not sensitive to the variation of the guest concentration [116]. This hence indicates that charge trapping was occurring in the MDMO-PPV devices and would explain the lower efficiencies exhibited by the devices.

Table 8-3 Properties of the devices over a range of TBST compositions. The last column shows the percentage of emission of the materials in the different blends [F8BT (<650 nm), MDMO-PPV (<740 nm)].

	Concentration of TBST (wt.%)	Max EQE (%)	Light turn-on voltage V_{ON} (V) @ 0.2 mW/m ²	Max light Output (mW/m ²) @ (114 mA/cm ²)	Percentage of emission from TBST (%)
TBST	100 %	0.01 ± 0.01	1.44 ± 0.15	180 ± 50	100
F8BT	0 %	1.51 ± 0.25	2.9 ± 0.4	35000 ± 4000	0
	1 %	0.31 ± 0.01	4.7 ± 0.2	3900 ± 700	91.4
	2 %	0.23 ± 0.03	5.6 ± 0.3	2900 ± 300	96.7
	3 %	0.23 ± 0.02	5.2 ± 0.3	3000 ± 300	98.6
	5 %	0.20 ± 0.02	5.3 ± 0.3	2500 ± 100	99.5
MDMO-PPV	0 %	1.09 ± 0.10	2.0 ± 0.2	22700 ± 4000	0
	1 %	0.16 ± 0.02	2.4 ± 0.1	3000 ± 200	45.8
	2 %	0.08 ± 0.01	2.7 ± 0.2	1300 ± 60	74.2
	3 %	0.07 ± 0.01	2.6 ± 0.3	1100 ± 150	78.3
	5 %	0.04 ± 0.02	2.9 ± 0.1	600 ± 30	93

The properties of the devices depicted in Table 8-3 show significantly improved emission properties over the pure TBST devices. The maximum light output from F8BT:TBST 5 wt. % devices was 16 times greater than that of the pure TBST devices but 8 times lower than that of the pure F8BT devices.

In terms of efficiency, the F8BT:TBST blend performed better than the MDMO-PPV:TBST with EQEs reaching 0.31 % and 0.16 %, respectively. Maximum outputs were 3900 mW/m² and 3000 mW/m², respectively. The efficiency decreased with increasing concentration of TBST for both host materials but decreased a lot more for MDMO-PPV blends. The F8BT:TBST blend decreased by a factor of 1.6 when going

from the 1 wt.% to the 5 wt.% blend whereas the MDMO-PPV:TBST decreased by a factor of 4.2.

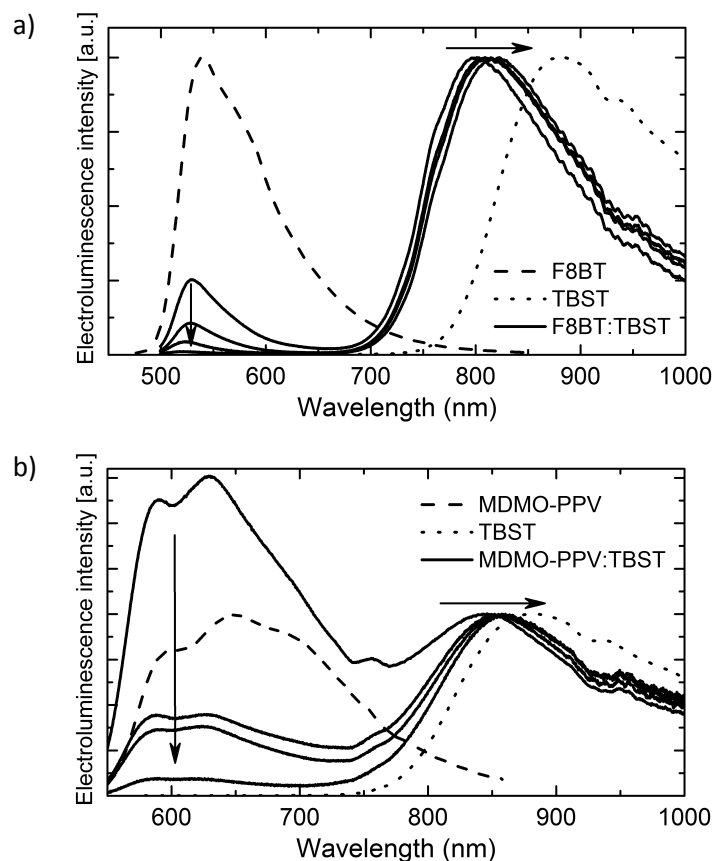


Figure 8-9 Effect of TBST concentration on the electroluminescence spectra of a) F8BT:TBST and b) MDMO-PPV:TBST with TBST concentration from 1 to 5 wt. %.

A clear change in the electroluminescence spectra as a function of TBST concentration was observed in the two systems studied (see Figure 8-9). The peak of TBST was shifted to the red with increasing concentration; this could be explained by the presence of intermolecular interactions and aggregate formation. Looking at the EL spectra, the average emission wavelength of F8BT:TBST in the infrared was at 810 nm whereas MDMO-PPV:TBST was at 855 nm. The fact that the emission of the blend MDMO-PPV:TBST was 45 nm-red-shifted could, at least partially, explain the fact that the devices made from MDMO-PPV were less efficient than the F8BT ones (according to the energy gap rule).

The MDMO-PPV devices showed lower efficiencies than the F8BT devices with 0.16 % instead of 0.31 % for 1 wt. % TBST and 0.04 % instead of 0.20 % for 5 wt. % TBST. The energy transfer from MDMO-PPV to TBST was less efficient than the energy transfer from F8BT to TBST, given that at 5 wt. % TBST, there was, still, 7 % of the emission coming from MDMO-PPV and only 0.5 % for F8BT devices.

Table 8-3 shows that only the F8BT:TBST 5 wt. % devices could be regarded as NIR emitter with 99.5 % of the light coming from TBST.

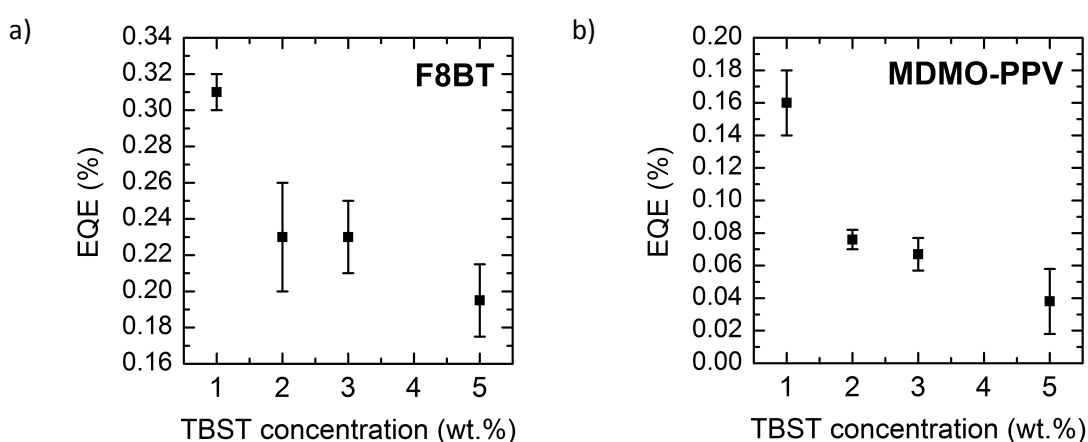


Figure 8-10 EQE plotted as a function of TBST for 1 wt. % to 5 wt. % TBST in a) F8BT and b) MDMO-PPV.

Looking at the EQEs of the devices (Figure 8-10), we observe that the EQE decreased with the concentration of TBST, independently of the choice of the host. It should be noticed that the EQEs were calculated over the entire UV-vis/NIR spectrum.

8.2.3 Effect of a TFB interlayer on F8BT devices

TFB is an interlayer spin-coated between the PEDOT:PSS layer and the active layer. It is believed to prevent the exciton quenching at the PEDOT:PSS interface and, therefore, improve the device efficiency [23]. It also acts as an electron blocking layer (see part 5.1.2 for more information).

TFB was spin-coated on top of PEDOT:PSS and baked at 180°C for 1 hour. The soluble part of TFB was then removed by spin-rinsing with toluene and a 10 to

20 nm-thick layer was obtained (measured by profilometry). The active layer was then spin-coated on top of it under the same processing conditions as in parts 8.2.1 and 8.2.2.

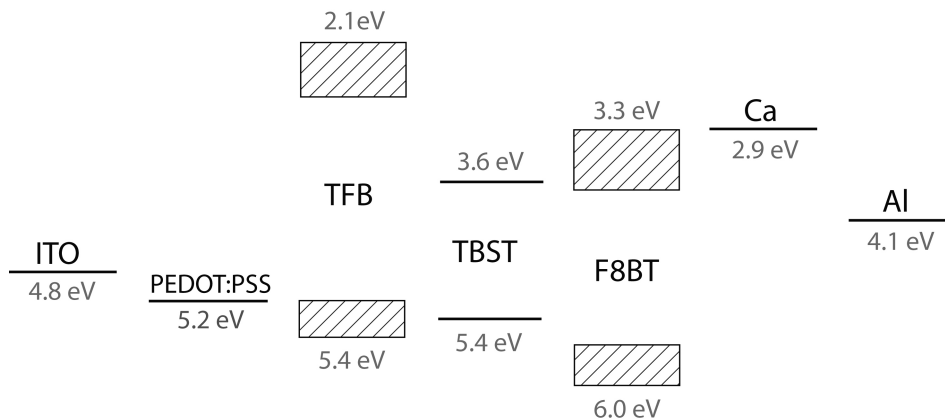


Figure 8-11 Energy diagram of the materials used in these experiments compared with the work functions of the electrodes. The HOMO and LUMO levels of TFB, TBST and F8BT were determined by cyclic voltammetry at UCL as described in the text or in part 3.7.4. Other values are from literature [148]. The error on TFB and F8BT values are represented.

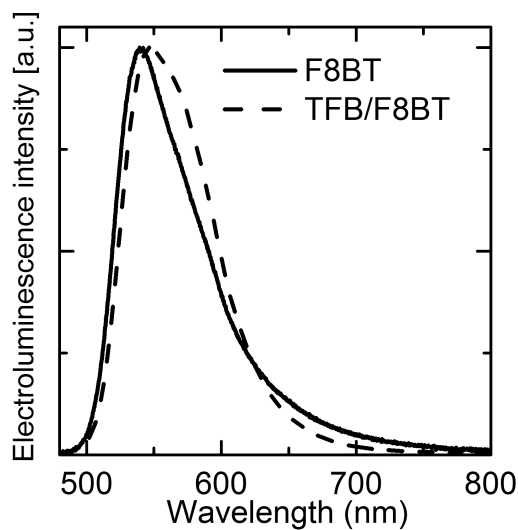


Figure 8-12 Comparison of the electroluminescence spectra of a F8BT device and a TFB/F8BT device.

As shown by the comparison of the EL spectra from F8BT and TFB/F8BT devices in Figure 8-12 the emission arose from F8BT. But the TFB/F8BT devices presented a shoulder and a shift in the EL spectrum attributed to the formation of an exciplex at the TFB/F8BT interface [23, 147, 267, 268].

The formation of an exciplex was checked with the help of Marten Tolks using the Time Correlated Single Photon Counting technique (TCSPC) as seen in Figure 8-13.

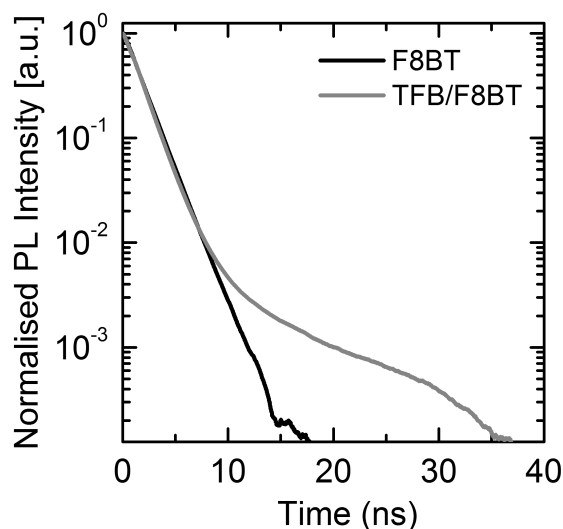


Figure 8-13 Time resolved photoluminescence spectra of F8BT and TFB/F8BT devices at 550 nm excited with a pulsed laser beam picked at 371 nm, of 270 ps duration entering from the polymer side.

The exciton lifetime (τ) values obtained by TCSPC measurements at a collection wavelength of 550 nm are summarized in Table 8-4. The lifetime of F8BT was almost constant over the whole energy range of emitted photons (1.85 eV to 2.25 eV, i.e. 670 nm to 550 nm). This shows no distinguishable difference between the different emissive states in terms of their decay time. At room temperature, the radiative emission from excited F8BT is characterised by a single decay constant. It is influenced by the distribution of the various distinctive emissive states of F8BT in the solid state [23] and the solid state excited lifetime was 1.6 ns in our case. When a TFB interlayer was added, two populations were observed. The first one had a lifetime of 1.3 ns and the second one of 5.8 ns. Whereas the first lifetime is attributed to F8BT, the longer one points toward an exciplex emission at the TFB/F8BT interface. Contrary to F8BT only devices, these values were not constant over the range of the emitted photon energy. Values of τ_1 were between 1.25 and 1.43 ns whereas the values of τ_2 were between 4.31 and 9.85 ns when the emitted photon energy varied from 1.85 eV to 2.25 eV (i.e. 670 nm to 550 nm). The dependence of the excited state lifetime on the emitted photon energy consolidates the assumption on the presence of low energy long lived interfacial excited states [23]. We also observed that when TFB was added, τ_1 was lower meaning that the excitons decayed faster. This could be due to an energy transfer from the excitons to the exciplex states [48].

Table 8-4 A summary of the principle properties of the ITO/PEDOT:PSS/TFB/F8BT/Ca/Al devices in average and compared to pure F8BT devices.

Polymer	Max. EQE (%)	Light turn-on voltage, V_{on} (V)@ 0.2 mW/m ²	Max. light output (mW/m ²) @ 4mA (114 mA/cm ²)	Lifetime (ns) at 550 nm
F8BT	1.51 ± 0.25	2.89 ± 0.40	35000 ± 4000	$\tau_1 = 1.6 \pm 0.05$
TFB/F8BT	1.34 ± 0.25	4.25 ± 0.4	32500 ± 3000	$\tau_1 = 1.3 \pm 0.05$ $\tau_2 = 5.8 \pm 0.05$

Nevertheless, the exciplexes generated by the introduction of a TFB interlayer did not improve the efficiencies of the devices as it would be normally expected (see Table 8-4: 1.34 % EQE instead of 1.51 % for pure F8BT devices). Kim et al. [23], for example, improved their F8BT devices from 0.3 % to 2.1 % by adding a TFB interlayer. In our case the quenching from PEDOT:PSS might have been already very low and, therefore, the system was not improved by adding a TFB interlayer. Furthermore, we also observed an increase in the light turn-on voltage, increasing from 2.9 V to 4.25 V. Additionally previous literature reported EQEs for ITO/PEDOT/F8BT/Ca/Al diodes of only 0.30 % [23] and 0.17 % [147], therefore, the surprising result is the very high efficiency of our ITO/PEDOT:PSS/F8BT/Ca/Al devices rather than the relatively modest performance of devices with a TFB interlayer which is comparable to the literature. We, thus, believe that it is due to the very high efficiency of the F8BT and the result of an optimized thickness.

In Figure 8-14 it is clear that the current densities at a given voltage were much lower when TFB was added. The lower currents could reflect a less efficient hole injection that was not expected from the HOMO-LUMO configuration (see Figure 8-11).

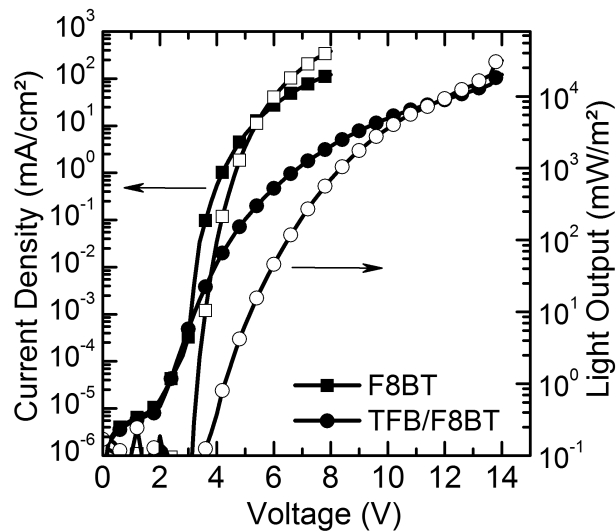


Figure 8-14 Current-voltage-light characteristics of TFB/F8BT devices (circles) compared to F8BT devices (squares). The current densities are represented by filled symbols and light outputs by empty symbols.

Blends of F8BT and TBST with a TFB interlayer were then fabricated. The current densities were very low resulting in low maximum outputs (Table 8-5). However, when a current density near $114 \text{ mA}\cdot\text{cm}^{-2}$ was reached, the maximum light output appeared to be comparable with the data obtained without the TFB interlayer, but the efficiency did not decrease with increasing concentration of TBST as much as without the TFB interlayer. The improved efficiency stability over TBST concentration could be due to a better confinement of the charge carriers within the emitting layer thanks to the electron blocking properties of TFB.

Table 8-5 Properties of the ITO/PEDOT:PSS/TFB/F8BT:TBST/Ca/Al devices over a range of TBST compositions. The last column shows the percentage of emission of the materials in the different blends [TFB F8BT (<670 nm)].

	Concentration of TBST (wt.%)	Max EQE (%)	Light turn-on voltage V_{ON} (V) @ $0.2 \text{ mW}/\text{m}^2$	Max light Output (mW/m^2) @ $114 \text{ mA}/\text{cm}^2$	Percentage of emission from TBST (%)
TFB F8BT	1%	0.23 ± 0.02	5.9 ± 0.3	1500 ± 500	61.8
	2%	0.22 ± 0.02	7.3 ± 1.2	760 ± 200	92.1
	3%	0.21 ± 0.02	6.5 ± 0.6	530 ± 270	96.4
	5%	0.21 ± 0.03	6.3 ± 0.8	1850 ± 620	99.5

The emission of F8BT for 1 wt. % TBST devices with a TFB interlayer was much higher than for F8BT single layer devices, but at 5 wt. the emission was the same with 99.5 % emission coming from TBST. In fact, F8BT and TFB/F8BT devices with 5 wt. % TBST were the only devices with a pure emission in the near infrared (99.5 %). In this case TFB/F8BT devices showed the best efficiency (0.21 %). Indeed, as we can see in Figure 8-15, the current densities and light outputs of F8BT:TBST 5 wt. % devices and TFB/F8BT:TBST 5 wt. % devices were very similar

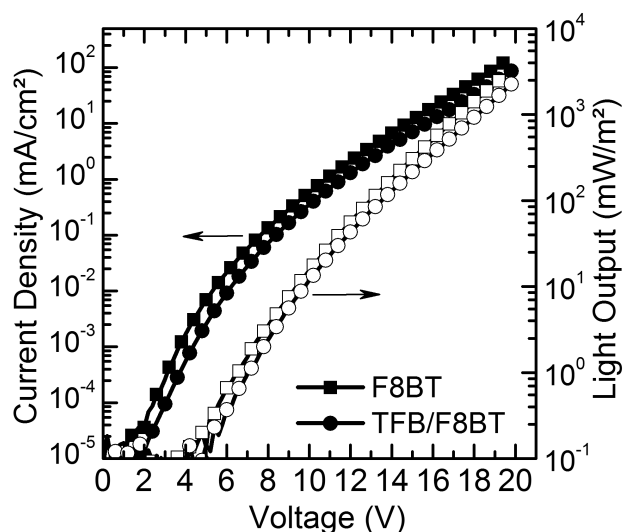


Figure 8-15 Current-voltage-light characteristics of TFB/F8BT:TBST 5 wt. % blend devices (circles) compared with F8BT:TBST 5 wt. % devices (squares). The current densities are represented by filled symbols and light outputs by empty symbols.

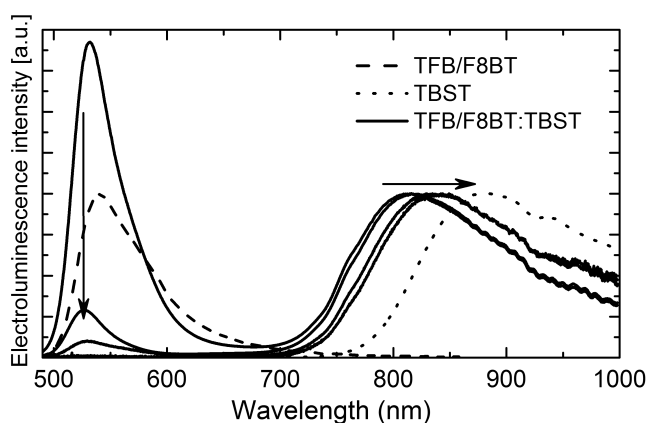


Figure 8-16 Effect of TBST concentration on the electroluminescence spectra of F8BT:TBST with a TFB interlayer.

Similarly to F8BT devices without a TFB interlayer, the peak of TBST was shifted to the red with increasing concentration (see Figure 8-16); this can be explained by the presence of intermolecular interactions and the formation of aggregates. The maximum EL peak for 5 wt. % was at 835 nm and thus 15 nm red-shifted compared to the single layer devices F8BT:TBST.

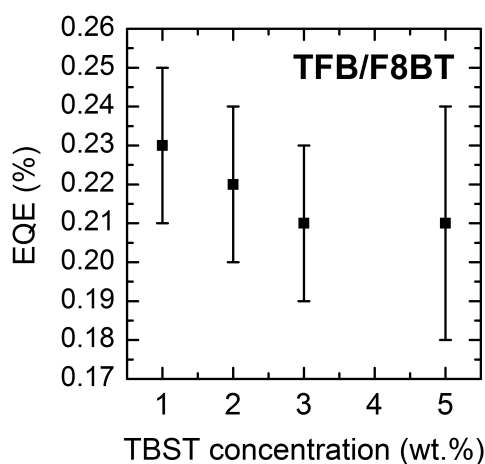


Figure 8-17 EQE plotted as a function of TBST concentration for 1 to 5 wt. % TBST

The EQE (%) versus TBST concentration for the TFB/F8BT devices is plotted in Figure 8-17 and shows that no obvious drop was observed in the efficiency contrary to F8BT single devices and MDMO-PPV devices. The TFB interlayer seems to limit the decrease in the efficiency occurring with the increase in the concentration of TBST.

8.2.4 F8BT:P3HT blend

Since red emission better matches with TBST absorption a novel approach consisting of the use of a ternary blend was used. F8BT and P3HT can be blended to obtain a red emission thanks to a favourable charge transfer and a relatively large Förster radius for energy transfer from F8BT to P3HT [269].

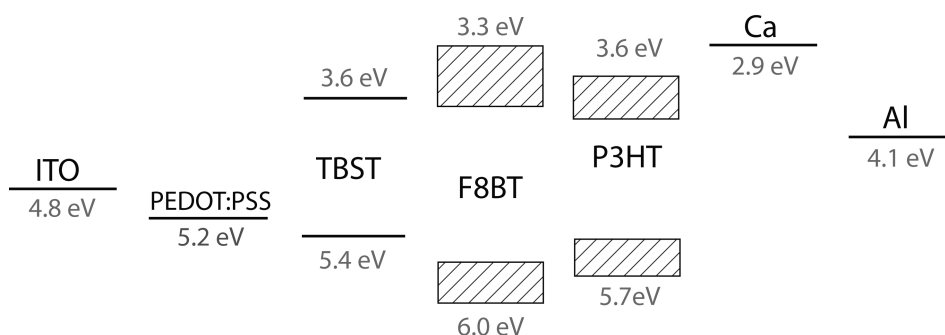


Figure 8-18 Energy diagram of the materials used in these experiments compared with the work functions of the electrodes. The HOMO and LUMO levels of TBST, F8BT and P3HT were determined by cyclic voltammetry at UCL as described in the text and in part 3.7. Other values are from literature [148]. The errors on F8BT and P3HT values are represented.

F8BT:P3HT blend devices with 5 wt. % P3HT in a 2 wt. % F8BT solution in p-xylene were fabricated. As we can see in Figure 8-19 there is a good charge or/energy transfer from F8BT to P3HT given that we could not see the emission from F8BT any longer with only 5 wt. % P3HT.

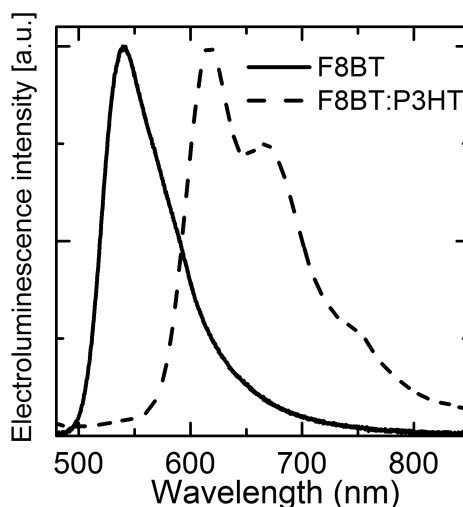


Figure 8-19 EL spectra of a F8BT:P3HT 5 wt. % blend compared with pure F8BT.

Table 8-6 A summary of the main properties of the ITO/PEDOT:PSS/F8BT:P3HT 5 wt. %/Ca/Al devices in average.

Polymer	Max. EQE (%)	Light turn-on voltage, V_{on} (V) @ 0.2 mW/m^2	Max. light output (mW/m^2) @ 114 mA/cm^2
F8BT:P3HT 5 wt %	1.70 ± 0.20	2.1 ± 0.2	25000 ± 7100

F8BT:P3HT 5 wt. % blends showed good efficiencies (1.69 % EQE) with an emission in the red (peak at 617 nm) and a light turn-on voltage of 2.1V (see Table 8-6).

Blends of F8BT:P3HT 5 wt. % and TBST were fabricated. The results are presented in Table 8-7.

Table 8-7 Properties of the ITO/PEDOT:PSS/F8BT:P3HT:TBST/Ca/Al devices over a range of TBST compositions. The last column shows the percentage of emission of the materials in the different blends [F8BT:P3HT 5 wt. % (<710 nm) (<720 nm for 1 wt. % TBST)].

Concentration of TBST (wt.%)	Max EQE (%)	Light turn-on voltage V_{ON} (V) @ 0.2 mW/m ²	Max light Output (mW/m ²) @ 114 mA/cm ²	Percentage of emission from TBST (%)
1%	0.16 ± 0.02	2.2 ± 0.1	2750 ± 200	45.9
2%	0.14 ± 0.02	2.3 ± 0.1	2100 ± 90	71.2
5%	0.09 ± 0.01	2.4 ± 0.1	1400 ± 90	95
10%	0.08 ± 0.01	1.8 ± 0.1	1160 ± 80	98.6

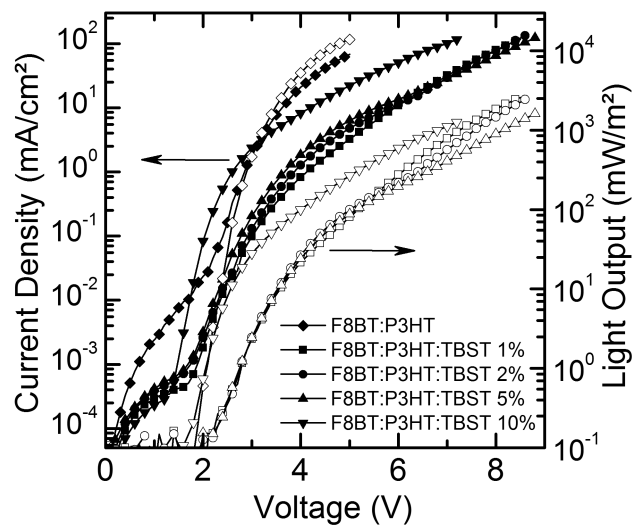


Figure 8-20 Current-voltage-light characteristics of F8BT:P3HT 5 wt. % :TBST 0, 1, 2, 5 and 10 wt. % blend devices. The current densities are represented by filled symbols and light outputs by empty symbols.

As we can see in Figure 8-20, the current densities in the devices were increasing with TBST concentration.

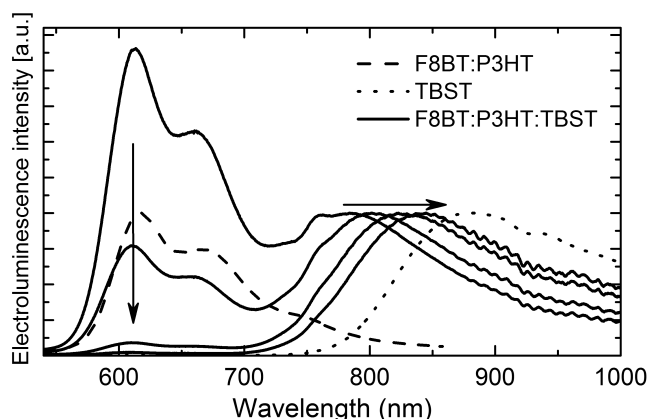


Figure 8-21 Effect of TBST concentration on the electroluminescence spectra of F8BT:P3HT 5 wt. %.

Figure 8-21 and Table 8-7 shows that with 1 wt. % TBST, the emission was mostly coming from the F8BT:P3HT blend, however, the red emission decreased with increasing concentration of TBST and 98.6% of the emission was from TBST when the concentration of NIR material reached 10 wt. %. The F8BT:P3HT blend shows a better energy transfer to TBST than MDMO-PPV but the EQE (0.08 % with a maximum emission at 840 nm) was, still, much lower than what was achieved with F8BT and TFB interlayer (0.21 % with a maximum emission at 835 nm). However, their turn-on voltages were much lower (1.8 V instead of 6.3 V).

Once again the EL peak of TBST was shifted to the red with increasing concentration; approaching the EL spectrum of a pure TBST device. This could be explained by the presence of intermolecular interactions and aggregate formation.

A significant drop in the EQE was observed with increasing TBST concentration (see Figure 8-22).

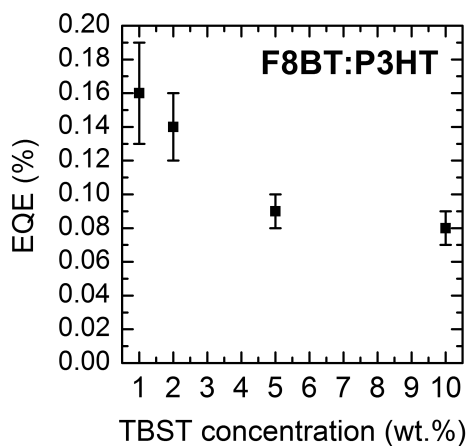


Figure 8-22 EQE plotted as a function of TBST concentration for 1 to 10 wt. % TBST.

8.3 Conclusion

Several configurations with different hosts and blends were tested in order to enhance the efficiency of NIR-OLEDs based on TBST. The charge and/or energy transfer from the red emitters (MDMO-PPV and F8BT:P3HT) appeared not to be as good as the one from the green emitter F8BT despite a better absorption from TBST in the red region. However, they allowed a more red-shifted emission and lower turn-on voltages.

In all experiments the EQEs decreased with increasing concentration of TBST that might be due to a purer emission from TBST and the formation of aggregates.

Best results were achieved using a TFB interlayer and a F8BT:TBST 5 wt. % blend exhibiting an EQE of 0.21 % with 99.5 % of the emission in the near-infrared (835 nm).

9 Near-infrared emission from compounds emitting in the visible

To most chemists π -conjugated systems are flat, however, by introducing appropriate substituents one can twist the aromatic core of the molecule [270, 271]. The influence of twisting the molecule on the properties of the materials is, thus, of interest.

The group of Aurelio Mateo-Alonso (University of Freiburg) chose to investigate the effect of the twisting by overcrowding hexaazatriphenylene compounds (HATs) with triisopropylsilyl (TIPS) [272] and trisobutylsilyl (TIBS) substituents. HATs have been mostly used in metal complex materials as a bis or tris-chelating ligand [273] thanks to, among others, its electron deficient π -systems which exhibit metal-to-ligand charge-transfer [274]. But HATs are attractive materials for organic electronic devices because of the wide range of morphologies (crystalline, columnar discotic liquid-crystalline and amorphous) they can have in films, their electron transporting properties and the fact that their HOMO and LUMO are easy to tune through substitution [275-277].

In this chapter the effect of the twisting on HAT-TIPS and HAT-TIBS on the photophysics of the devices will be studied and devices exhibiting near-infrared OLEDs will be presented.

9.1 The compounds

The compounds were synthesised by Sunil Choudhary (University of Freiburg) and are composed of a hexaazatriphenylene (HAT) core with triisopropylsilyl (TIPS) and trisobutylsilyl (TIBS) substituents

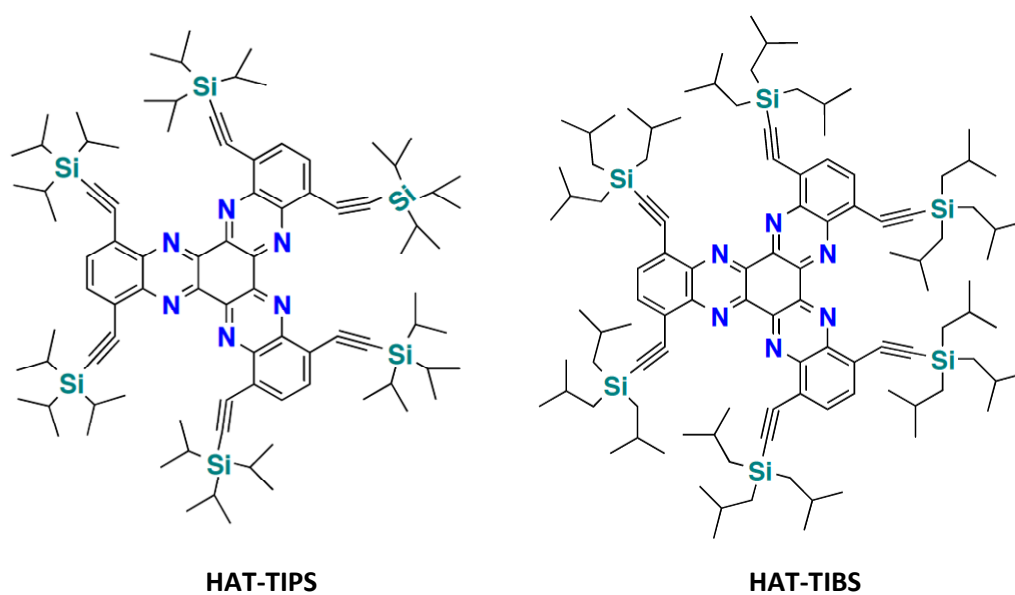


Figure 9-1 Chemical structure of the compounds HAT-TIPS and HAT-TIBS – data from University of Freiburg

As we can see in Figure 9-1 these two compounds differ only by their substituent on the silicon atom (Si). The close proximity of the bulky substitution distorts the planarity of the HAT chromophore. Such distortions provide molecules with a D_{3h} or “propeller” structure (orthorhombic, international symbol mmm).

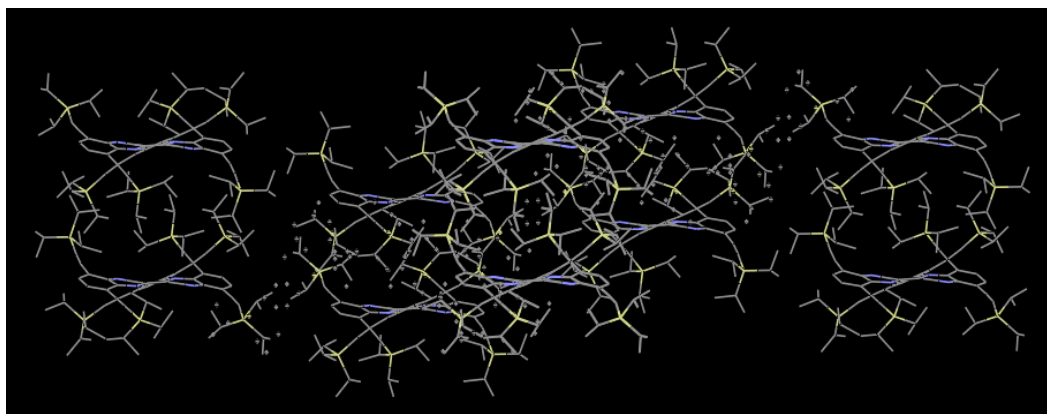


Figure 9-2 Packing of the molecule HAT-TIPS, one can see the twist of the aromatic core as well – data from University of Freiburg.

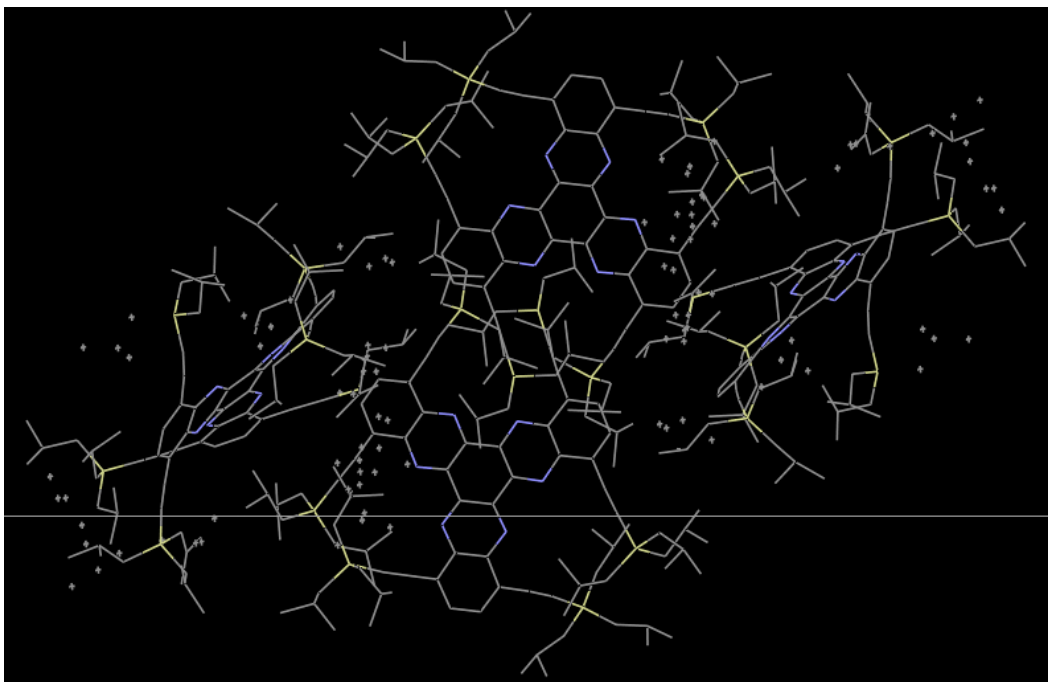


Figure 9-3 Packing of the molecule HAT-TIBS, one can see the twist of the aromatic core as well – data from University of Freiburg

The large difference on the volume of their substituents results in very different packing. Figure 9-2 and Figure 9-3 show that the aromatic cores of the molecules are twisted and HAT-TIBS's aromatic core is more twisted than that of HAT-TIPS. This can be explained by the fact that the substituents of HAT-TIBS are bigger than the ones of HAT-TIPS.

Furthermore, HAT-TIPS is characterized by a columnar packing whereas HAT-TIBS by a herringbone packing, which could lead to different morphologies of the spin-coated films and spectroscopic properties of the compounds. It should be noted that there are no π -interactions between the layers of HAT-TIPS since they are separated by 8 Å and that π -interaction usually happens around 3 Å for this class of compounds [276]. This can be explained by the steric crowding spawn by the substituents [146]. Such big separation between molecules should ensure an effective emission in the solid state making these types of molecules ideal candidates for OLED applications.

9.2 Absorption and photoluminescence

The absorption spectra (see Figure 9-4) of HAT-TIPS and HAT-TIBS films were similar except for the presence of peaks between 550 and 650 nm for HAT-TIBS. These peaks were also present in the absorption spectra measured in solution at the University of Freiburg and their origin has not been yet identified.

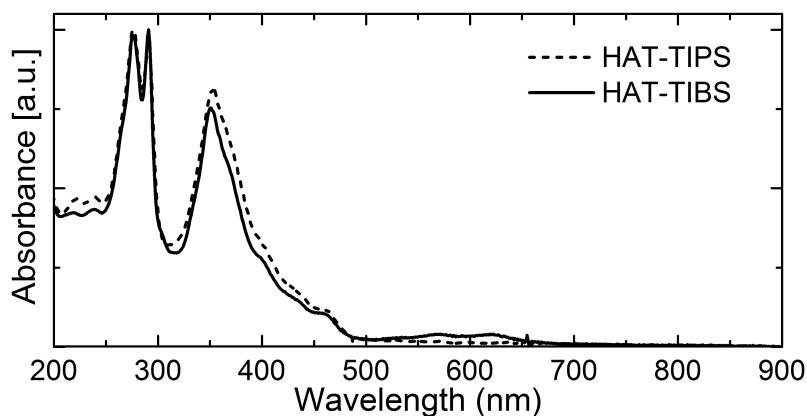


Figure 9-4 Absorption spectra of HAT-TIPS and HAT-TIBS spin-coated from a 2.5 wt. % toluene solution

The photoluminescence spectra of HAT-TIPS and HAT-TIBS films were measured with the help of Giulia Tregnago at UCL, by exciting the samples at 325 nm and are shown in Figure 9-5. HAT-TIPS is characterized by a maximum peak emission at 540 nm whereas HAT-TIBS shows a peak at 515 nm. We know that the packing of HAT-TIPS and HAT-TIBS is very different. HAT-TIPS presents a columnar packing type whereas HAT-TIBS is much less packed. This could explain the red-shift of HAT-TIPS compared to HAT-TIBS.

Furthermore, the emission peak of HAT-TIBS is very close to the one observed in solution at Freiburg University (around 500 nm, figure not shown) confirming the hypothesis of a low packing structure.

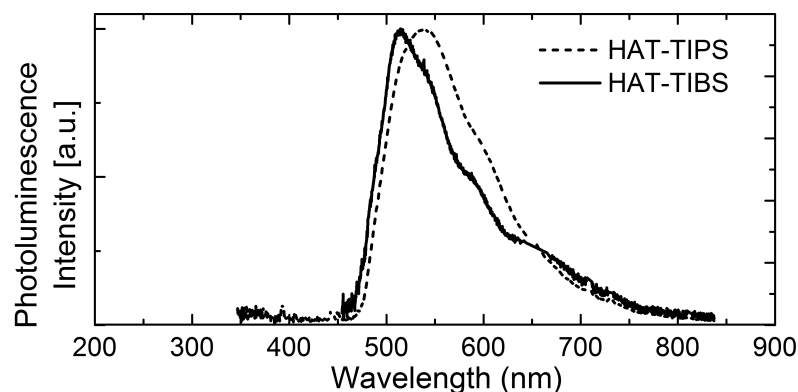


Figure 9-5 Photoluminescence spectra of HAT-TIPS and HAT-TIBS spin-coated from a 2.5 wt. % solution in toluene measured with a 325 nm laser and the ANDOR

9.3 OLEDs

9.3.1 Basic devices

Devices were made with the structure: ITO/PEDOT:PSS/active layer/Ca (30 nm)/Al (150 nm). The ITO was oxygen plasma treated for 10 minutes immediately prior to the spin-coating of the PEDOT:PSS, which was then baked at 180°C for 10 minutes on a hot plate.

The active layer consisted of a film of pure HAT-TIPS or HAT-TIBS. These were spin-coated in nitrogen atmosphere from 2.5 % by weight solutions in toluene. The thicknesses of these films are around 90 nm.

The HOMO-LUMO energy levels of HAT-TIPS and HAT-TIBS were measured at Freiburg University according to [278]. The results are depicted in Figure 9-6. One can see that the injection of holes has to overcome a barrier of 0.9 eV which could lead to unbalanced charge carrier concentration within the devices.

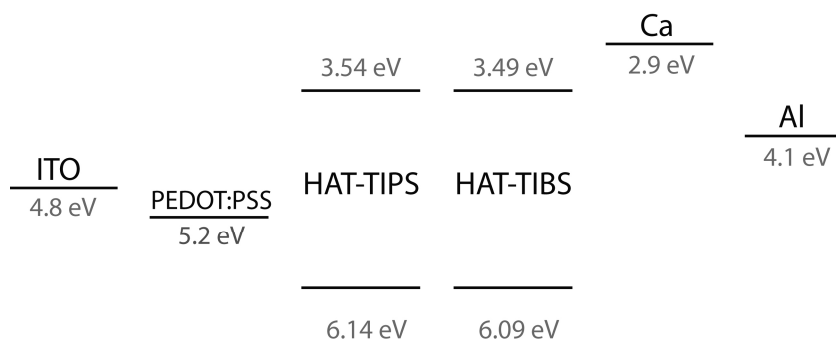


Figure 9-6 Energy diagram of the materials used in the experiments compared with the work functions of the electrodes. The HOMO and LUMO levels of HAT-TIPS and HAT-TIBS were determined at Freiburg University. Other values are from literature [148].

When measuring the current-voltage-light characteristics of these devices, the photodiode did measure an emission of light, however, this emission was so low that the ANDOR spectrometer could not detect it and, thus, the measurement of the electroluminescence spectra of these devices had not been possible. This could be explained by the fact that the injection of holes is too inefficient leading to unbalanced charge carrier concentrations and recombination too close to the anode.

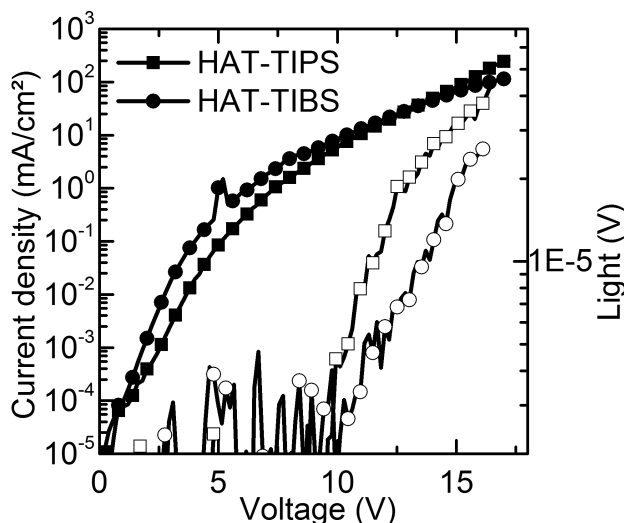


Figure 9-7 Current-voltage-light characteristics of pure HAT-TIPS (squares) and HAT-TIBS (circles) devices. The current densities are represented by filled symbols and light outputs by empty symbols.

As we can see in Figure 9-7, HAT-TIBS devices had higher turn-on voltages and current densities than HAT-TIPS, which could be explained by their different packing.

9.3.2 Insertion of an hole-injecting layer

Since hexaazatriphenylene molecules are electron transporter [137, 275-277, 279, 280], a hole injection layer (TFB) (see part 5.1.2) was inserted between the PEDOT:PSS and the active layers. This extra layer should ease the injection and the transport of the holes and consequently improve the charge carrier balance in the devices.

TFB was spin-coated on top of PEDOT:PSS and baked at 180 °C for 1 hour. The soluble part of TFB was then removed by a spin-rinsing with toluene and a 10 to 20 nm thick layer was obtained (measured by profilometry). The active layer was then spin-coated on top of it under the same processing conditions as the previous devices.

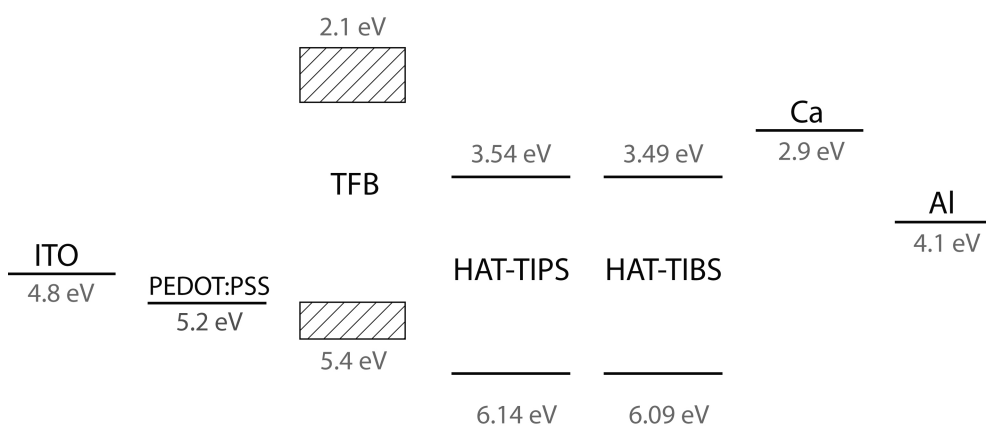


Figure 9-8 Energy diagram of the materials used in these experiments compared with the work functions of the electrodes. The HOMO and LUMO levels of HAT-TIPS and HAT-TIBS were determined at Freiburg University and TFB at UCL, the errors on the values of TFB are represented. Other values are from literature [148].

From the energy diagram of the materials (see Figure 9-8) one can see that the insertion of TFB should ease the injection of the hole by reducing the barrier by 0.2 eV.

In this configuration, EL was observed in the infra-red range with no emission in the visible for HAT-TIBS and a very weak peak at 600 nm for HAT-TIPS as shown in Figure 9-9 a).

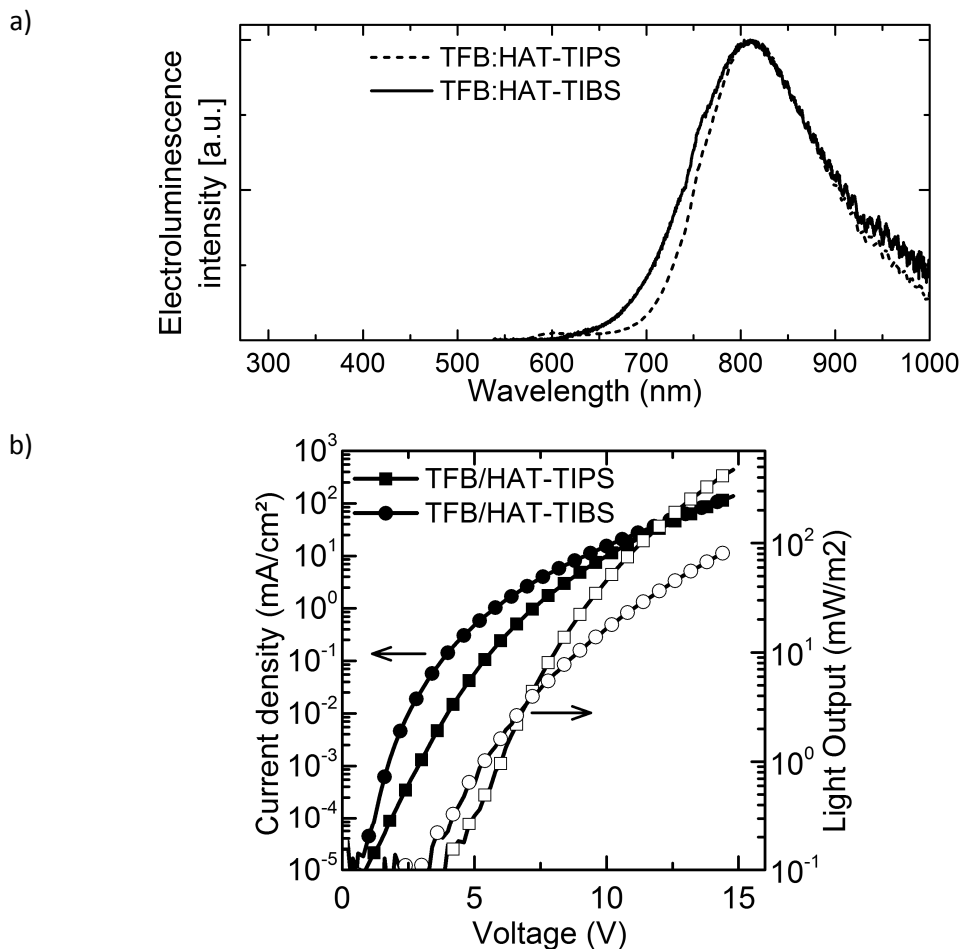


Figure 9-9 a) EL spectra and b) Current-Voltage-Light characteristics of HAT-TIPS (squares) and HAT-TIBS (circles) devices containing TFB as an interlayer. The current densities are represented by filled symbols and light outputs by empty symbols.

The maximum peak of the electroluminescence spectra of both compounds is at 810 nm. The small peak at 600 nm noticed in the emission of the TFB/HAT-TIPS devices could be due to an emission from pure HAT-TIPS or TFB (see part 5.1.2). Emission from pure TFB is, however, unlikely since its main emission peak is located at 465 nm (see part 5.1.2).

The large shift observed between the EL and the PL spectra (see Figure 9-5) could be explained by the formation of an exciplex between TFB and the compounds, and will be discussed in further details in part.9.3.3.

Table 9-1 Properties of the ITO/PEDOT:PSS/TFB/HAT-TIPS or HAT-TIBS/Ca/Al devices in average.

	Max EQE (%)	Light turn-on voltage V_{ON} (V)	Max light output (mW/m ²) @ (114 mA/cm ²)
TFB / HAT-TIPS	0.035 ± 0.005	4.4 ± 0.2	410 ± 30
TFB / HAT-TIBS	0.014 ± 0.005	4.1 ± 0.4	55 ± 20

As we can see from Figure 9-9 b) and Table 9-1, the EQE were low and the turn-on voltage of HAT-TIBS devices was lower than that of the HAT-TIPS devices. At low voltages, current densities in HAT-TIBS devices were higher than that of HAT-TIPS devices, however, the light output increased faster in HAT-TIPS devices.

9.3.3 Investigation of the origin of the near-infrared emission

The near-infrared emission obtained by incorporating a TFB layer in the HAT compounds based OLEDs could be explained by the formation of exciplexes at the interface TFB/ HAT compounds and would account for near infrared light emission from visible emitters. A near-infrared exciplex formed at the interface between rubrene and fullerene was reported from Ng et al. [281] . However, their devices, contrary to the present work, still, had a non-negligible emission of visible light. Clark et al. [137] reported a very similar work in which they observe an exciplex at the interface between a HAT compound and TFB. They proved that the 670 nm emission they obtained was due to the formation of an exciplex with a lifetime of 0.42 ns compared with 270 ps for the HAT compound.

In an attempt to verify the assumption of an exciplex formed at the TFB/HAT interface several experiments were carried out:

First of all, Figure 9-10 shows that the absorption spectra of a 50:50 blend of TFB and the HAT-compounds resulted from the superposition of the absorption of TFB and the HAT compounds indicating the absence of ground-state interactions.

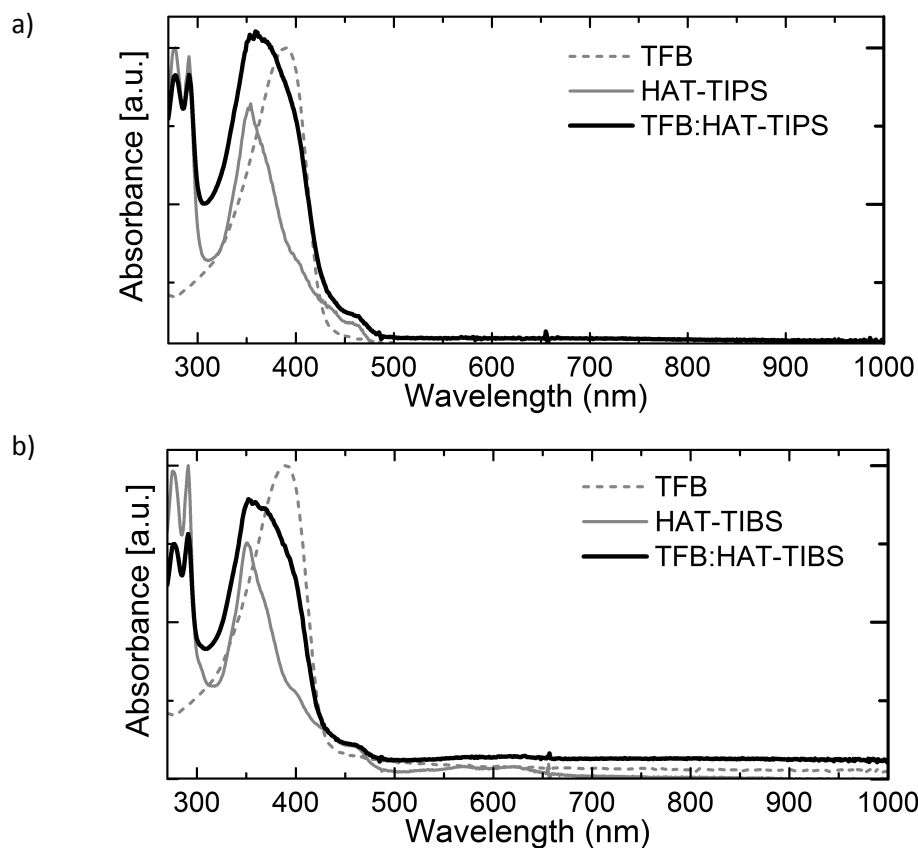


Figure 9-10 Comparison of the absorption spectra of a) TFB, HAT-TIPS and TFB:HAT-TIPS and b) TFB, HAT-TIBS and TFB:HAT-TIBS

Then, the PL of HAT-TIPS and HAT-TIBS blends with TFB were measured, with the help of Giulia Tregnago, and are represented in Figure 9-11. The PL spectra of pure TFB, HAT-TIPS and HAT-TIBS are drawn as well to ease the comparison.

On both graphs we can see that the first emission peak of the blend is the superposition of the emission from TFB and of the pure HAT materials. Furthermore, in both cases we can see the apparition of a second peak near 800 nm that does not correspond to TFB or the pure HAT compounds.

The presence of this new peak at 800 nm and the absence of ground state interaction might indicate the formation of an exciplex between TFB and the HAT-compounds. Furthermore, considering the HOMO/LUMO energy levels of TFB and the HAT-compounds (see Figure 9-8), the recombination of a hole on TFB and an electron on HAT can be reasonably considered.

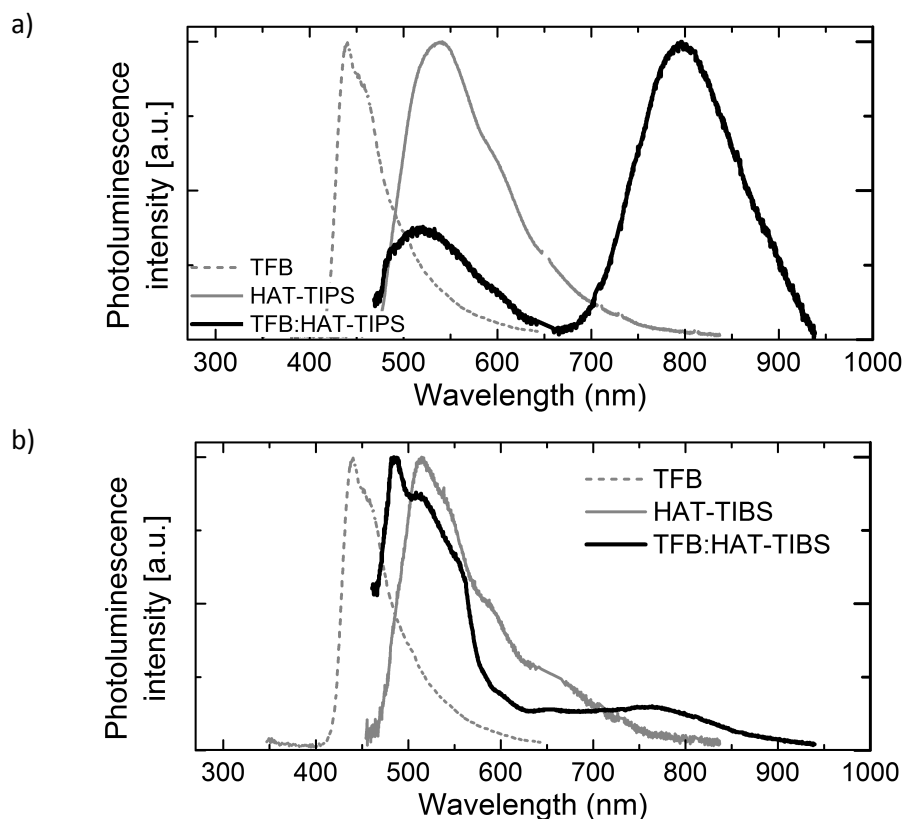


Figure 9-11 Photoluminescence spectra (excitation at 325 nm) of a) HAT-TIPS and b) HAT-TIBS blended with TFB. The PL of the pure materials are also represented for comparison purpose.

The assumption of the formation of an exciplex could also be confirmed by measuring the lifetime of the excited species with the TCSPC (see part 3.3), however, for now, measuring the luminescence decay of the sample has proven difficult and experiments are, still, in progress.

9.4 Conclusion and outlook

In the present work it has been shown that it is possible to obtain light emission from hexaazatriphenylene molecules twisted by triisopropylsilyl and trisobutylsilyl substituents. Due to the different substituents, the molecules have different packing that is reflected in their PL spectra.

Furthermore, it has been proven that NIR emission is achievable by using molecules/polymers that are emitting in the visible via the formation of what is believed to be an exciplex.

Some further work would be beneficial such as measuring the excited state lifetime via time-resolved techniques and an investigation of HAT-TIPS and HAT-TIBS sample via atomic force microscopy to probe morphology discrepancies or fabricating devices with another hole-injection molecule/polymer. Using a blend of TFB and a HAT compound would create a larger interface and might thus improve the efficiency of the devices.

10 General Conclusion

The fabrication and the characterisation of solution-processed OLEDs, all based on new materials, synthesized by research laboratories were reported in the present work.

After introducing the background of OLED devices, materials and techniques necessary to understand the experimental parts of the present work, I focused on the fabrication of phosphorescent OLEDs based on copper complexes that present the advantage of being cheap and non-toxic. Chapter 5 introduced the phosphorescent host and the interlayer that were used together with the transition metal complexes in the following chapter. A rather complete investigation of their photophysical properties together with their behaviour in devices was carried out. The improvement of the injection of charge and of the charge carrier balance in the devices had proven the benefits of the introduction of hole and electron injection/transport layers. Furthermore, these experiments did not show the formation of new electrical species that could influence the phosphorescent devices.

Chapter 6 reported on the properties of the organometallic compounds and their behaviour in devices when TPBi was used as an electron transport material and when TPBi and TFB were used simultaneously as hole transport and electron transport materials. As expected, the compounds that had their triplet energy level below the one of PVK did not achieve as good characteristics as the one with higher triplet energy levels. Devices exhibiting EQEs as high as 1.21 % were demonstrated with compound G and luminances as high as 250 cd.m^{-2} with compound A. However, due to very broad emission spectra the colour of all devices were in the white/yellow/orange range and not in the blue or green region as it could have been expected from the photoluminescence spectra of the compounds. The photophysical measurements performed on A and PVK:A suggested the formation of a triplet exciplex, however, to confirm this result, the experiment should be repeated with a higher energy laser that better excite PVK.

The solvent chosen to dissolve the active layer of the devices is of tremendous importance as demonstrated in Chapter 7. It was shown that even though the

performance of pure PVK devices made from chlorobenzene and tetrahydrofuran were comparable, the morphological differences were crucial when incorporating the copper complex G. The clusters on the THF films were fatal for the OLEDs devices whereas the devices based on chlorobenzene showed a better film morphology and good characteristics. The failure of the devices was attributed to localised electrical short and/or the presence of bigger clusters on THF films that allow the moisture and oxygen to diffuse in the device.

The second part of the present work was dedicated to a relatively new interest in OLED research, namely near-infrared devices.

Chapter 8 focused on a benzoselenadiazole polymer emitting at 880 nm. Different polymers were used as hosts, and the energy transfer from the red emitters (MDMO-PPV and F8BT:P3HT) appeared not to be as good as the one from the green emitter F8BT. However, they allowed a more red-shifted emission and lower turn-on voltages. Best results were achieved using a TFB interlayer and an F8BT:TBST 5 wt. % blend exhibiting an EQE of 0.21 % with 99.5 % of the emission in the near-infrared (835 nm).

Eventually chapter 9 demonstrated the possibility of fabricating near-infrared devices using materials that emit in the visible. This was achieved by using hexaazatriphthylene molecules twisted by triisopropylsilyl and trisobutylsilyl substituents and TFB as a hole injection layer.

10.1 Outlook

In the second part of the present work it was demonstrated that the main difficulty in the making of high efficiency solution-processable OLEDs based on the copper complexes from WWUM is the lack of good soluble phosphorescent hosts available on the market with convenient triplet energy levels and emission. It is thus to the chemistry and the physics labs to collaborate and develop new phosphorescent hosts.

However, researchers are already working on an alternative method that uses a copolymer incorporating an electron-transporting moiety in its backbone. The main advantages would be a better charge carrier balance in the device and the possibility of

avoiding the time-consuming step of the deposition of the electron-transporting layer. But these kinds of polymers are currently difficult to obtain.

Another possibility to achieve high efficiencies is to fabricate the devices completely via thermal evaporation. Unfortunately this is not possible at the moment with the equipment available at UCL.

Finally the work presented in chapter 9 is, still, in its early stage. Some further work would be beneficial for a better understanding of the compounds properties and the behaviour of the devices. Researchers from Freiburg University are working on the synthesis of new twisted compounds in order to further investigate the effect of the twisting on the properties of the materials. Furthermore, further work will be carried on at UCL such as the measurement of the excited state lifetime via time-resolved techniques and the investigation of HAT-TIPS and HAT-TIBS samples via atomic force microscopy to probe morphology discrepancies. Other experiments could also involve the fabrication of OLEDs with a blend of TFB and a HAT compound as the active layer. It would create a larger interface and might thus improve the efficiency; or the fabrication of devices with another hole-injection molecule/polymer.

Bibliography

1. Pope, M., H.P. Kallmann, and P. Magnante, *Electroluminescence in Organic Crystals*. The Journal of Chemical Physics, 1963. **38**: p. 2042-2043.
2. Tang, C.W. and S.A. VanSlyke, *Organic electroluminescent diodes*. Applied Physics Letters, 1987. **51**(12): p. 913-915.
3. Burroughes, J.H., et al., *Light-emitting diodes based on conjugated polymers*. Nature, 1990. **347**: p. 539-541.
4. Mertens, R., *The OLED Handbook. A guide to OLED Technology, Industry & Market 2011*: Metalgrass software.
5. Smith, M.B. and J. March, *Advanced Organic Chemistry: Reactions, Mechanisms and Structure. Sixth Edition* 2007: John Wiley and Sons.
6. Geffroy, B., P.I. Roy, and C. Prat, *Organic light-emitting diode (OLED) technology: materials, devices and display technologies*. Polymer International, 2006. **55**: p. 572-582.
7. Forget, S. and S. Chénais, *Les OLEDs montrent patte blanche*. Photoniques, 2007. **29**: p. 37-43.
8. Hai, N., Z. Bo, and T. Xian-Zhong, *Significant improvement of OLED efficiency and stability by doping both HTL and ETL with different dopant in heterojunction of polymer / small-molecules*. Chinese Physics, 2007. **16**(3): p. 730-734.
9. Nicolai, H.T., et al., *Unification of trap-limited electron transport in semiconducting polymers*. Nature Materials, 2012. **11**: p. 882-887.
10. Wu, C.C., et al., *Surface modification of indium tin oxide by plasma treatment: An effective method to improve the efficiency, brightness, and reliability of organic light emitting devices*. Applied Physics Letters, 1997. **70**(11): p. 1348-1350.
11. Lu, D., et al., *Surface treatment of indium tin oxide by oxygen plasma for organic light-emitting diodes*. Materials Science and Engineering B, 2003. **97**: p. 141-144.
12. Ishibashi, S., et al., *Low resistivity indium-tin oxide transparent conductive films. II. Effect of sputtering voltage on electrical property of films*. Journal of Vacuum Science & Technology A, 1990. **8**(3): p. 1403-1406.
13. Ma, J., et al., *Optical and Electrical Properties of Sn-doped Indium Oxide Films Deposited on Polyester by Reactive Evaporation*. Japanese Journal of Applied Physics, 1998. **37**: p. 5614-5617.

14. Kim, H., et al., *Electrical, optical, and structural properties of indium-tin-oxide thin films for organic light-emitting devices*. Journal of Applied Physics, 1999. **86**(11): p. 6451-6461.
15. Hook, D.A., et al., *Evaluation of Oxygen Plasma and UV Ozone Methods for Cleaning of Occluded Areas in MEMS Devices*. Journal of Microelectromechanical Systems, 2010. **19**(6): p. 1292-1298.
16. Huang, J., et al., *Investigation of the effects of Doping and Post-Deposition Treatments on the Conductivity, Morphology, and Work Function of Poly(3,4-ethylenedioxythiophene)/Poly(styrene sulfonate) Films*. Advanced Functional Materials, 2005. **15**(2): p. 290-296.
17. Brown, T.M., et al., *Built-in field electroabsorption spectroscopy of polymer light-emitting diodes incorporating a doped poly(3,4-ethylene dioxythiophene) hole injection layer*. Applied Physics Letters, 1999. **75**(12): p. 1679-1681.
18. Jin, R., et al., *On the use and influence of electron-blocking interlayers in polymer light-emitting diodes*. Physical Chemistry Chemical Physics, 2009. **11**: p. 3455-3462.
19. Elschner, A. and S. Kirchmeyer, *Organic Photovoltaics: Materials, Device Physics, and Manufacturing Technologies*, ed. C. Brabec, V. Dyakonov, and U. Scherf 2008: Wiley-VCH.
20. Jonda, C., et al., *Surface roughness effects and their influence on the degradation of organic light emitting devices*. Journal of Materials Science, 2000. **35**: p. 5645-5651.
21. Elschner, A., et al., *PEDT/PSS for efficient hole-injection in hybrid organic light-emitting diodes*. Synthetic Metals, 2000. **111-112**: p. 139-143.
22. Jong, M.P.d., L.J.v. Ijzendoorn, and M.J.A.d. Voigt, *Stability of the interface between indium-tin-oxide and poly(3,4-ethylenedioxythiophene)/poly(styrenesulfonate) in polymer light-emitting diodes*. Applied Physics Letters, 2000. **77**(14): p. 2255-2257.
23. Kim, J.-S., et al., *Spin-cast thin semiconducting polymer interlayer for improving device efficiency of polymer light-emitting diodes*. Applied Physics Letters, 2005. **87**(023506).
24. Berntsen, A., et al., *Stability of polymer LEDs*. Optical Materials, 1998. **9**: p. 125-133.
25. Liu, J., et al., *Device performance and polymer morphology in polymer light emitting diodes: The control of device electrical properties and metal/polymer contact*. Journal of Applied Physics, 2000. **88**(2): p. 605-609.
26. Salaneck, W.R., et al., *Electronic and Chemical Structure of Conjugated Polymer Surfaces and Interfaces: Implications for Polymer-Based Electronic Devices*. Synthetic Metals, 1997. **85**: p. 1219-1220.

27. Fowler, R.H. and L. Nordheim, *Electron Emission in Intense Electric Fields*. Proceedings of the Royal Society A, 1928. **119**: p. 173-181.
28. Parker, I.D., *Carrier tunneling and device characteristics in polymer light-emitting diodes*. Journal of Applied Physics, 1994. **75**(3): p. 1656-1666.
29. Braun, D., *Electronic Injection and Conduction Processes for Polymer Devices*. Journal of Polymer Science: Part B: Polymer Physics, 2003. **41**: p. 2622-2629.
30. Scott, J.C. and G.G. Malliaras, *Charge injection and recombination at the metal-organic interface*. Chemical Physics Letters, 1999. **299**: p. 115-119.
31. Conwell, E.M. and M.W. Wu, *Contact injection into polymer light-emitting diodes*. Applied Physics Letters, 1997. **70**: p. 1867.
32. Harada, K., et al., *Organic Homojunction Diodes with a High Built-in Potential: Interpretation of the Current-Voltage Characteristics by a Generalized Einstein Relation*. Physical Review Letters, 2005. **94**: p. 036601.
33. Barth, S., et al., *Current Injection from a metal to a disordered hopping system III. Comparison between experiment and Monte Carlo simulation*. Physical Review B, 1999. **60**(12): p. 8791-8797.
34. Wolf, U., V.I. Arkhipov, and H. Bässler, *Current injection from a metal to a disordered hopping system. I. Monte Carlo simulation*. Physical Review B, 1999. **59**(11): p. 7507-7513.
35. Koller, G., et al., *Band alignment at the organic-inorganic interface*. Applied Physics Letters, 2000. **76**(7): p. 927-929.
36. Hill, I.G., et al., *Molecular level alignment at organic semiconductor-metal interfaces*. Applied Physics Letters, 1998. **73**(5): p. 662-664.
37. Flores, F., J. Ortega, and H. Vázquez, *Modelling energy level alignment at organic interfaces and density functional theory*. Physical Chemistry Chemical Physics, 2009. **11**: p. 8658-8675.
38. Amy, F., C. Chan, and A. Kahn, *Polarization at the gold/pentacene interface*. Organic Electronics, 2005. **6**: p. 85-91.
39. Pai, D.M., J.F. Yanus, and M. Stolka, *Trap-Controlled Hopping Transport*. Journal of Physical Chemistry, 1984. **88**: p. 4714-4717.
40. Alonso, J.L., et al., *Solvent dependent behaviour of poly(9-vinylcarbazole)-based polymer light emitting diodes*. Solid-State Electronics, 2010. **54**: p. 1269-1272.
41. Dexter, D.L., *A Theory of Sensitized Luminescence in Solids*. The Journal of Chemical Physics, 1953. **21**(5): p. 836-850.
42. Nguyen, T.-Q., et al., *Controlling Interchain Interactions in Conjugated Polymers: The effects of Chain Morphology on Exciton-Exciton Annihilation and*

- Aggregation in MEH-PPV Films*. Journal of Physical Chemistry B, 2000. **104**: p. 237-255.
43. Huang, Y.-S., et al., *Electronic structures of interfacial states formed at polymeric semiconductor heterojunctions*. Nature Materials, 2008. **7**: p. 483-489.
 44. Guillet, J., *Polymer photophysics and photochemistry. An introduction to the study of photoprocesses in macromolecules*. 1985: Cambridge University Press, New York, NY.
 45. Förster, T., *Transfer mechanisms of electronic excitation*. Discussions of the Faraday Society, 1959. **27**: p. 7-17.
 46. Turro, N.J., V. Ramamurthy, and J.C. Scaiano, *Principle of Molecular Photochemistry* 2009: University Science Books.
 47. Blatchford, J.W., et al., *Photoluminescence in pyridine-based polymers: Role of aggregates*. Physical Review B, 1996. **54**(13): p. 9180-9189.
 48. Müllen, K. and U. Scherf, *Organic Light Emitting Devices. Synthesis, Properties and Applications* 2006: WILEY-VCH Verlag GmbH&Co.
 49. Frankevich, E.L. and A.A. Lymarev, *Polaron-pair generation in poly(phenylene vinylenes)*. Physical Review B, 1992. **46**: p. 9320-9324.
 50. Mizes, H.A. and E.M. Conwell, *Photoinduced charge transfer in poly(p-phenylene vinylene)*. Physical Review B, 1994. **50**: p. 11243-11246.
 51. Yan, M., et al., *Defect Quenching of Conjugated Polymer Luminescence*. Physical Review Letters, 1994. **73**(5): p. 744-747.
 52. Yan, M., et al., *Interchain Excitations in Conjugated Polymers*. Physical Review Letters, 1995. **75**(10): p. 1992-1995.
 53. Wohlgenannt, M., E. Ehrenfreund, and Z.V. Vardeny, *Photophysics of Molecular Materials : From Single Molecules to Single Crystals*, ed. G. Lanzani 2006: John Wiley & Sons.
 54. Dyakonov, V. and E. Frankevich, *On the role played by polaron pairs in photophysical processes in semiconducting polymers*. Chemical Physics, 1998. **227**: p. 203-217.
 55. Gelinck, G.H., J.M. Warman, and E.G.J. Staring, *Polaron Pair Formation, Migration, and Decay on Photoexcited Poly(phenylenevinylene)*. Journal of Physical Chemistry, 1996. **100**: p. 5485-5491.
 56. Rothberg, L., *Semiconducting Polymers Chemistry, Physics and Engineering*. 2nd ed, ed. G. Hadziioannou and G.C. Malliaras. Vol. 1. 2007, Weinheim, Germany: WILEY-VCH Verlag GmbH & Co. KGaA.

57. Pope, M. and C.E. Swenberg, *Electronic Processes in Organic Crystals*. 1st edition ed. Monographs on the Physics and Chemistry of Materials, 39 1982: Oxford Univ Pr.
58. Conwell, E.M., *Excimers in poly(phenylene vinylene) and its derivatives*. Synthetic Metals, 1997. **85**: p. 995-999.
59. Conwell, E.M., *Mean free time for excimer light emission in conjugated polymers*. Physical Review B, 1998. **57**(22): p. 14200-14202.
60. Jakubiak, R., et al., *Aggregation Quenching of Luminescence in Electroluminescent Conjugated Polymers*. Journal of Physical Chemistry A, 1999. **103**: p. 2394-2398.
61. Sinha, S. and A.P. Monkman, *Effect of electric field, solvent, and concentration on the electroluminescence spectra and performance of poly[2-methoxy-5-(2'-ethyl-hexyloxy)-1,4-phenylenevinylene] based light emitting diodes*. Journal of Applied Physics, 2003. **93**(9): p. 5691-5700.
62. Wu, M.W. and E.M. Conwell, *Effect of interchain coupling on conducting polymer luminescence: Excimers in derivatives of poly(phenylene vinylene)*. Physical Review B, 1997. **56**(16): p. R10060-R10062.
63. Smith, T. and J. Guild, *The C.I.E. colorimetric standard and their use*. Transactions of the Optical Society, 1931-32. **33**(3): p. 73-134.
64. Wikipedia. *International Commission on Illumination*. last update: 15 September 2012 consulted on 12 October 2012]; http://en.wikipedia.org/wiki/International_Commission_on_Illumination].
65. Kazakevich, Y. *Molecular Spectroscopy*. 1998 [cited 2009 August]; Seton Hall University]. Available from: http://hplc.chem.shu.edu/NEW/Undergrad/Molec_Spectr/molec.spectr.general.html
66. Martin, G. and B. Pretzel, *UV-VIS-NIR spectroscopy: what is it & what does it do?* Conservation Journal, 1991(01).
67. Lakowicz, J.R., *Principles of Fluorescence Spectroscopy, Third Edition* 2006: Springer Science.
68. Binnig, G., C.F. Quate, and C. Gerber, *Atomic Force Microscope*. Physical Review Letters, 1986. **56**(9): p. 930-933.
69. Wilson, R.A. and H.A. Bullen. *Introduction to Scanning Probe Microscopy (SPM) - Basic Theory - Atomic Force Microscopy (AFM)*. Available from: http://asdlib.org/onlineArticles/ecourseware/Bullen/SPMModule_BasicTheoryAFM.pdf.

70. Bowen, W.R. and N. Hilal, *Atomic Force Microscopy in Process Engineering: An Introduction to AFM for Improved Processes and Products*, ed. W.R. Bowen and N. Hilal 2009: Butterworth-Heinemann. 283.
71. Glowacki, I. and Z. Szamel, *The nature of trapping sites and recombination centres in PVK and PVK-PBD electroluminescent matrices seen by spectrally resolved thermoluminescence*. Journal of Physics D: Applied Physics, 2010. **43**: p. 295101.
72. Kaifer, A.E. and M. Gómez-Kaifer, *Supramolecular Electrochemistry* 1999: Weinheim: Wiley-VCH.
73. Tsierkezos, N.G., *Cyclic Voltammetric Studies of Ferrocene in Nonaqueous Solvents in the Temperature Range from 248.15 to 298.15K*. Journal of Solution Chemistry, 2007. **36**: p. 289-302.
74. Petrovic, S., *Cyclic Voltammetry of hexachloroiridate (IV): An alternative to the Electrochemical Study of the Ferricyanide Ion*. The Chemical Educator, 2000. **5**(2): p. 231-235.
75. Kounaves, S.P., *Voltammetric techniques*. In: *Handbook of Instrumental Techniques for Analytical Chemistry*, ed. F. Settle 1997.
76. Gagné, R.R., C.A. Kowal, and G.C. Lisensky, *Ferrocene as an Internal Standard for Electrochemical Measurements*. Inorganic Chemistry, 1979. **19**: p. 2854-2855.
77. Gritzner, G. and J. Kůta, *Recommendations on reporting electrode potentials in nonaqueous solvents*. Pure & Applied Chemistry, 1984. **56**(4): p. 461-466.
78. Neuse, E.W., *Synthetic Polymers as Drug-Delivery Vehicles in Medicine*. Metal-Based Drugs, 2008. **2008**: p. 1-19.
79. D'Andrade, B.W., et al., *Relationship between the ionization and oxidation potentials of molecular organic semiconductors*. Organic Electronics, 2005. **6**: p. 11-20.
80. Djurovich, P.I., et al., *Measurements of the lowest unoccupied molecular orbital energies of molecular organic semiconductors*. Organic Electronics, 2009. **10**: p. 515-520.
81. Hill, I.G., et al., *Charge-separation energy in films of π -conjugated organic molecules*. Chemical Physics Letters, 2000. **327**: p. 181-188.
82. Tadayyon, S.M., et al., *Reliable and reproducible determination of work function and ionization potentials of layers and surfaces relevant to organic light emitting diodes*. Organic Electronics, 2004. **5**: p. 199-205.
83. Balzani, V., et al., *Photochemistry and Photophysics of Coordination Compounds: Overview and General Concepts*. Topics in Current Chemistry, 2007. **280**: p. 1-36.

84. Cacialli, F., *Lecture on Plastic and Molecular Electronics*, University College London.
85. Baldo, M.A., et al., *Excitonic singlet-triplet ratio in a semiconducting organic thin film*. *Physical Review B*, 1999. **60**(20): p. 14422-14428.
86. Cao, Y., et al., *Improved quantum efficiency for electroluminescence in semiconducting polymers*. *Nature*, 1999. **397**: p. 414-417.
87. Ho, P.K.H., et al., *Molecular-scale interface engineering for polymer light-emitting diodes*. *Nature*, 2000. **404**: p. 481-484.
88. Segal, M., et al., *Excitonic singlet-triplet ratios in molecular and polymeric organic materials*. *Physical Review B*, 2003. **68**: p. 075211.
89. Dijken, A.v., et al., *Carbazole Compounds as Host Materials for Triplet Emitters in Organic Light-Emitting Diodes: Polymer Hosts for High-Efficiency Light-Emitting Diodes*. *Journal of the American Chemical Society*, 2004. **126**: p. 7718-7727.
90. Köhler, A. and H. Bässler, *Triplet states in organic semiconductors*. *Materials Science and Engineering*, 2009. **R 66**: p. 71-109.
91. Brunner, K., et al., *Carbazole Compounds as Host Materials for Triplet Emitters in Organic Light-Emitting Diodes: Tuning the HOMO Level without influencing the Triplet Energy in Small Molecules*. *Journal of the American Chemical Society*, 2004. **126**(19): p. 6035 - 6042.
92. Köhler, A. and D. Beljonne, *The Singlet-Triplet Exchange Energy in Conjugated Polymers*. *Advanced Functional Materials*, 2004. **14**(1): p. 11-18.
93. Baldo, M.A., M.E. Thompson, and S.R. Forrest, *High-efficiency fluorescent organic light-emitting devices using a phosphorescent sensitizer*. *Nature*, 2000. **403**: p. 750-753.
94. Patel, N.K., S. Cinà, and J.H. Burroughes, *High-Efficiency Organic Light-Emitting Diodes*. *IEEE Journal on selected topics in Quantum Electronics*, 2002. **8**(2): p. 346-361.
95. Köhler, A., J.S. Wilson, and R.H. Friend, *Fluorescence and Phosphorescence in Organic Materials*. *Advanced Materials*, 2002. **14**(10): p. 701-707.
96. Adachi, C., et al., *High-efficiency red electrophosphorescence*. *Applied Physics Letters*, 2001. **78**: p. 1622-1624.
97. Chou, P.-T. and Y. Chi, *Phosphorescent Dyes for Organic Light-Emitting Diodes*. *Chemistry at a European Journal*, 2007. **13**: p. 380-395.
98. Vlček, J.A., *Mechanistic roles of metal-to-ligand charge-transfer excited states in organometallic photochemistry*. *Coordination Chemistry Reviews*, 1998. **177**: p. 219-256.

99. Evans, R.C., P. Douglas, and C.J. Winscom, *Coordination complexes exhibiting room-temperature phosphorescence: Evaluation of their suitability as triplet emitters in organic light emitting diodes*. *Coordination Chemistry Reviews*, 2006. **250**: p. 2093-2126.
100. Oxtoby, D.W., H.P. Gillis, and A. Campion, *Principle of Modern Chemistry 2007*: Cengage Learning.
101. Hoffman, R.V., ed. *Organic Chemistry: An Intermediate Text, 2nd Edition*. 2004, John Wiley and Sons. 6.
102. Ma, Y., et al., *High Luminescence Gold(I) and Copper(I) Complexes with a Triplet Excited State for Use in Light-Emitting Diodes*. *Advanced Materials*, 1999. **11**(10): p. 852-857.
103. Zhang, Q., et al., *Highly Efficient Green Phosphorescent Organic Light-Emitting Diodes based on Cu^I complexes*. *Advanced Materials*, 2004. **16**(5): p. 432-436.
104. Zhang, Q., et al., *Highly Efficient Electroluminescence from Green-Light-Emitting Electrochemical Cells based on Cu^I complexes*. *Advanced Functional Materials*, 2006. **16**: p. 1203-1208.
105. Zhang, Q., et al., *Novel Heteroleptic Cu^I Complexes with Tunable Emission Color for Efficient Phosphorescent Light-Emitting Diodes*. *Advanced Functional Materials*, 2007. **17**: p. 2983-2990.
106. Che, G., et al., *Highly efficient and color-tuning electrophosphorescent devices based on Cu^I complex*. *Applied Physics Letters*, 2006. **89**: p. 103511.
107. Zhang, Q., et al., *Triplet Excitation Confinement in Green Organic Light-Emitting Diodes Containing Luminescent Charge-Transfer Cu(I) Complexes*. *Advanced Functional Materials*, 2012. **22**: p. 2327-2336.
108. Brunner, K., et al., *Carbazole Compounds as Hosts Materials for Triplet Emitters in Organic Light-Emitting Diodes: Tuning the HOMO Level without Influencing the Triplet Energy in Small Molecules*. *Journal of the American Chemical Society*, 2004. **126**(19): p. 6035-6042.
109. D'Angelo, P., et al., *Electrical transport properties characterization of PVK (poly N-vinyl carbazole) for electroluminescent devices applications*. *Solid-State Electronics*, 2007. **51**: p. 123-129.
110. Peter, G., et al., *Picosecond study of singlet exciton dynamics in polyvinylcarbazole (PVK) in the temperature range 5-300 K*. *Chemical Physics*, 1985. **94**: p. 445-453.
111. Qian, L., D. Bera, and P.H. Holloway, *Electrophosphorescence from triplet excimers in poly-(N-vinylcarbazole)*. *Applied Physics Letters*, 2007. **90**: p. 103511.
112. Johnson, G.E., *Emission properties of vinylcarbazole polymers*. *The Journal of Chemical Physics*, 1975. **62**: p. 4697.

113. de Sainte Claire, P., *Molecular Simulation of Excimer Fluorescence in Polystyrene and Poly(vinylcarbazole)*. Journal of Physical Chemistry B, 2006. **110**: p. 7334-7343.
114. Qian, L., D. Bera, and P.H. Holloway, *White light emission from single layer poly(n-vinylcarbazole) polymeric light-emitting devices by mixing singlet and triplet excimer emissions*. The Journal of Chemical Physics, 2007. **127**: p. 244707.
115. Jiang, X., et al., *Effect of carbazole-oxadiazole excited-state complexes on the efficiency of dye-doped light-emitting diodes*. Journal of Applied Physics, 2002. **91**(10): p. 6717-6724.
116. Hu, B., Z. Yang, and F.E. Karasz, *Electroluminescence of pure poly(N-vinylcarbazole) and its blends with a multiblock copolymer*. Journal of Applied Physics, 1994. **76**(4): p. 2419-2422.
117. Wu, C.-C., et al., *Efficient Organic Electroluminescent Devices Using Single-Layer Doped Polymer Thin Films with Bipolar Carrier Transport Abilities*. IEEE Transactions on Electron Devices, 1997. **44**(8): p. 1269-1281.
118. Rippen, G., G. Kaufmann, and W. Klöpffer, *Luminescence of poly(N-vinylcarbazole) films at 77K. I. Fluorescence, phosphorescence and delayed fluorescence*. Chemical Physics, 1980. **52**: p. 165-177.
119. Burkhart, R.D., *Triplet emission from poly(N-vinylcarbazole) Solid Films at Ambient Temperature Studied in the Microsecond Time Regime Using Pulsed Laser Excitation*. Macromolecules, 1983. **16**: p. 820-824.
120. Jankus, V. and A.P. Monkman, *Is Poly(vinylcarbazole) a Good Host for Blue Phosphorescent Dopants in PLEDs? Dimer Formation and Their Effects on the Triplet Energy Level of Poly(N-vinylcarbazole) and Poly(N-Ethyl-2-Vinylcarbazole)*. Advanced Functional Materials, 2011. **21**: p. 3350-3356.
121. Xu, H., et al., *Difference between photoluminescence and electroluminescence of excimer-based platinum [1,3-difluoro-4,6-di(2-pyridinyl)benzene]chloride*. Journal of Physics D: Applied Physics, 2011. **44**: p. 415102.
122. Cadby, A.J., et al., *Film morphology and photophysics of polyfluorene*. Physical Review B, 2000. **62**(3): p. 15604-15609.
123. D'Andrade, B. and S.R. Forrest, *Formation of triplet excimers and dimers in amorphous organic thin films and light emitting devices*. Chemical Physics, 2003. **286**: p. 321-335.
124. Hayer, A., et al., *Morphology dependence of the triplet excited state formation and absorption in polyfluorene*. Physical Review B, 2005. **71**: p. 241302(R).
125. Byun, H.Y., et al., *Suppression of Secondary PL Emission by Indirect Photoexcitation*. Macromolecule Symposia, 2003. **192**: p. 151-160.

126. Yang, C.-C., et al., *Excited State Luminescence of Multi-(5-phenyl-1,3,4-oxadiazol-2-yl)benzenes in an Electron-Donating Matrix: Exciplex or Electroplex?* Journal of Physical Chemistry B, 2010. **114**: p. 756-768.
127. Negres, R.A., et al., *Origin of efficient light emission from a phosphorescent polymer/organometallic guest-host system.* Physical Review B, 2003. **68**: p. 115209.
128. Gong, X., et al., *Phosphorescence from iridium complexes doped into polymer blends.* Journal of Applied Physics, 2004. **95**(3): p. 948-953.
129. Wang, Y.-M., et al., *White emission via electroplex formation at poly(N-vinylcarbazole)/2,9-dimethyl-4,7-diphenyl-1,10-phenanthroline interface.* Applied Surface Science, 2004. **236**: p. 251-255.
130. Li, J., et al., *Electroplex emission of the blend film of PVK and DPVBi.* Solid-State Electronics, 2010. **54**: p. 349-352.
131. Chen, F.-C., et al., *Energy Transfer and Triplet Exciton Confinement in Polymeric Electrophosphorescent Devices.* Journal of Polymer Science: Part B: Polymer Physics, 2003. **41**: p. 2681-2690.
132. Ye, T., J. Chen, and D. Ma, *Electroluminescence of poly(N-vinylcarbazole) films: fluorescence, phosphorescence and electromers.* Physical Chemistry Chemical Physics, 2010. **12**: p. 15410-15413.
133. Kuo, T.-H., et al., *Efficient organic optoelectronics with multilayer structures.* Journal of Materials Chemistry, 2012. **22**: p. 1364-1369.
134. Redecker, M., et al., *High Mobility Hole Transport Fluorene-Triarylamine Copolymers.* Advanced Materials, 1999. **11**(3): p. 241-246.
135. Fong, H.H., A. Papadimitratos, and G.G. Malliaras, *Nondispersive hole transport in a polyfluorene copolymer with a mobility of $0.01 \text{ cm}^2\text{V}^{-1}\text{s}^{-1}$.* Applied Physics Letters, 2006. **89**: p. 172116.
136. Tseng, S.-R., et al., *Deep blue light-emitting diode based on high molecular weight poly(9,9-dioctylfluorene) with high efficiency and color stability.* Organic Electronics, 2008. **9**: p. 279-284.
137. Clark, J., et al., *Charge recombination in distributed heterostructures of semiconductor discotic and polymeric materials.* Journal of Applied Physics, 2008. **103**: p. 124510.
138. Tsami, A., et al., *Random Fluorene Copolymers with On-Chain Quinoxaline Units.* Journal of Polymer Science: Part A: Polymer Chemistry, 2007. **45**: p. 4773-4785.
139. Moons, E., *Conjugated polymer blends: linking film morphology to performance of light emitting diodes and photodiodes.* Journal of Physics: Condensed Matter, 2002. **14**(47): p. 12235-12260.

140. Tang, K.-C., et al., *Broad band and white phosphorescent polymer light-emitting diodes in multilayer structure*. Synthetic Metals, 2008. **158**: p. 287-291.
141. Chen, C.-Y., et al., *Continuous blade coating for multi-layer large-area organic light-emitting diode and solar cell*. Journal of Applied Physics, 2011. **110**: p. 094501.
142. Park, J.J., et al., *Small molecule interlayer for solution processed phosphorescent organic light emitting device*. Organic Electronics, 2009. **10**: p. 189-193.
143. Liu, S., et al., *Low-voltage, high-efficiency nondoped phosphorescent organic light-emitting devices with double-quantum-well structure*. Applied Physics Letters, 2011. **98**: p. 163301.
144. Liu, Z.-Y., et al., *Solution-processed small molecular electron transport layer for multilayer polymer light-emitting diodes*. Synthetic Metals, 2011. **161**: p. 426-430.
145. Huang, S.-Y., et al., *Uniform dispersion of triplet emitters in multi-layer solution-processed organic light-emitting diodes*. Synthetic Metals, 2010. **160**: p. 2393-2396.
146. Zhang, J., et al., *Structure, photophysics, and photooxidation of crowded diethynyltetracenes*. Journal of Materials Chemistry, 2012. **22**: p. 6182.
147. Shakutsui, M., H. Matsuura, and K. Fujita, *Improved efficiency of polymer light-emitting diodes by inserting a hole transport layer formed without thermal treatment above glass transition temperature*. Organic Electronics, 2009. **10**: p. 834-842.
148. Brown, T.M. and F. Cacialli, *Contact Optimization in Polymer Light-Emitting Diodes*. Journal of Polymer Science: Part B: Polymer Physics, 2003. **41**(21): p. 2649-2664.
149. Barbieri, A., G. Accorsi, and N. Armaroli, *Luminescent complexes beyond platinum group: the d^{10} avenue*. Chemical Communications, 2008: p. 2185-2193.
150. Miller, M.T., P.K. Gantzel, and T.B. Karpishin, *Structures of the Copper (I) and Copper (II) Complexes of 2,9-Diphenyl-1,10-phenanthroline: Implications for Excited-State Structural Distorsion*. Inorganic Chemistry, 1998. **37**: p. 2285-2290.
151. Bizzarri, C., *Luminescent Cu(I) and Ir(III) Complexes and their application in optoelectronic devices*, in *Inorganic Chemistry 2011*, Westfälische Wilhelms-Universität Münster: Münster. p. 207.
152. McMillin, D.R., J.R. Kirchhoff, and K.V. Goodwin, *Exciplex quenching of photo-excited copper complexes*. Coordination Chemistry Reviews, 1985. **65**: p. 83-92.
153. Kutal, C., *Spectroscopic and photochemical properties of d^{10} metal complexes*. Coordination Chemistry Reviews, 1990. **99**: p. 213-252.

154. Lavie-Cambot, A., et al., *Improving the photophysical properties of copper(I) bis(phenanthroline) complexes*. Coordination Chemistry Reviews, 2008. **252**: p. 2572-2584.
155. Scaltrito, D.V., et al., *MLCT excited states of cuprous bis-phenanthroline coordination compounds*. Coordination Chemistry Reviews, 2000. **208**: p. 243-266.
156. Hertel, D., et al., *Triplet-Triplet annihilation in a poly(fluorene)-derivative*. Journal of Chemical Physics, 2001. **115**: p. 10007-10013.
157. Armaroli, N., *Photoactive mono- and polynuclear Cu(I)-phenanthrolines. A viable alternative to Ru(II)-polypyridines?* Chemical Society Reviews, 2001. **30**: p. 113.
158. Kuang, S.-M., et al., *Synthesis and Structural Characterization of Cu(I) and Ni(II) Complexes that Contain the Bis[2-(diphenylphosphino)phenyl]ether Ligand. Novel Emission Properties for the Cu(I) Species*. Inorganic Chemistry, 2002. **41**: p. 3313-3322.
159. Jia, W.L., et al., *New Phosphorescent Polynuclear Cu(I) Compounds Based on Linear and Star-Shaped 2-(2'-Pyridyl)benzimidazolyl Derivatives: Syntheses, Structures, Luminescence, and Electroluminescence*. Inorganic Chemistry, 2005. **44**: p. 5706-5712.
160. Armaroli, N., et al., *Highly Luminescent Cu^I Complexes for Light-Emitting Electrochemical Cells*. Advanced Materials, 2006. **18**: p. 1313-1316.
161. Demas, J.N. and G.A. Crosby, *The Measurement of Photoluminescence Quantum Yields. A Review*. The Journal of Physical Chemistry, 1971. **75**(5): p. 991-1024.
162. Kirchoff, J.R., et al., *Temperature Dependence of Luminescence from Cu(NN)₂⁺ Systems in Fluid Solution. Evidence for the Participation of Two Excited States*. Inorganic Chemistry, 1983. **22**: p. 2380-2384.
163. Palmer, C.E.A. and D.R. McMillin, *Singlets, Triplets, and Exciplexes: Complex, Temperature-Dependent Emissions from Cu(dmp)(PPh₃)₂⁺ and Cu(phen)(PPh₃)₂⁺ in Solution*. Inorganic Chemistry, 1987. **26**: p. 3837-3840.
164. McMillin, D.R. and K.M. McNett, *Photoprocesses of Copper Complexes that Bind to DNA*. Chemical Reviews, 1998. **98**: p. 1201-1219.
165. Miller, M.T., P.K. Gantzel, and T.B. Karpishin, *Effects of Sterics and Electronic Delocalization on the Photophysical, Structural, and Electrochemical Properties of 2,9-Disubstituted 1,10-Phenanthroline Copper (I) Complexes*. Inorganic Chemistry, 1999. **38**: p. 3414-3422.
166. Asano, M.S., et al., *Temperature-dependent Emission of Copper(I) Phenanthroline Complexes with Bulky Substituents: Estimation of an Energy Gap between the Singlet and Triplet MLCT states*. Chemistry Letters, 2010. **39**: p. 376-378.

167. Sommer, J.R., et al., *Efficient Near-Infrared Polymer and Organic Light-Emitting Diodes Based on Electrophosphorescence from (Tetraphenyltetranaphtho[2,3]porphyrin)-platinum(II)*. Applied Materials & Interfaces, 2009. **1**(2): p. 274-278.
168. Choulis, S.A., et al., *Interface Modification to Improve Hole-Injection Properties in Organic Electronic Devices*. Advanced Functional Materials, 2006. **16**: p. 1075-1080.
169. Vaeth, K.M. and C.W. Tang, *Light-emitting diodes based on phosphorescent guest/polymeric host systems*. Journal of Applied Physics, 2002. **92**(7): p. 3447-3453.
170. Kalinowski, J., *Excimers and exciplexes in organic electroluminescence*. Materials Science-Poland, 2009. **27**(3): p. 735-756.
171. Masuhara, H., N. Tamai, and N. Mataga, *Energy transfer in the doped poly(N-vinylcarbazole) films*. Chemical Physics Letters, 1982. **91**(3): p. 209-212.
172. Nguyen, T.-Q., V. Doan, and B.J. Schwartz, *Conjugated polymer aggregates in solution: Control of interchain interactions*. Journal of Chemical Physics, 1999. **110**(8): p. 4068-4078.
173. Nguyen, T.-Q., et al., *Improving the performance of conjugated polymer-based devices by control of interchain interactions and polymer film morphology*. Applied Physics Letters, 2000. **76**(17): p. 2454-2456.
174. Raynes, P. and T. Uchida, *Handbook of Optoelectronics*, ed. J.P. Dakin and R.G.W. Brown 2006: Taylor & Francis Group.
175. Scott, J.C., et al., *Degradation and failure of MEH-PPV light-emitting diodes*. Journal of Applied Physics, 1996. **79**(5): p. 2745-2751.
176. Chao, C.-I., K.-R. Chuang, and S.-A. Chen, *Failure phenomena and mechanisms of polymeric light-emitting diodes: Indium-tin-oxide damage*. Applied Physics Letters, 1996. **69**(19): p. 2894-2896.
177. Kasim, R.K., et al., *Investigation of device failure mechanisms in polymer light-emitting diodes*. Synthetic Metals, 1997. **85**: p. 1213-1214.
178. Kim, J.-S., et al., *Nature of Non-emissive Black Spots in Polymer Light-Emitting Diodes by In-Situ Micro-Raman Spectroscopy*. Advanced Materials, 2002. **14**(3): p. 206-209.
179. Cocchi, M., et al., *Highly efficient near-infrared organic excimer electrophosphorescent diodes*. Applied Physics Letters, 2007. **90**: p. 023506.
180. Cocchi, M., et al., *Excimer-based red/near-infrared organic light-emitting diodes with very high quantum efficiency*. Applied Physics Letters, 2008. **92**: p. 113302.

181. Fenwick, O., et al., *Linear and Cyclic Porphyrin Hexamers as Near-Infrared Emitters in Organic Light-Emitting Diodes*. Nano Letters, 2011. **11**: p. 2451-2456.
182. Gillin, W.P. and R.J. Curry, *Erbium (III) tris (8-hydroxyquinoline) (ErQ): A potential material for silicon compatible 1.5 μm emitters*. Applied Physics Letters, 1999. **74**(6): p. 798-799.
183. Khreis, O.M., et al., *Infrared organic light emitting diodes using neodymium tris-(8-hydroxyquinoline)*. Journal of Applied Physics, 2000. **88**(2): p. 777-780.
184. Kim, D.Y., et al., *Organic Infrared Upconversion Device*. Advanced Materials, 2010. **22**: p. 2260-2263.
185. Macdonald, I.J. and T.J. Dougherty, *Basic principles of photodynamic therapy*. Journal of Porphyrins and Phthalocyanines, 2001. **5**: p. 105-129.
186. Ostrowski, J.C., et al., *Near-Infrared Electroluminescent Light-Emitting Devices Based on Ethyne-Bridged Porphyrin Fluorophores* Advanced Materials, 2003. **15**(15): p. 1296-1300.
187. Rossi, E., et al., *From red to near infra-red OLEDs: the remarkable effect of changing from X = -Cl to -NCS in a cyclometallated [Pt(N^CN)X] complex {N^CN = 5-mesityl-1,3-di(2-pyridyl)benzene}*. Chemical Communications, 2012. **48**: p. 3182-3184.
188. Slooff, L.H., et al., *Rare-earth doped polymers for planar optical amplifiers*. Applied Physics Reviews, 2002. **91**(7): p. 3955-3980.
189. Suzuki, H., *Self-enhancement in the electroluminescence of a near-infrared ionic dye*. Applied Physics Letters, 2000. **76**(12): p. 1543-1545.
190. Whelan, H.T., et al., *Effect of NASA Light-Emitting Diode Irradiation on Wound Healing*. Journal of Clinical Laser Medicine & Surgery, 2001. **19**(6): p. 305-314.
191. Yang, Y., et al., *Efficient near-infrared organic light-emitting devices based on low-gap fluorescent oligomers*. Journal of Applied Physics, 2009. **106**: p. 044509.
192. Caspar, J.V., et al., *Application of the Energy Gap Law to the Decay of Charge-Transfer Excited States*. Journal of the American Chemical Society, 1982. **104**: p. 630-632.
193. Englman, R. and J. Jortner, *The energy gap law for radiationless transitions in large molecules*. Molecular Physics, 1970. **18**: p. 145-764.
194. Kober, E.M., et al., *Application of the Energy Gap Law to Excited-State Decay of Osmium(II)-Polypyridine Complexes: Calculation of Relative Nonradiative Decay Rates from Emission Spectral Profiles*. Journal of Physical Chemistry, 1986. **90**: p. 3722-3734.
195. Bettencourt-Dias, A.d., *Lanthanide-based emitting materials in light-emitting diodes*. Dalton Transactions, 2007: p. 2229-2241.

196. Curry, R.J. and W.P. Gillin, *1.54 μm electroluminescence from erbium (III) tris(8-hydroxyquinoline) (ErQ)-based organic light-emitting diodes*. Applied Physics Letters, 1999. **75**: p. 1380-1382.
197. Harrison, B.S., et al., *Near-infrared electroluminescence from conjugated polymer/lanthanide porphyrin blends*. Applied Physics Letters, 2001. **79**(23): p. 3770-3772.
198. Harrison, B.S., et al., *Near-Infrared Photo- and Electroluminescence of Alkoxy-Substituted Poly(p-phenylene) and nonconjugated Polymer/Lanthanide Tetraphenylporphyrin Blends*. Chemistry of Materials, 2004. **16**: p. 2938-2947.
199. Hong, Z., et al., *Infrared and visible emission from organic electroluminescent devices based on praseodymium complex*. Applied Physics Letters, 2001. **79**: p. 1942-1944.
200. Hong, Z.R., et al., *Infrared electroluminescence of ytterbium complexes in organic light emitting diodes*. Thin Solid Films 2001. **391**: p. 122-125.
201. Kang, T.-S., et al., *Near-Infrared Light-Emitting Diodes (LEDs) Based on Poly(phenylene)/Yb-tris(β -Diketonate) Complexes*. Advanced Functional Materials, 2003. **13**: p. 205-210.
202. Kang, T.-S., et al., *Near-Infrared Electroluminescence from Lanthanide Tetraphenylporphyrin:Polystyrene Blends*. Advanced Materials, 2003. **15**: p. 1093-1097.
203. Katkova, M.A., et al., *Lanthanide imidodiphosphinate complexes - Synthesis, structure and new aspects of electroluminescent properties*. Synthetic Metals, 2009. **159**: p. 1398-1402.
204. Kawamura, Y., et al., *Observation of neodymium electroluminescence*. Applied Physics Letters, 1999. **74**: p. 3245-3247.
205. Kido, J. and Y. Okamoto, *Organo Lanthanide Metal Complexes for Electroluminescent Materials*. Chemical Reviews, 2002. **102**: p. 2357-2368.
206. Li, Z., et al., *1.54 μm Near-infrared photoluminescent and electroluminescent properties of a new Erbium (III) organic complex*. Organic Electronics, 2008. **9**: p. 487-494.
207. Li, Z., et al., *The near-infrared optical properties of an Nd (III) complex and its potential application in electroluminescence*. Inorganic Chemistry Communications, 2009. **12**: p. 151-153.
208. Silva, M.C., et al., *Structural and spectroscopic characterization of poly(styrene sulfonate) films doped with neodymium ions*. Journal of Non-Crystalline Solids, 2008. **354**: p. 5496-5503.

209. Slooff, L.H., et al., *Near-infrared electroluminescence of polymer light-emitting diodes doped with a lissamine-sensitized Nd³⁺ complex*. Applied Physics Letters, 2001. **78**: p. 2122-2124.
210. Sun, R.G., et al., *1.54 μm infrared photoluminescence and electroluminescence from an erbium organic compound*. Journal of Applied Physics, 2000. **87**(10): p. 7589-7591.
211. Zang, F.X., et al., *1.4 μm band electroluminescence from organic light-emitting diodes based on thulium complexes*. Applied Physics Letters, 2004. **84**: p. 2679-2681.
212. Schanze, K.S., et al., *Near-infrared organic light emitting diodes*. Synthetic Metals, 2003. **137**: p. 1013-1014.
213. O'Riordan, A., et al., *Near infrared electroluminescence from neodymium complex-doped polymer light emitting diodes*. Thin Solid Films, 2006. **497**: p. 299-303.
214. Cheng, C.-H., et al., *1.1 μm near-infrared electrophosphorescence from organic light-emitting diodes based on copper phthalocyanine*. Applied Physics Letters, 2006. **88**: p. 213505.
215. Holder, E., B.M.W. Langeveld, and U.S. Schubert, *New Trends in the Use of Transition Metal-Ligand Complexes for Applications in Electroluminescent Devices*. Advanced Materials, 2005. **17**: p. 1109-1121.
216. Holmes, R.J., et al., *Saturated deep blue organic electrophosphorescence using a fluorine-free emitter*. Applied Physics Letters, 2005. **87**: p. 243507.
217. Lamansky, S., et al., *Highly Phosphorescent Bis-Cyclometalated Iridium Complexes: Synthesis, Photophysical Characterization, and Use in Organic Light Emitting Diodes*. Journal of the American Chemical Society, 2001. **123**: p. 4304-4312.
218. Rosenow, T.C., K. Walzer, and K. Leo, *Near-infrared organic light emitting diodes based on heavy metal phthalocyanines*. Journal of Applied Physics, 2008. **103**: p. 043105.
219. Yang, C.-J., et al., *Red to near-infrared electrophosphorescence from a platinum complex coordinated with 8-hydroxyquinoline*. Applied Physics Letters, 2006. **89**: p. 233506.
220. Zhang, D., et al., *Sensitized photo- and electroluminescence from Er complexes mixed with Ir complex*. Applied Physics Letters, 2008. **95**: p. 093501.
221. Baldo, M.A., et al., *Highly efficient phosphorescent emission from organic electroluminescent devices*. Nature, 1998. **395**: p. 151-154.

222. Williams, E.L., J. Li, and G.E. Jabbour, *Organic light-emitting diodes having exclusive near-infrared electrophosphorescence*. Applied Physics Letters, 2006. **89**: p. 083506.
223. Borek, C., et al., *Highly Efficient, Near-Infrared Electrophosphorescence from a Pt-Metalloporphyrin Complex*. Angewandte Chemie International Edition, 2007. **46**: p. 1109-1112.
224. Sun, Y., et al., *Photophysics of Pt-porphyrin electrophosphorescent devices emitting in the near infrared*. Applied Physics Letters, 2007. **90**: p. 213503.
225. Chen, Z.-Q., et al., *Efficient near-infrared organic light-emitting diodes based on multimetallic assemblies of lanthanides and iridium complexes*. Organic Electronics, 2010. **11**: p. 369-376.
226. Xu, H.-B., et al., *Diplatinum alkynyl chromophores as sensitizers for lanthanide luminescence in Pt₂Ln₂ and Pt₂Ln₄ (Ln = Eu, Nd, Yb) arrays with acetylide-functionalized bipyridine/phenanthroline*. Chemical Communications, 2006: p. 1601-1603.
227. Klink, S.I., H. Keizer, and F.C.J.M.v. Veggel, *Transition Metal Complexes as Photosensitizers for Near-Infrared Lanthanide Luminescence*. Angewandte Chemie International Edition, 2000. **39**(23): p. 4319-4321.
228. Bünzli, J.-C.G. and C. Piguet, *Taking advantage of luminescent lanthanide ions*. Chemical Society Reviews, 2005. **34**: p. 1048-1077.
229. Glover, P.B., et al., *Hairpin-Shaped Heterometallic Luminescent Lanthanide Complexes for DNA Intercalative Recognition*. Journal of the American Chemical Society, 2003. **125**: p. 9918-9919.
230. Herrera, J.-M., et al., *Structural and Photophysical Properties of Coordination Networks Combining [Ru(Bpym)(CN)₄]²⁻ or [Ru(CN)₄]₂(μ-bpym)]⁴⁻ Anions (bpym = 2,2'-Bipyrimidine) with Lanthanide(III) Cations: Sensitized Near-Infrared Luminescence from Yb(III), Nd(III), and Er(III) Following Ru-to-Lanthanide Energy Transfer*. Inorganic Chemistry, 2006. **45**(10): p. 3895-3904.
231. Kennedy, F., et al., *Sensitized near-infrared luminescence from lanthanide(III) centres using Re(I) and Pt(II) diimine complexes as energy donors in d-f dinuclear complexes based on 2,3-bis(2-pyridyl)pyrazine*. Dalton Transactions, 2007: p. 1492-1499.
232. Shavaleev, N.M., et al., *Sensitized near-infrared emission from lanthanides using a covalently-attached Pt(II) fragment as an antenna group*. Chemical Communications, 2003: p. 1134-1135.
233. Shavaleev, N.M., et al., *Sensitized Near-Infrared Emission from Complexes of Yb^{III}, Nd^{III}, Er^{III} by Energy-Transfer from Covalently Attached Pt^{II}-Based Antenna Units*. Chemistry a European Journal, 2003. **9**: p. 5283-5291.

234. Bai, Q., et al., *Synthesis, Photophysical Properties and Near Infrared Electroluminescence of 1(4),8(11),15(18),22(25)-Tetra-(methoxyphenoxy)phthalocyanine*. Chinese Journal of Chemistry, 2012. **30**: p. 689-694.
235. Casalboni, M., et al., *Optical investigation of infrared dyes in hybrid thin films*. Applied Physics Letters, 1999. **75**(15): p. 2172-2174.
236. Suzuki, H., *Infrared electroluminescence from an organic ionic dye containing no rare-earth ions*. Applied Physics Letters, 2002. **80**(18): p. 3256-3258.
237. Suzuki, H., et al., *Polymethine Dyes as Novel Efficient Infrared Electroluminescence Materials*. Molecular Crystals and Liquid Crystals, 2006. **444**: p. 51-59.
238. Qian, G., et al., *Synthesis and Application of Thiadiazoloquinoxaline-Containing Chromophores as Dopants for Efficient Near-Infrared Organic Light-Emitting Diodes*. Journal of Physical Chemistry C, 2009. **113**: p. 1589-1595.
239. Bourdakos, K.N., et al., *Highly efficient near-infrared hybrid organic-inorganic nanocrystal electroluminescence device*. Applied Physics Letters, 2008. **92**: p. 153311.
240. Cheng, K.-Y., et al., *Hybrid Silicon Nanocrystal-Organic Light Emitting Devices for Infrared Electroluminescence*. Nano Letters, 2010. **10**: p. 1154-1157.
241. Curry, R.J., et al., *Silicon-based organic light-emitting diode operating at a wavelength of 1.5 μm* . Applied Physics Letters, 2000. **77**(15): p. 2271-2273.
242. Finlayson, C.E., et al., *Infrared emitting PbSe nanocrystals for telecommunications window applications*. Journal of Modern Optics, 2005. **52**(7): p. 955-964.
243. Tessler, N., et al., *Efficient Near-Infrared Polymer Nanocrystal Light-Emitting Diodes*. Science, 2002. **295**: p. 1506-1508.
244. Andersson, M.R., et al., *Electroluminescence from Substituted Poly(thiophenes): From Blue to Near-Infrared*. Macromolecules, 1995. **28**: p. 7525-7529.
245. Baigent, D.R., et al., *Polymer electroluminescence in the near infra-red*. Synthetic Metals, 1995. **71**: p. 2175-2176.
246. Berggren, M., et al., *Thermal control of near-infrared and visible electroluminescence in alkyl-phenyl substituted polythiophenes*. Applied Physics Letters, 1994. **65**(12): p. 1489-1491.
247. Chen, M., et al., *1 micron wavelength photo- and electroluminescence from a conjugated polymer*. Applied Physics Letters, 2004. **84**(18): p. 3570-3572.
248. Li, X., et al., *Synthesis and properties of novel poly(p-phenylenevinylene) copolymers for near-infrared emitting diodes*. European Polymer Journal, 2005. **41**: p. 2923-2933.

249. Moratti, S.C., et al., *High Electron Affinity Polymers for LEDs*. *Synthetic Metals*, 1995. **71**: p. 2117-2120.
250. Yang, R., et al., *Deep-Red Electroluminescent Polymers: Synthesis and Characterization of New Low-Band-Gap Conjugated Copolymers for Light-Emitting Diodes and Photovoltaic Devices*. *Macromolecules*, 2005. **38**: p. 244-253.
251. Li, P., et al., *Dual functions of a novel low-gap polymer for near infra-red photovoltaics and light-emitting diodes*. *Chemical Communications*, 2011. **47**: p. 8820-8822.
252. Qian, G., et al., *Simple and Efficient Near-Infrared Organic Chromophores for Light-Emitting Diodes with Single Electroluminescent Emission above 1000 nm*. *Advanced Materials*, 2009. **21**: p. 111-116.
253. Sharbati, M.T., et al., *Near infrared organic light-emitting diodes based on acceptor-donor-acceptor (ADA) using novel conjugated isatin Schiff bases*. *Journal of Luminescence*, 2011. **131**: p. 553-558.
254. Yang, Y., et al., *Near infrared organic light-emitting devices based on donor-acceptor-donor oligomers*. *Applied Physics Letters*, 2008. **93**: p. 163305.
255. Qian, G., et al., *Band Gap Tunable, Donor-Acceptor-Donor Charge-Transfer Heteroquinoid-Based Chromophores: Near Infrared Photoluminescence and Electroluminescence*. *Chemistry of Materials*, 2008. **20**: p. 6208-6216.
256. Jung, I.H., et al., *Synthesis and Characterization of Cyclopentadithiophene-Based Low Bandgap Copolymers Containing Electron-Deficient Benzoselenadiazole Derivatives for Photovoltaic Devices*. *Journal of Polymer Science: Part A: Polymer Chemistry*, 2010. **48**: p. 1423-1432.
257. Hou, J., et al., *Poly[4,4-bis(2-ethylhexyl)cyclopenta[2,1-b;3,4-b']dithiophene-2,6-diyl-alt-2,1,3-benzoselenadiazole-4,7-diyl]*, a New Low Band Gap Polymer in *Polymer Solar Cells*. *Journal of Physical Chemistry C*, 2009. **113**: p. 1601-1605.
258. Donley, C.L., et al., *Effects of Packing Structure on the Optoelectronic and Charge Transport Properties in Poly(9,9-di-n-octylfluorene-alt-benzothiadiazole)*. *Journal of the American Chemical Society*, 2005. **127**: p. 12890-12899.
259. Xiong, Y., et al., *Improved Performance of Polymer Light-Emitting Diodes with an Electron Transport Emitter by Post-Annealing*. *Chinese Physics Letters*, 2009. **26**(9): p. 097801.
260. Yamasaki, N., et al., *Rapid Energy Transfer and Improved Performance of Organic Light-Emitting Diodes Using Composite Film Based on π -Conjugated Polymers*. *Japanese Journal of Applied Physics*, 2009. **48**: p. 101502.
261. Morgado, J., et al., *De-mixing of Polyfluorene-Based Blends by Contact with Acetone:Electro- and Photo-luminescence Probes*. *Advanced Materials*, 2001. **13**(11): p. 810-814.

262. Morgado, J., et al., *Optical and morphological investigations of non-homogeneity in polyfluorene blends*. Synthetic Metals, 2001. **124**: p. 63-66.
263. Riehn, R., et al., *Phase-Separated Conjugated-Polymer Blend by Means of Near-Field Excitation*. Advanced Functional Materials, 2006. **16**(4): p. 469-476.
264. Arredondo, B., et al., *Comparison between electroluminescent organic diodes based on new poly(2,7-fluorene phenylidene) derivatives and commercial polymers*. Photonic Materials, Devices and Applications. Edited by Badenes, Goncal; Abbott, Derek; Serpenguzel, Ali. Proceedings of the SPIE, 2005. **5840**: p. 853-861.
265. Jarzab, D., et al., *Photoluminescence of conjugated polymer blends at the nanoscale*. Soft Matter, 2010. **7**: p. 1702-1707.
266. Tvingstedt, K., et al., *Electroluminescence from Charge Transfer States in Polymer Solar Cells*. Journal of the American Chemical Society, 2009. **131**: p. 11819-11824.
267. Morteani, A.C., et al., *Exciton Regeneration at Polymeric Semiconductor Heterojunctions*. Physical Review Letters, 2004. **92**(24): p. 247402.
268. Lazzerini, G.M., et al., *Low-temperature treatment of semiconducting interlayers for high-efficiency light-emitting diodes based on a green-emitting polyfluorene derivative*. Applied Physics Letters, 2011. **99**: p. 243305.
269. Kim, Y. and D.D.C. Bradley, *Bright red emission from single layer polymer light-emitting devices based on blends of regioregular P3HT and F8BT*. Current Applied Physics, 2005. **5**: p. 222-226.
270. Pascal, R.A.J., *Twisted Acenes*. Chemical Reviews, 2006. **106**: p. 4809-4819.
271. Lu, J., et al., *Synthesis, Structure, and Resolution of Exceptionally Twisted Pentacenes*. Journal of the American Chemical Society, 2006. **128**(51): p. 17043-17050.
272. Rücker, C., *The Triisopropylsilyl Group in Organic Chemistry: Just a Protective Group or More?* Chemical Reviews, 1995. **95**: p. 1009-1064.
273. Shatruk, M., et al., *Structural and magnetic properties of iron(II) complexes with 1,4,5,8,9,12-hexaazatriphenylene (HAT)*. Dalton Transactions, 2005: p. 1897-1902.
274. Kitagawa, S. and S. Masaoka, *Metal complexes of hexaazatriphenylene (hat) and its derivatives- from oligonuclear complexes to coordination polymers*. Coordination Chemistry Reviews, 2003. **246**: p. 73-88.
275. Lehmann, M., et al., *High Charge-Carrier Mobility in π -Deficient Discotic Mesogens: Design and Structure-Property Relationship*. Chemistry - A European Journal, 2005. **11**: p. 3349-3362.

276. Barlow, S., et al., *Synthesis, Ionisation Potentials and Electron Affinities of Hexaazatrinaphthylene Derivatives*. Chemistry - A European Journal, 2007. **13**: p. 3537-3547.
277. Gao, B., et al., *Starbust substituted hexaazatriphenylene compounds: synthesis, photophysical and electrochemical properties*. Tetrahedron Letters, 2009. **50**: p. 1649-1652.
278. More, S., et al., *Versatile 2,7-Substituted Pyrene synthons for the Synthesis of Pyrene-Fused Azaacenes*. Organic Letters, 2012. **14**(16): p. 4170-4173.
279. Kaafarani, B.R., et al., *High Charge-Carrier Mobility in an Amorphous Hexaazatrinaphthylene Derivatives*. Journal of the American Chemical Society, 2005. **127**: p. 16358-16359.
280. Juárez, R., et al., *Hexaazatriphenylene (HAT) versus tri-HAT: The Bigger the Better?* Chemistry - A European Journal, 2011. **17**: p. 10312-10322.
281. Ng, A.M.C., et al., *Near infrared emission in rubrene:fullerene heterojunction devices*. Chemical Physics Letters, 2009. **474**: p. 141-145.

List of abbreviations, mathematical symbols and compounds

\$	US Dollars
%	Percent
[Ru(bpy) ₃] ²⁺	ruthenium(II) tris(bipyridine)
°	Degree
°C	Celsius degree
μs	Microsecond
2-TNATA	4,4',4''-tris[2-naphthyl(phenyl)amino]triphenylamine
A	Amper
A	Acceptor
Ag	Silver
Å	Angstrom
acn	Acetonitrile
ADA	Acceptor-Donor-Acceptor
ADS	American Dye Source
AFM	Atomic Force Microscopy
Al	Aluminium
Alq ₃	tris(8-hydroxyquinoline) aluminium
AMOLED	Active-Matrix Organic Light-Emitting Diode
ANR	Annealed and Not Rinsed
AR	Annealed and Rinsed
Ar	Argon
BCP	2,9-dimethyl-4,7-diphenyl-1,10-phenanthroline
BHT	butylhydroxytoluene
Ca	Calcium
CB	Chlorobenzene
CBP	4,4'-N,N'-dicarbazole-biphenyl
CCD	Charge-coupled device
cd	Candelas
CHCl ₃	Chloroform

CIE	Commission Internationale de l'Eclairage
cm	Centimeter
CPDT	cyclopentadithiophene
Cu	Copper
D	Donor
Dr.	Doctor
DA	Donor Acceptor
DAD	Donor-Acceptor-Donor
DCM	Dichloromethane
DFT	Density Functional Theory
DMF	Dimethylformamide
DPEPhos	bis[2-(diphenylphosphino)phenyl]ether
DPEPO	bis[2-(diphenylphosphino)phenyl]ether oxide
DPV	Differential Pulse Voltammetry
$E_{1/2}$	Half wave potential
EA or $\mathcal{A}e$	Electronic Affinity
E_{HOMO}	Energy of the HOMO level
E_i	Ionization Energy
EL	Electroluminescent
E_{LUMO}	Energy of the LUMO level
E_{opt}	Optical energy gap
E_{pa}	Potential of the anodic peak
E_{pc}	Potential of the cathodic peak
EQE	External Quantum Efficiency
Er	Erbium
E_t	Transport bandgap
E_T	Triplet Energy
Et al.	et alii (and others)
ETL	Electron-transporting layer
eV	Electron volt
E_{vac}	Vacuum level
F8	Poly(9,9-dioctylfluorenyl-2,7-diyl)
F8BT	poly[(9,9-dioctylfluorenyl-2,7-diyl)-alt-co-(1,4-benzo-{2,1',3}-thiadiazole)]
Fc^+/Fc	ferricenium/ferrocene
FRET	Förster Resonance Energy Transfer

HAT	hexaazatrinaphthylene
HD	High Definition
HOMO	Highest Occupied Molecular Orbital
HTL	Hole transporting layer
I	Current
$I(\lambda)$	Spectral power distribution
IC	Internal conversion
IE	Ionisation energy
I_p	Ionization potential
i_{pa}	Anodic current
i_{pc}	Cathodic current
IPES	Inverse PhotoEmission Spectroscopy
ISC	Intersystem crossing
ITO	Indium tin oxide
IUPAC	International Union of Pure and Applied Chemistry
J	Current density
K	Exchange integral
K	Kelvin
LC	Ligand Centered
LCD	Liquid Crystal Display
LEC	Light-emitting electrochemical cell
LED	Light-Emitting Diode
LiF	Lithium Fluoride
lm	Lumen
LMCT	Ligand-to-Metal Charge-Transfer
Ln	Lanthanide
LUMO	Lowest Unoccupied Molecular Orbital
m	Meter
M	Molar concentration (mol.L^{-1})
M_n	Number average molecular weight
M_w	Weight average molecular weight
mA	Milliamper
MC	Metal-Centered
MDMO-PPV	poly[2-methoxy-5-(3',7'-dimethyloctyloxy)-1,4-phenylenevinylene]
MEH-PPV	Poly[2-methoxy-5-(2'-ethyl-hexyloxy)-1,4-phenylene vinylene]

MLCT	Metal-to-Ligand Charge-Transfer
ms	Millisecond
m_s	Spin projection quantum number
M_s	Quantum number for the z-component of the total spin.
mW	Milliwatt
NANR	Not Annealed and Not Rinned
Nd	Neodymium
NHE	Normal Hydrogen Electrode
NIR	Near-Infrared
nm	Nanometer
NPB	N,N'-di-1-naphthyl-N,N-diphenyl-benzidine
ns	Nanosecond
Φ_L	Luminous flux
OLED	Organic Light-Emitting Diode
P3HT	Poly(3-hexylthiophene-2,5-diyl)
PC ₆₁ BM	[6,6]-Phenyl C61 butyric acid methyl ester
PEDOT	Poly(3,4-ethylenedioxythiophene)
PEDOT:PSS	Poly(3,4-ethylenedioxythiophene):poly(styrenesulfonic acid)
PF ₆ ⁻	Hexafluorophosphate
PFB	Poly[(9,9-dioctylfluorenyl-2,7-diyl)-co-(N,N'-diphenyl)-N,N'-di(p-butyl- oxyphenyl)-1,4-diaminobenzene]]
PhD	Doctor of Philosophy
PL	Photoluminescence
PMMA	Poly(methyl methacrylate)
ps	Picosecond
PSS	Poly(styrenesulfonic acid)
PVK	Poly(9-vinylcarbazole)
PYD2	2,6-dicarbazo-1,5-pyridine
q	Electron charge
S	Siemens
s	Second
S	Total spin
SCE	Saturated Calomel Electrode
S_n	Singlet state, with n the vibronic sub-level
SPM	Scanning Force Microscopy

SWV	Sweep Wave Voltammetry
TAZ	3-(Biphenyl-4-yl)-5-(4-tert-butylphenyl)-4-phenyl-4H-1,2,4-triazole
TCTA	4,4',4''-tris(N-carbazolyl)triphenylamine
TBST	Poly[4,4-bis(2-ethylhexyl)-4H-cyclopenta[1,2-b:5,4-b']dithiophene-2,6-diyl-co-4,7-di(thiophen-2-yl)benzo[c][1,2,5]selenadiazole-4,7-diyl]
TCCz	N-(4-(carbazol-9-yl)phenyl)-3,6-bis(carbazol-9-yl) carbazol
TCSPC	Time correlated single photon counting
TFB	Poly[(9,9-dioctylfluorenyl-2,7-diyl)-co-(4,4'-(N-(p-butylphenyl))diphenylamine)]
THF	Tetrahydrofuran
TIBS	trisobutylsilyl
TIPS	triisopropylsilyl
Tm	Thulium
T _n	Triplet state, with n the vibronic sub-level
TPBi	2,2',2''-(1,3,5-benzotriyl)tris-[1-phenyl-1H-benzimidazole] or 1,3,5-tris(phenyl-2-benzimidazole)-benzene or 1,3,5-tris(N-phenylbenzimidazol-2-yl)benzene
TPD	N,N'-diphenyl-N,N'-bis-(3-methyl-phenyl)-[1,1'-biphenyl]-4,4'-diamine
TTA	Triplet Triplet Annihilation
UCL	University College London
UPS	Ultraviolet Photoemission Spectroscopy
UV	Ultraviolet
V	Volt or operation voltage
Vis.	Visible
W	Watt
wt. %.	Weight percent
WWUM	Westfälische Wilhelms-Universität Münster
X	Quasi-equal to red simulation (XYZ system)
Y	Brightness (XYZ system)
Yb	Ytterbium
Z	Quasi-equal to blue simulation (XYZ system)
β	Production efficiency of emissive excitation
γ	Number of excitons formed by unitary charge
Δ	Interface dipole
ΔE _{ST}	Exchange energy

Δ_t	Energy Gap
η_c	Current efficiency
η_{ext}	External Quantum Efficiency
η_{int}	Internal Quantum Efficiency
η_{lum}	Luminous efficiency
η_{PL}	Photoluminescence quantum efficiency
λ	Wavelength
τ	Lifetime value
Φ_{Be}	Electron barrier
Φ_{Bh}	Hole barrier
Φ_M	Metal work function
χ	Out-coupling efficiency
\bar{x}	Colour matching function of the quasi-equal to red simulation X (XYZ system)
\bar{y}	Colour matching function of the brightness Y (XYZ system)
\bar{z}	Colour matching function of the quasi-equal to blue simulation Z (XYZ system)